Assessment of hysteretic dissipative devices to improve the seismic behaviour of steel-concrete composite structures

Tiago Sequeira Guedes Tristany Farinha

Dissertation for the degree of Master of Science in

Civil Engineering

Supervisors: Prof. Luís Manuel Calado de Oliveira Martins

Prof. Jorge Miguel Silveira Filipe Mascarenhas Proença

Jury

Chairperson: Prof. António Manuel Figueiredo Pinto da Costa

Supervisor: Prof. Luís Manuel Calado de Oliveira Martins

Members of the Committee: Prof. Alper Kanyilmaz

December 2020

Statement

I state that the present document is an original work of my own authorship and that it fulfills all the requirements of the "Code of Conduct and Good Practices of the Universidade of Lisboa"

Declaração

Declaro que o presente documento é um trabalho original da minha autoria e que cumpre todos os requisitos do Código de Conduta e Boas Práticas da Universidade de Lisboa.

Agradecimentos

Os meus sinceros agradecimentos aos meus orientadores: professores Luís Calado e Jorge Miguel Proença, pela sua disponibilidade e apoio no decorrer deste trabalho e por me desafiarem com um projecto de tão alto interesse. Gostaria especialmente de agradecer ao professor Luís Calado pela constante motivação e conselhos.

Uma nota de agradecimento a todos os que acompanharam durante a realização do curso, quer nos estudos quer nas celebrações, em especial à minha namorada.

Finalmente agradeço à minha família pelo ânimo e apoio prestado ao logo destes longos anos de estudo.

Abstract

Composite steel-concrete structures subjected to strong earthquakes should be able to dissipate large amounts of energy. Conventional energy dissipation systems rely on the inelastic deformation of the main structural elements. This leads to long interruption of functionality of the building, assuming that the repair work is feasible and not too expensive. The project DISSIPABLE is currently developing an innovative, low-cost and easily-replaceable dissipative device, to absorb the seismic energy, leaving the main structure undamaged. In this work, a numerical model is developed that accurately simulates the behaviour of such devices.

Based on experimental tests, a numerical methodology is developed and calibrated, by optimizing the simulation approach, the material model, the contact model, the geometry definition and the damage criteria. Using the Abaqus/Implicit software, finite element quasi-static simulations were performed to evaluate the hysteretic response of several devices and compare them with the corresponding experimental results. For validation of the numerical model, INERD devices are used. To enhance the plastic response of the constituent materials, a methodology was also developed to calculate approximate parameters of a cyclic combined hardening type of material.

A damage criteria was implemented in the model, successfully simulating material degradation through the opening of a crack. To circumvent the complexity of this strategy, a simplified criteria was studied that is able to predict the failure cycle through the accumulation of plastic strains, with an error lower than 2 cycles.

Finally, parametric analysis of the model suggests an improved behaviour using high strength steel on the plates, and a higher distance between the internal plates.

Keywords: Finite elements analysis; Hysteretic damper; Damage criteria; Material modelling; Replaceable devices; Pin fuse

Resumo

Estruturas mistas de aço e betão sujeitas a fortes terramotos devem ser capazes de dissipar grandes quantidades de energia. Os sistemas convencionais de dissipação de energia dependem da deformação inelástica dos principais elementos estruturais. Isto leva a uma longa interrupção da funcionalidade do edifício, assumindo que o trabalho de reparação é viável e não muito caro. O projecto DISSIPABLE está actualmente a desenvolver um dispositivo dissipativo inovador, de baixo custo e facilmente substituível, para absorver a energia sísmica, deixando a estrutura principal intacta. Esta tese visa desenvolver um modelo numérico capaz de simular com precisão o comportamento de tais dispositivos.

Com base em ensaios experimentais, é criada e calibrada uma metodologia numérica tendo em conta o tipo de simulação, a modelação do material, a modelação de contacto, a definição da geometria e o critério de dano. Utilizando o software Abaqus/Implicit, foram realizadas simulações de vários dispositivos a fim de as comparar com os respectivos resultados experimentais. Como validação do modelo numérico, são utilizados dispositivos INERD e para melhorar a resposta plástica dos materiais constituintes, foi também desenvolvida uma metodologia para calcular parâmetros aproximados de um material com endurecimento misto.

Foi implementado um critério de dano no modelo, que simula com precisão a degradação do material através da abertura de uma fissura. Para contornar a complexidade desse critério, foi estudado um critério simplificado que é capaz de prever o ciclo de rotura através da acumulação de extensões plásticas, com um erro inferior a 2 ciclos.

Finalmente, a análise paramétrica do modelo sugere um comportamento melhorado usando o aço de alta resistência nas placas, e uma maior distancia entre as placas internas.

Palavras-chave: Analise de elementos finitos; Sistemas histerético de dissipador de energia; Critério de dano; Modelação de material; Sistemas de substituição; Perno fusível

Contents

List of figures

List of tables

List of symbols

Latin upper-case letters

C_1 Initial Hardening Parameter

D Damage Variable

E_E Experimental Energy Dissipated

E_N Numerical Energy Dissipated

E_y Young Modulus

G_f Fracture Energy Dissipation

K Stiffness

L Characteristic Length of the Element

MPa   Mega Pascal

N Newtons

Q_∞ Isotropic hardening Parameter

Latin lower-case letters

b Isotropic hardening Parameter

d Displacement

f_s Friction Shear Stress

f Force

mm millimetres

$\bar{u}^{pl}$ Equivalent Plastic Displacement

Greek lower-case letters

γ_1 Kinematic Hardening Parameter

$\bar{\varepsilon}_0^{pl}$ Equivalent Plastic Strain at Damage Initiation

$\bar{\varepsilon}_f^{pl}$ Equivalent Plastic Strain at Fracture

ε_e Engineering Strain

ε_t True Strain

ε_y	Yield Strain
μ	Friction Coefficient
ρ	Normal Pressure
σ_e	Engineering Stress
σ_t	True Stress
σ_y	Yield Stress
ν	Poisson's Modulus

Acronyms

DISSIPABLE   "Fully DISSIPAtive and Easily RepairaBLE devices for resilient buildings with composite steel-concrete structures

DE   Damage Evolution

DI   Damage Initiation

DIC   Digital Image Correlation

DRD1   Dissipative Replaceable Device no 1

ECCS   European Convention for Constructional Steelwork

ETT   Experimental Tensile Test

FE   Finite Element(s)

FEM   Finite Element Method(s)

HSS   High Strength Steel

INERD   INnovations for Earthquake Resistant Design

IST   Instituto Superior Técnico

LERM   Laboratory of Structures and Strength of Materials

Maxpe   Maximum Principal Strain

PEEQ   Equivalent Plastic Strain (scalar)

UMAT   User Subroutine

XFEM   Extended Finite Element Model

1 Introduction

Earthquake: "*A sudden violent movement of the earth's surface*(…)" [1]

Earthquakes are geological events that consist of the release of great amounts of energy, usually in less than a minute. This energy is accumulated in the Earth's crust throughout long periods in the form of potential displacements. In other words, due to the rough edges of the tectonic plates, these tend to get stuck while the rest of the plate keeps moving. Finally, when a critical point is reached, these plates detach and a sudden deformation happens. All this energy is propagated by means of mechanical vibrations through the ground and, if it reaches a structure, part of that energy will be transmitted to it. If these buildings are not capable of dissipating the transmitted energy at a reasonable rate, they might suffer costly damages, partial or even total collapse. This degree of destruction not only depends on the magnitude of the earthquake, but also on the capacity that the targeted structure has to dissipate the motion transmitted through its foundations. Due to these sporadic events, Civil Engineering studies and develops earthquake-resistant designs, in order to avoid loss of life and damage to property. These designs consist of determining the anticipated demands and providing the necessary capacity to meet these forces and/or displacements by satisfying prescribed safety and serviceability criteria or limit states [2].

The design of a building on an active seismic area must take into account the risk that it is subjected to. In Eurocode 8, for example, there are four classes of importance. From the first, where buildings of minor importance are, such as agricultural buildings, to the fourth, where vital buildings for civil protection are [2]. Consequently, three performance objectives are defined [3]:

1. Avoiding collapse - In case of a strong earthquake, it is admitted that the structure will suffer extensive damages, but it is required that it does not collapse. In these cases, it might not be possible or economically viable to repair the present building.
2. Protecting human life - Although it is assumed that the structure will suffer significant damages, it is required that it is able to withstand vertical loads without being dangerous for the people inside or around it.
3. Avoiding inactive time – This includes all the buildings that must remain functional after the earthquake's damage, such as vital buildings in post-earthquake situations (e.g. Hospitals); buildings that, if too damaged, might be dangerous to people or the environment (e.g. nuclear power plants); and, finally, important heritage buildings (e.g. monuments).

Depending on the type of structure and the required level of performance, several types of solutions can be employed. For example, in reinforced concrete structures, one of the most common methods to achieve the required protection, is to employ the capacity design concept. This proposes that it is beneficial to design structures in a way that plastic hinges can form in predestinated locations and a predeterminate sequence, without forming a mechanism. The main goal is to avoid a brittle mode of failure, which is achieved by making the plastic hinges form at the end of the beams and never at the columns of the structure [4].

The work in this dissertation was developed within the project "DISSIPABLE": "Fully <u>Dissipa</u>tive and Easily Repaira<u>ble</u> devices for resilient buildings with composite steel-concrete structures". This European project is currently developing innovative low-cost, dissipative and easily replaceable devices. Thereby, promoting buildings with an improved economy and feasibility resiliency, in a post-disaster situation. This also aims to minimize the environmental impacts and costs throughout a building's life cycle. Upon introducing dissipative devices in strategic points of a structure, these will behave as plastic hinges and avoid extensive damages to the structural elements.

This dissertation will study the behaviour of one of the devices currently in development, the DRD1 "Dissipative Replaceable Device no 1". This is a hysteretic device composed by a pin fuse that is introduced in the ends of the diagonal braces (Figure 1.1), in a composite steel-concrete building. In order to meet the specified objectives of the DRD1 study proposal, several parametric studies of this device are necessary. These studies can be performed using an analytical, experimental or numerical finite element models. This last method is considered to be one of the most effective ways to assess the system's behaviour. However, before a numerical model can be considered as accurate enough to perform a parametric study, it is necessary to calibrate and validate it. As a result, at the end of the year 2019, an experimental program was performed in eight different physical models [5].

The aim of this work is, therefore, to understand the behaviour of the DRD1 and create a numerical model capable of reproducing it, using the software *Abaqus*. To achieve this task, the experimental data available will be used to calibrate and validate such a model. The numerical methodology developed will then be applied to perform a parametric study.
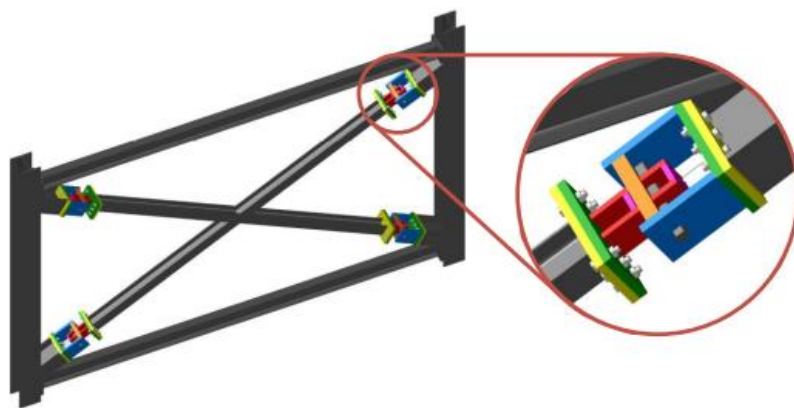
Figure 1.1 - Location of implementation of the device in a frame [6].

In short, this introductory chapter presented a general overview of the context of this dissertation and its objective. This dissertation includes seven more chapters, described as follows:

Chapter 2 reviews several types of structural control systems, then are discusses the existing developments and specifications about the device in study. At last, the existing methods that might be useful to create a numerical model of hysteretic mechanisms are explored.

All the information needed from the performed experimental tests is summarized in Chapter 3. These results are necessary for the development of a numerical model.

In Chapter 4, the methodology used to achieve the objectives of this dissertation is presented, as well as, some choices to calibrate a finite element model capable of accurately reproducing the behaviour of several devices.

In Chapter 5, the process of calibrating the material's behaviour present in the DRD1 is presented.

The most relevant results obtained for the numerical studies are presented in Chapter 6, as well as a detailed discussion on several variables and how they help in the calibration of the developed model.

Finally, in Chapter 7 and 8 are depicted some conclusions from the work described in this document as well as proposals for future work regarding this topic.

4

2 Literature Review

One of the major challenges of the present time is to reduce the loss of life and damages to structures due to seismic events. In the last decades, this problem has been studied in great detail, mainly due to new calculation methods but it has been a concern long before.

Perhaps one of the first solutions ever perceived by humans, to withstand the enormous quantities of energy released on seismic events, was the Dougong Brackets, roughly 2500 years ago (Figure 2.1). In a period of history where the variety of construction materials was low, mainly rock and wood. It was used the first wooden dendriform, a sequence of cantilevers united by a tight interlocking arrangement that made the connection between the beam and the column. With this fractal-like geometry, it was possible to forward loads from the floor above to the floor beneath transferring them, sequentially, from the uppermost bracket to the lowermost bracket of this system. The ingenious part was the fact that it had a reasonable stiffness to endure the transmission of the weight and it was able to absorb huge quantities of energy due to the lack of rigid connections between its constituents. This system can be found across China, mainly on famous palaces, but the most site is the Forbidden City, Beijing. This palace complex, in 600 years, withstood more than 200 earthquakes which some of them were devastating for the rest of the city. Making it an outstanding solution for low height wooden buildings [7].

Figure 2.1 - The prototype of a Dougong Bracket [7].

Throughout the years, new materials have been incorporated in the construction, mainly steel and concrete. With these, new designs were developed to created steel, concrete and composite structures. This dissertation will have a higher focus on the composite concrete-steel structures. The first evidence of composite solutions using metal was around 1850 when it was registered a patent on trusses using wood and wrought iron. From that point, several solutions were proposed and meanwhile concrete was introduced, marking the first steel-concrete elements [8]. Composite structures have a set of characteristics that makes it an interesting solution, for certain situations. The principal elements are the structural steel, the concrete and the connectors, whose purpose is to unite both materials and avoid slip between them (Figure 2.2). These materials although different, they complement each other [9]:

- Concrete is efficient to compression and avoids unwanted displacements from the steel elements, particular instability problems.
- Steel is efficient to tension and offers a necessary ductility in structures.
- They have a similar thermal expansion coefficient and the concrete protects the steel from corrosion and fire.
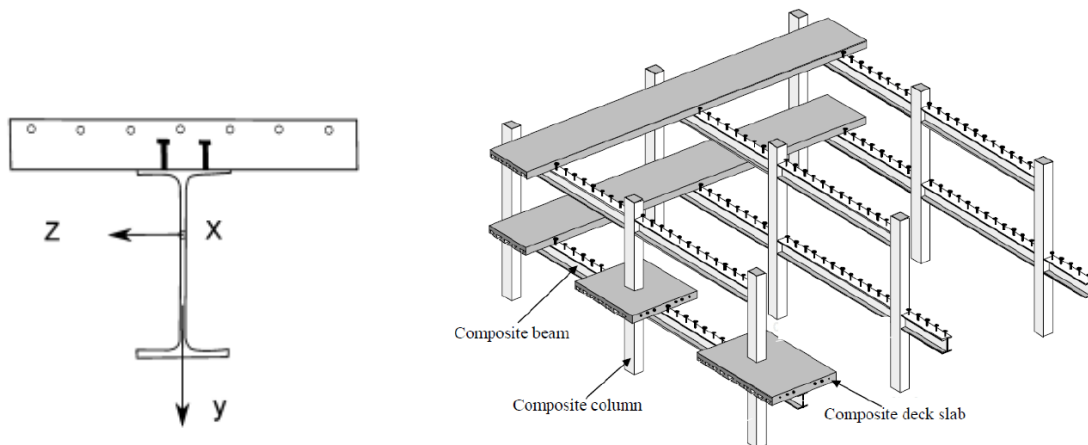
Figure 2.2 - Schematic depiction of a composite structure (right) with the common representation of a composite element beam(left) [10].

Although new types of buildings were developed, the seismic event hazard maintained a constant. When observing steel structures, these do not tend to have problems checking the necessary conditions for it to be considered earthquake resistant. These besides being constructed with highly ductile materials, they also use to be very light, comparing with concrete structures. In the other hand, in composite concrete-steel structures, there are concrete slabs which create a high concentration of weights at high levels, this addition is dangerous during a seismic event.

In earthquake engineering, the stiffness of the composite column members is one of the most important parameters of the entire structural systems since it governs the lateral resistance of the frame. Present on reference 11, a numerical study investigates the robustness of a six-level building in the event of loss of one or more columns. With careful evaluation of the beam-to-column connection and the interaction between the concrete slab and steel beams, it was concluded that it is possible to avoid progressive collapse, in that situation. Another element also used to increase the performance during a seismic event are the braces, these are effective to enhance the ductility of the structure, transfer horizontal loads and control inter storey drift. Reference 10 and 12 offers an in deep seismic analysis of this type of structure.

As stated, there are several strategies and methods to increase the seismic behaviour of a structure but in the end, these do not tend to be enough to prevent extensive damage in strong earthquakes. This damage may be so severe that post-earthquake serviceability cannot be maintained and replacement of the structure is necessary. Even if the damage is modest, the structure may be required

to be taken out of service while inspection and repairs are undertaken. Structures with class four of importance, the inactive time should be minimum. Therefore, an alternative approach to ductile deformation is sought to prevent structural damage while accommodating large displacements due to the horizontal loadings. Structural control systems are an alternative seismic energy dissipation approach that can be achieved using separate non-load bearing supplementary damping systems. This ensures continued post-earthquake serviceability by keeping the primary gravity load-bearing structure behaving elastically.

2.1 Existing methods for structural control

In a nutshell, throughout an earthquake, a certain quantity of energy is transferred to the structure. This energy is transformed in both kinetic and potential strain energy, which must be either absorbed or dissipated by heat or damage. In strong earthquakes, most building can not dissipate the received energy without extensive damage, therefore devices can be introduced to the structure to perform that dissipation. As these devices are not essential to the vertical resistance of the structure they can be damaged during the seismic event.

There is a wide range of method to achieve the desired seismic resistance. These solutions can be divided into three categories: *i*) passive systems, *ii*) active systems, *iii*) hybrid systems(Figure 2.3).
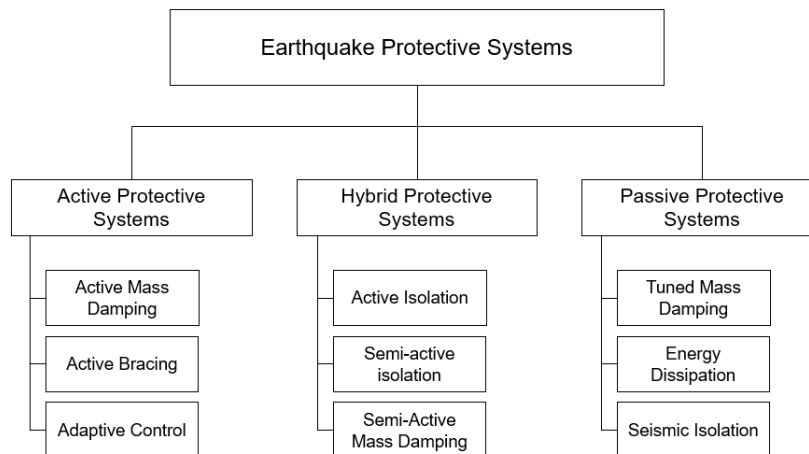
Figure 2.3 - Classification of response control systems with principal solutions for each system [13].

2.1.1 Active control systems

In civil engineering, active structural control is perceived as the solutions that actively control or modify the motion of the structure. This is achieved through the action of the control system that is powered by an external energy supply. An active protection system is composed of [14]:

- Sensors located in strategic points of the structure to measure external excitations and structural response variables.
- Devices to process the information measured by the sensors and to compute the necessary control forces needed, based on a given control algorithm.
- Actuators, usually powered by external energy sources, to implement the required forces in the structure

With these three elements combined the active system can work properly. The base task is to determine a control approach that uses the measured structural responses to calculate the appropriate control signal to send to the actuator that will perform its purpose. The most common type of actuators is the active mass damper, this consists of an auxiliary mass connected to the structure through the actuator. Depending on the external accelerations from the earthquake, the actuator will apply inertial control forces to the structure to reduce the structural responses in the desired manner. The first application of such a method was performed in Tokyo on an 11-storey structure [15].

The main advantage of this type of control is the enhanced effectiveness in response control, that theoretically is only limited by the capacity of the control system. However several disadvantages make this option unreliable. Firstly, it has a high cost in implementation and maintenance. Secondly, it is highly reliable to the external power source, if it is interrupted throughout a severe seismic disturbance, this method will not work. Thirdly, it is a complex system that requires specialised companies to implement and maintain. For these reasons, other solutions are usually explored.

2.1.2 Semi-Active control systems

Semi-active control systems work the same way as an active system but require a lot less energy. Furthermore, the necessary energy might even be storer inside the structure in small batteries, solving one of the problems from active systems. These are not dependent on any external power supply. Is short they work as passive devices where they desired properties, such as stiffness and damping, can be adjusted in real-time.

An example of such a system, are devices that used valves of mechanism controlled with electricity, to work as dampers in the structure. The mechanical devices tend to be more problematic in terms of reliability and maintenance. In the other hand, the ones that use controllable fluids have no moving parts, which increase their general reliability [16].

2.1.3 Passive control systems

Passive protective systems can be incorporated into the initial design of the structure. They consist of devices that do not require a power supply and that are capable of reducing the dynamic response of structures, either by absorbing or dissipating energy. There are several solutions o achieve this purpose,

they use a wide range of materials and devices that can enhance damping, stiffness and overall strength. After approaching the seismic isolation method, some solutions will be explored in the next subchapters.

Although not restricted to passive systems, a common solution is the seismic isolation method. This technique aims to isolate the structure from the ground to mitigate the energy that is transferred to it. This is achieved by a mechanism that introduces flexibility and damping into the structure and creates a barrier between the ground and the foundations(Figure 2.4), reducing the inertia forces induced on the building. For the elements that will dissipate the energy, generally at ground level to limit the excessive base deflection, there are three categories: viscous dampers, hysteretic dampers and friction dampers[17]. Reference 18 and 19 offers a detailed review of current solutions, evaluating then through full-scaled shake table tests.
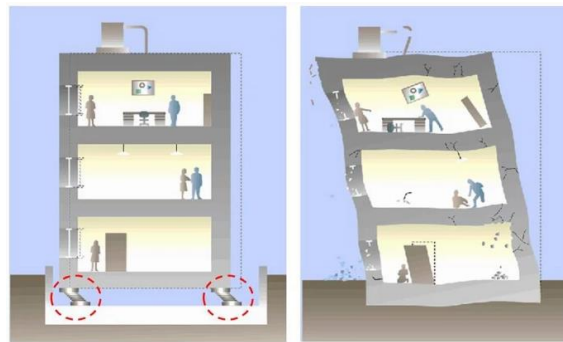
Figure 2.4 - Comparison between seismic isolated structure vs conventional earthquake-resistant structure [18].

2.1.3.1 Metallic yield dampers

Metallic yield dampers are one of the most effective mechanisms amongst the passive systems, mainly due to their simplicity and economic value. These devices can dissipate large amounts of energy that are transferred to the structure through inelastic deformation of metals. In traditional buildings, the post-yield ductility of structural elements is used to reach the required energy dissipation. Therefore, to spare these structural members, that are important to resist vertical loads, metallic energy dissipators can be added within the structure, to perform that task. Furthermore, these devices are not important for the integrity of the building regarding vertical loads, so they can go through extensive damage without short-term structural repercussions. These can be integrated into several locations of the structure, from the web of the metallic part of the beam to the braces of the building There is a wide variety of these types of mechanisms and it is a subject that is currently being highly explored. For example, reference 20 reviews and compares eight different metallic yield dampers. Note that the device studied in this dissertation is inserted in this category. There is also an interesting book that compilates several innovative anti-seismic devices [21].

2.1.3.2 Friction dampers

Friction also provides an excellent mechanism to dissipate energy and has been used, for several years, in motion brakes, such as bicycles and automobile. This phenomenon could also be explored in civil engineering, using a wide variety of material pairs (steel on steel, brass on steel, graphite impregnated bronze on stainless steel, …) to create friction in case of a severe earthquake. Although different from the yield dampers, these devices also use their hysteretic properties, as their main contributor to increasing the behaviour of the structure [22].

2.1.3.3 Viscoelastic dampers

Viscoelastic (VE) materials used in civil engineering are copolymers or glassy substances that are able to dissipate energy when subjected to shear deformations. As shown in (Figure 2.5), these devices typically consist of viscoelastic layers bonded with steel plates. When the structure is affected by a seismic event, this type o devices will dissipate energy in locations where shear forces are transmitted. They work for every type of perturbations, there is no activation level. From a strong earthquake to wind loads these elements will be active [23].
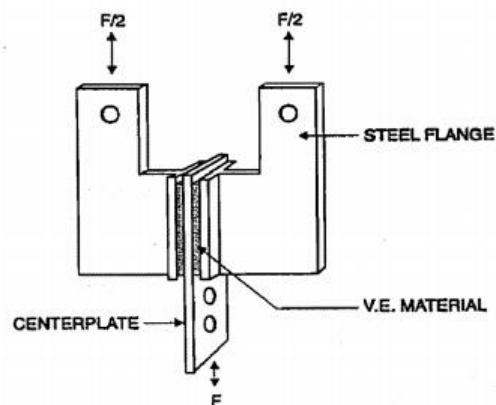
Figure 2.5 - Common viscoelastic damper configuration [23].

2.1.3.4 Others dampers

In here a short list of other dampers will be presented as well as their main characteristics.

- Viscous Fluid Dampers (VFD): These work as a piston with viscous fluid inside. The main characteristic is their viscous behaviour, where the force is proportional to the velocity.
- Tuned Mass Dampers (TMD): These consist in transferring some of the structural vibrations to these tuned mass dampers. The TMD are auxiliary mass-spring-dashpot systems that are attached to the main structure [24].
- Tuned Liquid Dampers (TLD): These are similar to the TMD but instead of a solid mass it is used a liquid mass. They absorb structural energy by viscous actions of the fluid and wave breaking.

- Ring Spring Dampers (RSD): These devices consist of inner and outer rings that have tapered mating surface, as shown in Figure 2.6. When they are subjected to compressive loads, these are affected by an axial displacement, accompanied by the sliding of the rings. This effect dissipates energy through the friction between rings [25].

Figure 2.6 - Example of a ring spring damper [25].

2.2 Overview of the DISSIPABLE project

As stated, this dissertation will explore strategies to develop a numerical model of this device, an innovative yield stress damper. This subchapter will briefly expose the essential information needed to understand the origins and the work already existent in this topic.

The main objective of developing this device is to create a mechanism capable of dissipating large amounts of energy so that the main structure does not suffer extensive damage throughout a strong earthquake. In addition, the design of the DRD1 was thought so that it would fill the lack of reparability performance, existent in other similar devices. As it is crucial to restore buildings and its functions as quickly as possible, this device was planned, so that it could be easily replaced, resulting in its considerable low weight(100Kg). This device consists of a pin fuse, mounted in the bracing system. The concept of this connection is a pin that is subjected to four-point bending which behaves in a relatively simple and predictable way. It is supposed to fail due to low cycle fatigue, by accumulating permanent plastic deformations.

In a broad sense the following points summarize the principal objective for the DRD1:

- Reduced failure probabilities;
- Reduced consequences from failure, in terms of lives lost, structural and non-structural damage, and negative economic and social consequences;
- Reduced time to recovery (restoration of a specific system to its functionality)

It is important to refer, that this solution is an evolution of a previous research project to develop innovative designs to resist seismic events. The device in question was named INERD and was developed between 2001 and 2004 [26].

As shown in Figure 2.7, these two devices have a similar concept, in their dissipative function. The main difference in this evolution is that, once the pin ① is damaged, it can be fully replaced. To achieve this, instead of welding the internal plates ③ to the diagonal member of the bracing, they are welded to a base plate ⑦ and the device is fixed to the diagonal member through the use of bolts ⑧. The connection to the main structure is identical: the external plates ② are welded to the opposite base plate ④ and this its bolts are used to fixed this end of the device. Is was also adopted spacers ⑤ and ⑥ to help the concentration of plastic deformations on the pin. Without then, like the INERD device, the external and internal plates would withstand deformation.
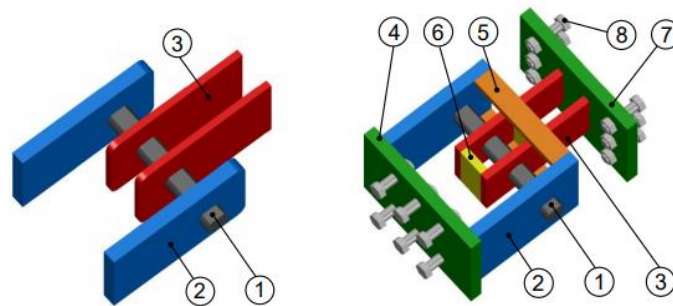
Figure 2.7 - INERD device, developed in 2004 (left) and the DISSIPABLE device, developed in 2019 (right) [6].

Although this system is being studied as independent of the rest of the structure, it was also a concern, the overall behaviour of a concentric braced frame with these DRD1's (Figure 1.1). The connections were designed so that:

- The yielding of the pin would take before compression failure of the diagonals and before yielding or buckling of the beams or columns;
- The diagonals should fail due to compression before the connections;
- The connections should fail before tension failure of the diagonals.

The safety verifications during the design of this device were performed, taking into account the recommendation from INNOSEIS [21] and INERD [26] projects which are detailed in reference 5.

2.2.1 Numerical analysis from INERD

During the development of the INERD device, it was also studied a numerical model to reproduce their characteristic behaviour. Reference 27 contains all the numerical information gathered of this project. Some key points relevant to the work developed in this dissertation will be explored.

The first software using in the study was the MSC NASTRAN MS (version 4.5), but the author rapidly noticed that it had difficulties to simulate the contact between plates and pin. Furthermore, the solver of this software was not optimized to calculate solutions with extensive inelastic displacements and high

geometric nonlinearity. This two factors made the author change the software employed to *Abaqus* (version 6.4). The numerical model was conceived as a quarter of the entire device, making use of two symmetry planes. The contact was defined with a node-to-node formulation between elements with a friction coefficient of 0.4. The whole model was meshed with C3D8R elements and an average size of 5 millimetres. Loading was applied through displacement control. Using the experimental program carried out in Lisboa, this model was calibrated. During this work, the author acknowledged that obtaining the true parameters, of the constituent material, was paramount for an accurate model, as well as, using a combined hardening material definition. Figure 2.8 compares the hysteretic curves from one of the experimental results with the model using isotropic hardening, associated with an inclined line to define the plastic range; and combined hardening with logarithmic shaped plasticity. In this dissertation, the damage criterion was not studied.
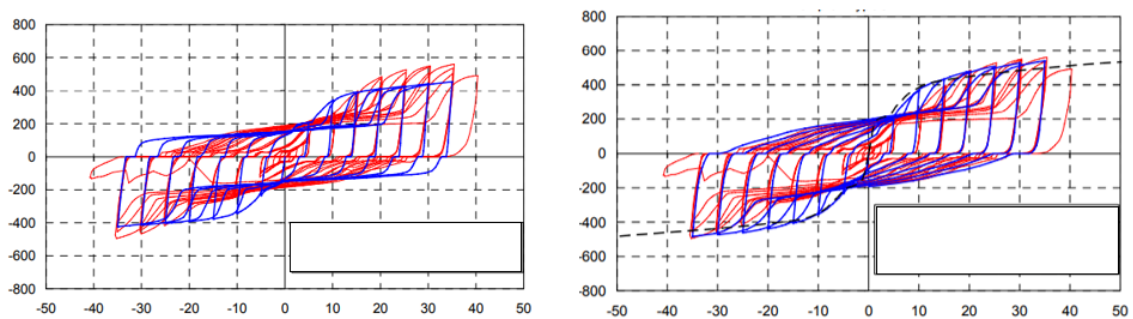
Figure 2.8 - Hysteretic curves using isotropic hardening (left) and combined hardening (right); Experimental curve(red) and numerical curve (blue) [27].

2.2.2 Numerical analysis from DISSIPABLE

As this project is still in development, there are not numerical models calibrated specifically for this device. However, it was studied the implementation of the previous model to the results of the preliminary experimental campaign of this project. Using the same specifications as before, the results were the following (Figure 2.9). Note that, as stated in reference 5, there was a difference between the expected constitutive relation on the constituents of the devices and the type of material received.
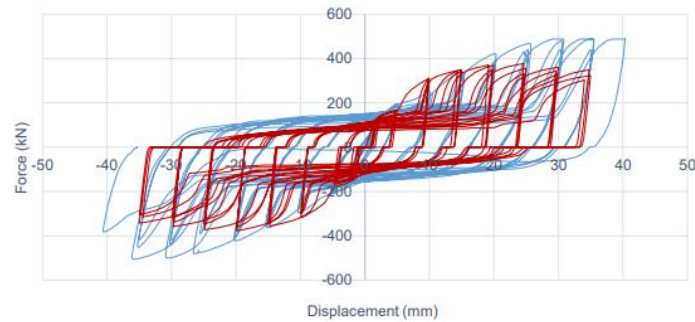
Figure 2.9 - Comparison between numerical (red) and experimental curves (blue) of test number 2.

2.3 Solving steel mechanisms behaviour

Describing the world around us mathematically is a practice quite old but it became much more important throughout the advancement of civilizations. Nowadays, it is a necessity, everything from industry to economy is highly studied to always reach more accurate results or methods. Engineering is no different, it might even be said that it exists due to this practice, characterize behaviours thought mathematical equations. When it comes to mechanisms the main focus resides in two aspects. Firstly, how do the constituent materials react to different disturbances and how can that be captured with mathematical methods. Secondly, how do different objects react with each other and can those behaviours be predicted?

In this chapter, it will be explained how the finite element method works and then it will be discussed several definitions and methods necessary for this dissertation.

2.3.1 Finite element method

The finite element method was developed around the 1940s with the necessity of solving complex problems of elasticity and structural analysis. Nevertheless, only in the 1970s did this method gained its impetus, it started being applied to all sorts of fields including fluid mechanics, mechanical optimisation and heat transmission. This is a very flexible tool because of its simple fundament: a numerical technique that calculates approximate solution for partial differential equations. When it comes to complex mechanisms such as mechanical hysteretic devices this method is indeed a powerful tool to simulate and predict their behaviour. For this type of problems, two different solving techniques can be used: the quasi-static analysis and the dynamic analysis.

Regarding the quasi-static simulations, its utility includes the ability to accurately solve problems with large displacements because this method uses a static non-linear formulation. Although it is not able to take into account dynamic effects, it was not considered a problem since dissipative devices are tested at very slow velocities, therefore impact behaviours and inertia forces are not important. There are two types of nonlinearities in these simulations, it can be geometrical or physical. The geometric non-

linearity consists of calculating the solution knowing that it is dependent on the deformations of the studied structure. So the larger the displacements are, the higher this effect is. When a simulation has small deformations, there are several simplifications that will not bring considerable error, this means that the simulation can be geometrically linear. Although if this error is considerable, non-linearity is present and acknowledging second-order effects might be paramount. Physical non-linear in related to the behaviour of a material. It means that the material cannot be only defined by Hooke's law, it also has a plastic and failure definition. This is very important in dissipative devices as their functionality resides with the capacity of plastic deformations.

The equation (2.1) is the system of equations that is used when calculation solutions with FE analysis; f is a vector that describes the field of forces, K is the stiffness matrix and d is the displacement field. Note that this equation has n degrees of freedom which is the number of nodes that are used to solve the problem. That is why the solution is usually more accurate when a finer mesh is used to describe the geometry of the problem.

$$f^n = K^{n*n} \times d^n \tag{2.1}$$

When assuming that the problem in hand is linear f and K are considered independent of d therefore, this can easily be solved directly. However, this does not happen when second-order effects are considerable, it is necessary to calculate d with an iterative process because that displacement field influences the calculation of f and K. This process consists of calculating the deformations for an initial force value that is progressively incremented. In each increment is it verified if equilibrium has been achieved, when it does, it is understood that the solution converged and force field f , of that increment, is introduced in the equation. While the displacement field f used is from the previous increment. This iterative solving method is called as Implicit. One of the main advantages of this method is that it solves the equations in each increment to achieve equilibrium, making the simulation unconditionally stable. Although it might be problematic because, in increments that the solver cant verified equilibrium, it will not diverge and abort the calculations. This usually happens with extremely non-linear problems and sometimes when damage definitions are present. In these cases, it might be beneficial to use an explicit method. Using this, the equilibrium is not checked in every increment so the solver will never stop calculating a solution. As a result, a solution might diverge and the solver will continue leading to inaccurate results. To avoid this, the force increments used when solving the equations are extremely small but divergencies might happen nonetheless [28].

2.3.2 Material modelling

The simplest way of describing a material would be using a linear constitutive relation. However, for yield dampers, it is crucial the definition of a plastic relation, so that it is capable of dissipating considerable amounts of energy. These types of devices use their hysteretic properties to achieve their intended purpose. For this reason, the constitutive relation of the material that is used in the device must include a law for the plastic domain. Another phenomenon necessary to implement is a damage

criterion so that the effects of total failure and material degradation can be captured in the numerical solutions. This is the effect that conceives an ending to the simulations, without it, two consequences would occur. Firstly, as no elements are considered to have degradation, it will sustain loads that would otherwise be distributed to other elements. Secondly, the simulations would, if allowed, run indefinitely.

The common material used in these devices tends to be mild steel, due to their price and high ductility. In general, most literature assumes steel as an isotropic material, for simplicity, although they are slightly anisotropic due to the elongation of the grains during production.

The most common way to easily obtain the constitutive relation that describes an isotropic material is thought a tensile test. For mild steel, the stress-strain curve is usually similar to the one presented in Figure 2.10, where the several phases are identified: elastic, strain hardening and necking ranges.
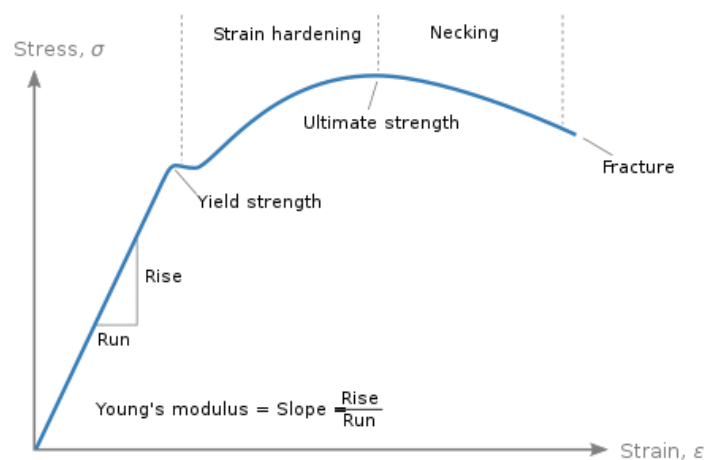
Figure 2.10 - The general behaviour of mild steel under uniaxial tension.

In the elastic range, the material is defined by the Young modulus (E_y) and the Poisson modulus (v). The first parameter defines the rigidity of the material, thus it represents the slope of this linear range. The second value defines the ration between the deformations suffered in one direction and the effect that it has in the normal directions.

To define the end of the elastic range and the beginning of the plastic behaviour is necessary to specify the yielding stress (σ_y) and the yielding strain (ε_y). The most simple way to define a plastic range is to ignore strain hardening and define it as a linear curve with a null tangent modulus, these are called as perfectly plastic materials. However, in simulations where the strain hardening is important, it is necessary to detail it. *Abaqus* software offers several options, from a bilinear definition, where a constant residual stiffness is used after yielding; to more complex definitions using parabolic progressions. The implementation of these parameters depends on the type of cyclic hardening chosen.

2.3.2.1 Cyclic hardening

When a metallic material is subjected to a cyclic load, that forces the material to experience plastic deformations, it is imperative to calibrate a hardening behaviour, which can be isotropic, kinematic or

combined (Figure 2.11). Under a cyclic loading condition, materials and structures, experience repeated tensile and compressive load which shows different behaviours with those under monotonic loading. It is observed that the yield stress changes throughout a cyclic loading. The isotropic hardening definition states that the yield surface remains the same shape but expands with increasing stress. This implies that the yield surface is symmetric about the stress axes, they remain equal as the yield surface develops with plastic strain, which goes against the Bauschinger effect. The Bauschinger effect refers to the property, where materials stress and strain changes as a result of the microscopic stress distribution of the material. For example, the increase of tensile yield strength can occur at the expense of compressive yield strength (Figure 2.12). The kinematic hardening takes into account the Bauschinger Effect and states that the yield surface remains the same shape and size but merely translates in stress space. Finally, the combined hardening is a combination of the isotropic and kinematic hardening.
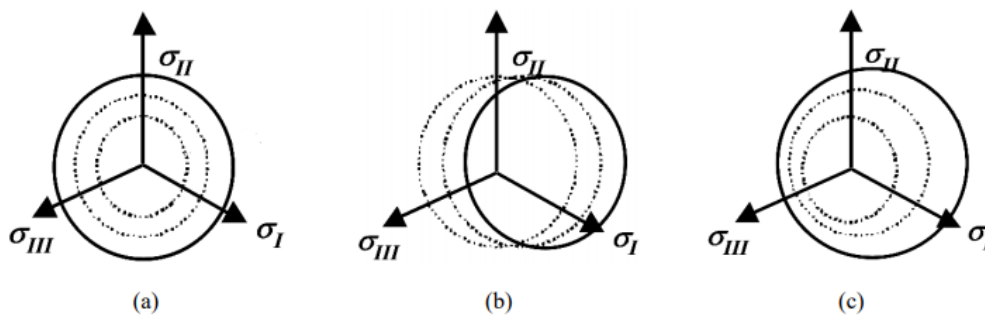
Figure 2.11 - Yield surface adaptation under plastic deformation on a principal stress space: (a) Isotropic hardening, (b) kinematic hardening and (c) combined hardening [29].
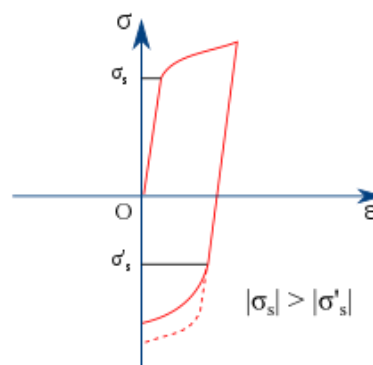
Figure 2.12 - Representation of the Bauschinger Effect.

Although there are three principal types of cyclic hardening behaviours, there is a large number of rate-independent plasticity models that have been proposed in the last decades. A comprehensive review of this field can be found in reference 30, where a review on the most relevant models is performed. Most of these are defined as a combined hardening definition because is agreed to be the most accurate

when modelling the cyclic behaviour of metals [31,32]. In the *Abaqus* software, when combined hardening is chosen, it follows the model developed by Lemaitre and Chaboche [33].

2.3.2.2 True stress-strain curve

Tensile tests are used to obtain various elastic and plastics properties of the target material. The specimen is subjected to a tensile force until failure and two arrays of values are measured during this test: the force that the machine used and the displacement between both ends of the specimen. These two values with the length and the area of the undeformed pin, it is simple to calculate the stress-strain curve. However, the desired properties cannot be attained from this curve because it is considered as the engineering curve (σ_e, ε_e). This curve does not consider the non-linear area value of the specimen through its length. To reach the correct parameters it is necessary to acquire the true stress(σ_t)-strain(ε_t) curve of the material. The discrepancy between both curves is higher through the test because the reduction of the area tends to localized on a specific point of the specimen, this effect is known as the necking. (Figure 2.13). In the pre-necking range, it is accepted that the logarithmic law can accurately perform this conversion, using equations (2.2) and (2.3) [34].

$$\sigma_t = \sigma_e \times (1 + \varepsilon_e) \tag{2.2}$$

$$\varepsilon_t = ln(1 + \varepsilon_e) \tag{2.3}$$
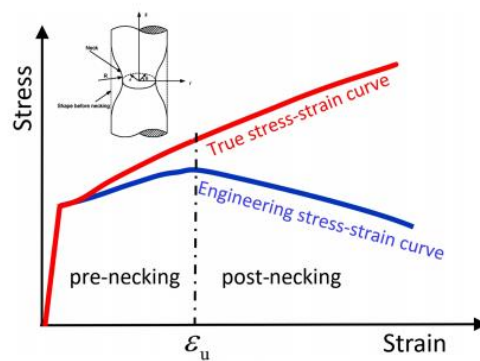
Figure 2.13 - Schematically illustration of the engineering stress-strain curve and true stress-strain curve from a uniaxial tensile test [35].

Although this is an easy and direct way to calculate the true stress-strain curve, it is important to understand that this only leads to accurate results until the highest engineering stress is reached, where consequently, the necking phenomenon starts. In other words, this analytic method is only valid when the pin has uniform deformation. When the pin stars to suffer non-linear deformations, designated as plastic instability this method is not valid. In most steels, this instability, designated as the beginning of diffuse necking, starts to develop just after a maximum load. To calculate the post necking true range, more complex methods are required to employ. There is a wide variety of studies in this field. One of the most simple methods, that is widely used in this true stress correction, is the solution proposed by

Bridgman [36]. However, this analytic solution requires continuous data on the diameter reduction and radius change in necked geometry, besides, the Bridgman equations are developed only for round cross-section specimen. Throughout the years, new analytic methods were developed but no general solution has been achieved [35]. With the introduction of finite element models to solve this problem, new solutions were developed. In general, these managed to be more precise, proposing iterative approaches to obtain the true curve, using the experimental data and FEM simulations [37]. In recent years, new experimental measurement tool of high-resolution digital camera (DIC) was employed by some researchers, to accurately define the change in the geometry of specimens [38,39].

2.3.2.3 Fracture Mechanics

The damage range of the material is associated with the necking phenomenon, in uniaxial tension of steel. With the reduction of the specimen area in a localized zone, it also reduces the capacity for the specimen to sustain loads, there is a microscopic degradation of the material. Then, this degradation leads to material failure, hence the location of necking and failure is normally coincident. Depending on the conditions of the studied material, from geometry to the type of loading, it can have several types of phenomenons that lead to material failure. Therefore, there are different damage criteria to simulate different failure modes.

When modelling steel, the most common type of failure is mostly ductile, except in certain condition, such as low temperatures, it can be brittle. Ductile damage can be perceived as the appearance of microscopic voids, that during plastic deformations tend to grow and coalesce. This phenomenon creates large localized deformations which lead to failure. This physical has been thoroughly studied and in the last years, it was developed numerical models to simulate this behaviour using microscopy images from real specimens being tested with several load cases [40].

When using *Abaqus*, the modelling of damage is divided into two steps, the damage initiation criteria(DI) and the damage evolution (DE) [28]. In the first step, there are different ways to model this according to each type of fracture mechanism that the problem might have. The most common is to use the ductile DI criterion, which is based on the void coalescence theory. The equivalent plastic strain at damage initiation ($\bar{\varepsilon}_0^{pl}$) represented in Figure 2.14, was proven to vary with the velocity of the deformation and the stress state. Therefore *Abaqus* allows implementing different values of $\bar{\varepsilon}_0^{pl}$ for different strain rate and stress triaxiality values. This might be a necessary tool for some problems but in this case, this will not be explored because to implement such plot variation, it is necessary a great deal of experimental tests to successfully calibrate the material behaviour. Nevertheless, there is a wide range of studies to calibrate these values through selected experimental procedures [41].
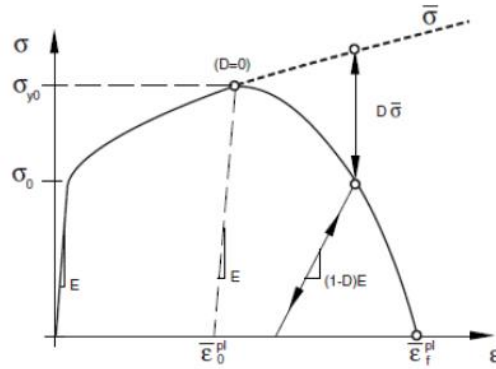
Figure 2.14 - Stress-strain curve for a material with damage initiation and evolution [28].

By definition, the DE criterion defines the degradation of the material when it enters the damage range. This degradation affects the rigidity and the yield stress of the material. This evolution can be modelled through the definition of a curve D, that starts with a value 0 at damage initiation ($\bar{\varepsilon}_0^{pl}$) and ends in 1 at fracture $\bar{\varepsilon}_f^{pl}$. The curve D can be defined using an equivalent plastic displacement ($\bar{u}^{pl}$) or potential energy dissipation (G_f). Other definitions include linear and exponential degradation. The plastic displacement, given by the equation (2.4) depends on the characteristic length of the finite element (L), thus being mesh dependent. Finally, using this definition is critical to used highly refined meshes to achieve acceptable results, which the computational cost might be unacceptably high [42].

$$\bar{u}^{pl} = L * \bar{\varepsilon}^{pl} \tag{2.4}$$

The other type of damage criteria uses the *traction separation law*. When studying fracture mechanics there are three different types of crack openings(Figure 2.15), which will propagate through the material. The first mode is characterized by the perpendicular directions between the opening of the crack and the applied load, originating normal stresses at the tip of the crack. The second mode has the plane of fracture perpendicular to the load and the third this relation is tangential, they both are defined by shear stresses at the tip of the crack. The most critical and common type of fracture is the first type, this is also the mode that happens during failure of the DRD1.

20
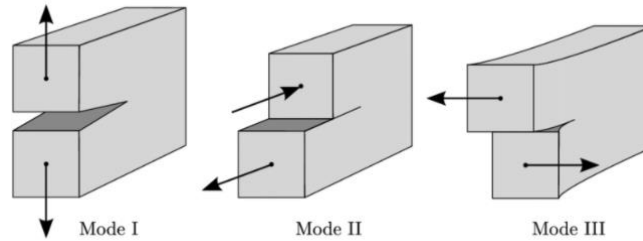
Figure 2.15 - The three fracture modes [43].

This type of fracture, exploring the opening of a crack instead of void coalescence, cannot be efficiently solved by mesh refinement with the classic FEM, so the Extended Finite Element Model (XFEM) was developed by Belytschko and Black [44] in 1999 to solve problems with this kind of discontinuities. One of the main applications of this method is the modelling of crack, from its initiation to its propagation.

In *Abaqus*, just like the ductile damage criterion, the *traction separation law* also has a DI and DE. This has several parameters to control the first criteria, such as max principle stress and max principle strain[28]. Using the options that this software offers, the possible failure mechanisms are quite limited but sometimes enough to achieve the pretended objective. This method has proven to be very versatile when combined with a user subroutine (UMAT), to define a personalized material's mechanical behaviour. The use of this coded subroutines can be used to model fatigue behaviours [45] or even to simulate enhanced ductile damage behaviours [46], also known as the Rousselier-UMAT-XFEM(RuX)

2.3.3 Contact modelling

Contact is a central matter to the present problem, since a correct formulation, allows to achieve realistic distribution of loadings and deformations in both acting surfaces. There is a wide variety of research when modelling contact formulations, especially on quasi-static conditions. As there are no phenomenons such as impact, the main focus in on the role of roughness between two microscopic contact areas. The literature on this field is reviewed in references 47 and 48, taking into account the topography and tribology of the surfaces.

Contact between two objects is perceived as not allowing the surfaces of each object to penetrate each other, so to model such an effect is necessary to define contact surfaces, which consists in the outer boundaries of the objects. The main option to use contact formulation, on finite element analysis, is to discretize the contact surfaces into a series of nodes and the most common way to define their relationship, is through a master-slave formulation. The master surface is defined by the connection of its discretized nodes, while the slave surface is defined by the group of nodes. What the finite element software perceived as contact is by avoiding the penetration of the master surface by the slave nodes (Figure 2.16). This formulation has a major disadvantage: when the contacting surfaces have coarser

meshes, the master surface might penetrate the slave surface, leading to inaccurate behaviours. When using *Abaqus* this formulation is designated as the node to surface formulation, but it is also offered the option of the surface to surface formulation, to minimize the penetration problem. This second formulation usually leads to better results in the distribution of the contact pressure over the surfaces being analysed [28].
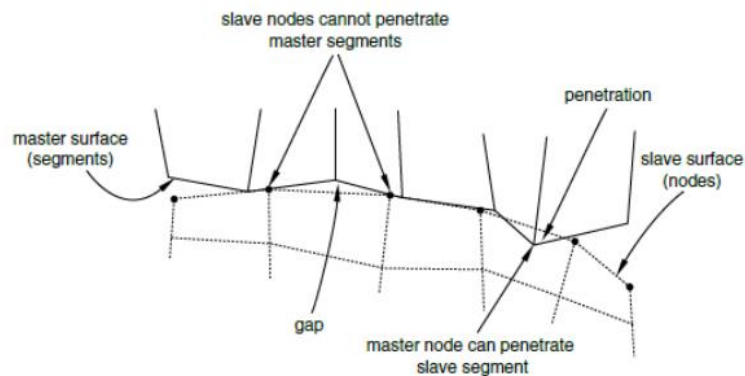
Figure 2.16 - Node to surface contact specifications [28].

In both formulations, during the analysis, the normal direction of each surface suffers discontinuities, which may lead to instabilities in the pressure distribution. Although the surface to surface formulations reduces this problem, it is also used surface smoothing algorithms to avoid entirely this discontinuity.

Although it would be optimal, the constrain of no penetration between slave and master surfaces are not strictly enforced. In *Abaqus,* there is always some penetration, even in the *hard* contact formulation, for numerical stability reasons. Besides this rigorous formulation, there are other ways to control the amount of penetration allowed, the *penalty* contact. This formulation allows slight penetration and calculates the pressure surface thought that penetration value. The effect of the master surface penetration into the slave surfaces is designated as overclosure and when this happens forces are transferred between them. In the other hand, clearance is designated as the non-transference of forces between surfaces. With this formulation, it is necessary to assign a pressure-overclosure relationship, which can be performed linearly, exponentially or defined as a matrix (Figure 2.17). In case of the hard *contact* formulation, it would be perceived as a vertical line in the exact moment where overclosure starts.
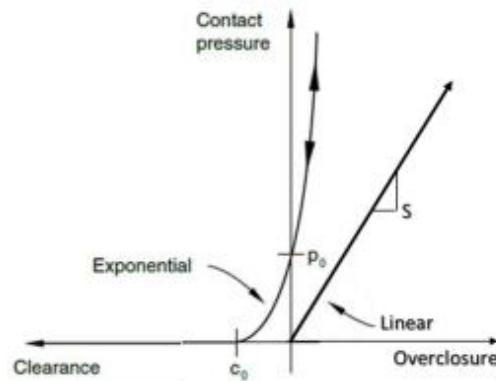
Figure 2.17 - Graph demonstration the exponential and linear pressure-overclosure relationships [28].

The software is also capable of calculating the tangential behaviour between surfaces, by a small sliding formulation or a finite sliding formulation. The first one is used when the relative motion of surfaces is small, where contact is enforced only in the initial pairs of node-surface relations, and therefore is computationally less expensive than finite sliding. The second formulation allows larger relation motions between surfaces because is can predict the possible contacts that might happen during the simulation

There are many models available to include friction between two contact surfaces. These definitions aim to describe, how does the shear forces are transmitted from one object to another. Abaqus also allows the inclusion of a friction model. The most common is the Coulomb friction that defines the interface friction shear stress (f_s) as a function of the normal pressure (ρ) and the friction coefficient (μ), as stated in equation (2.5). This theory does not depend on the mesh of the interacting objects, only of the stresses developed between these two [28]

$$f_s = \mu * \rho$$

(2.5)

3 Experimental Tests

As part of the work package number 4 of the project "DISSIPABLE", task 4.1 "Experimental tests on optimized DRD" consisted in the experimental test on single connections with DRD1 under cyclic loading. Due to the low-cost of each unit, twenty-eight full-scale devices will be fabricated and tested until failure. These tests will be conducted in the Laboratory of Structures and Strength of Materials (LERM) at Instituto Superior Técnico (IST).

3.1 DRD1 devices

The test setup is represented in Figure 3.1 and consist of 1) a foundation, 2) a beam of base 3) a reaction wall 4) an actuator 5) a double-action load cell 6) a frame of reaction and 7) the DRD type 1 to be tested. Figure 3.2 shows a top-view photo of one of the specimens during the test. The load cell used was limited to values between -500 and 500 kN, so devices that could withstand more than this, had their results capped to those limits.
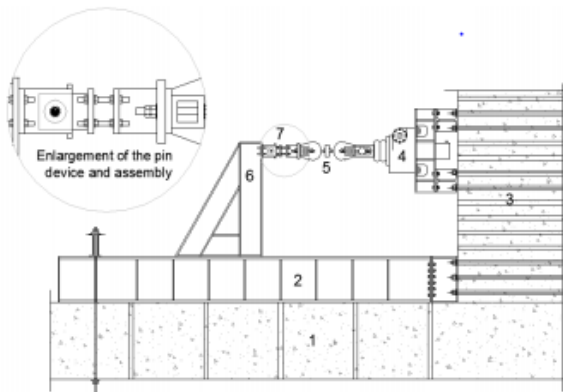
Figure 3.1 - Setup for the DRD1 tests.   Figure 3.2 - Photo of a device during the test.

Each of the twenty-eight units set (Annex A – Figure A.1), has a specific characteristic changed so that a direct comparison between two results can show the effect of that difference. In this campaign, one of the objectives was to help developing and to validate a numerical model, thus considering that the device was separated from the global structure, making it possible to analyse them at an element level.

Predicting the necessity of changing some characteristics in the devices after the first tests, it was agreed to test 8 units first and then carry on with the rest. So, if needed, small variants could be integrated into the production of the remaining specimens. This first campaign was executed from November to December 2019. Annex A – Figure A.2 identifies the 8 Specimens of this first study. Throughout the experiments, some lateral movement and consequently pin sliding were recorded, so 2 sets of guidance plates were added in their geometry. In addition, a tensile test campaign has also been conducted with samples created from the different types of steel used in the DRD1.

Four boxes with each type of pin were chosen for this first campaign but this dissertation will only focus on the specimens with a chamfered pin that have no welds applied. So only the tests number 1, 2, 3 and 4 will be used in the development of the numerical model. The full report on these preliminary tests can be read in reference 5

These four boxes were measured before being submitted to the cyclic loading and all of them had a geometry very close to what was expected (Figure 3.3). There were some discrepancies in the order of a few millimetres, which given the size of the box did not bring relevant changes.
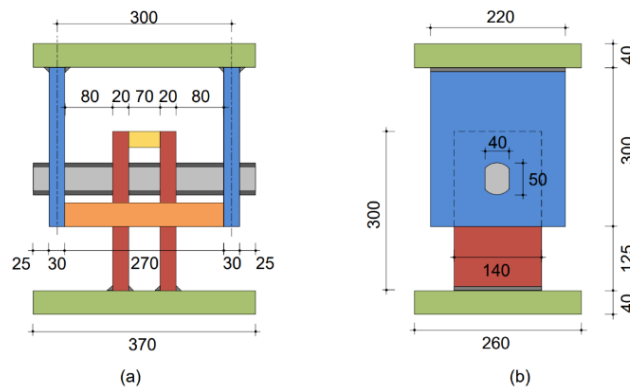
Figure 3.3 - DRD1 first campaign geometry: (a) top view and (b) side view, dimensions in mm.

3.1.1 Test number 01

The device number 1 (code 01-R_S235_S355_E) had a chamfered pin produced by SOFMAN. The cyclic load applied that followed the European Convention for Constructional Steelwork (ECCS) protocol [49] is in Figure 3.4, the horizontal axis does not have a specific dimension but is proportional to time. The force-displacement graph is shown in Figure 3.6. This test did not achieve failure (Figure 3.5) because it was stopped when load forces reached 500kN (which was sooner than expected), The remaining would not be correctly captured due to the load cell limitation. The hight force at such an early phase was due to the steel grade of the SOFMAN pin which was higher than expected. Therefore, IST manufactured other chamfered pins with a lower grade for the other three devices, they were designated as the IST pins.
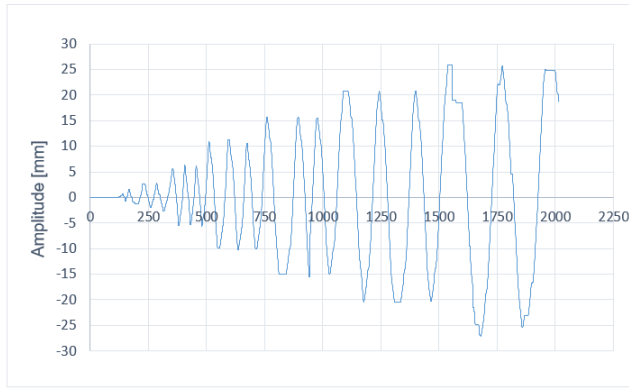
Figure 3.4 - Recorded displacement of the load cell in test number 1.

Figure 3.5 - Tests performed in the first campaign at the end of 2019.
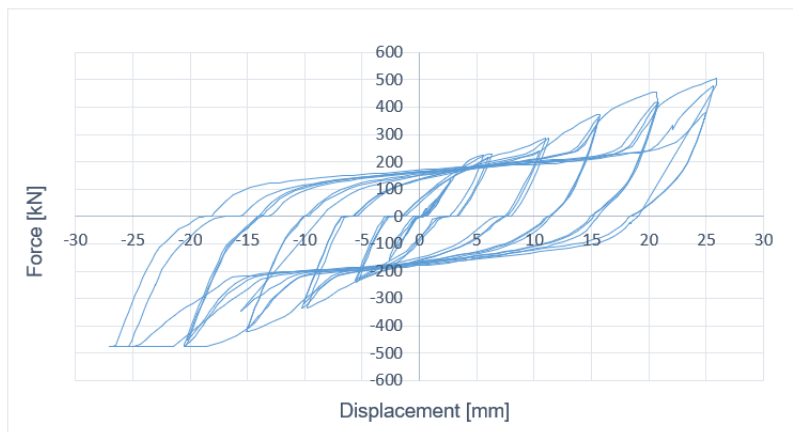
Figure 3.6 - Hysteretic curves obtained from the first test.

3.1.2 Test number 02

The device number 2 (02-R_S235_S355_E) had a chamfered pin produced by IST. The cyclic load applied that followed the ECCS protocol is shown in Figure 3.7 and Figure 3.9 represents the force-displacement graph. This test achieved failure (Figure 3.8) located in the mid-span of the pin and ovalization of the holes in the plates was observed.
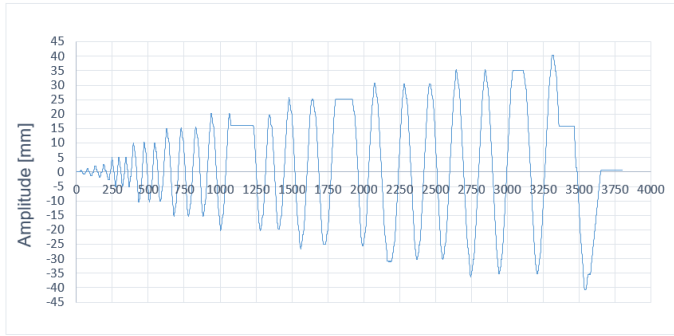
Figure 3.7 - Recorded displacement of the load cell in test number 2.

Figure 3.8 - Top-view photo at the end of the experimental test.
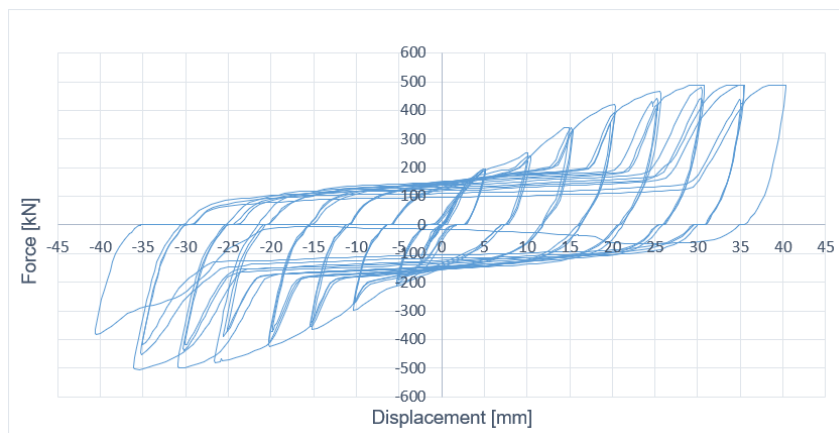
Figure 3.9 - Hysteretic curves obtained on the second test.

3.1.3 Test number 03

The device number 3 (code 03-R_S235_S355_C1) had a chamfered pin produced by IST. The cyclic load following constant pattern is shown in Figure 3.10 and the force-displacement graph is shown in Figure 3.12. This test also achieved failure (Figure 3.11) located in the mid-span of the pin and ovalization of the holes in the plates was observed.
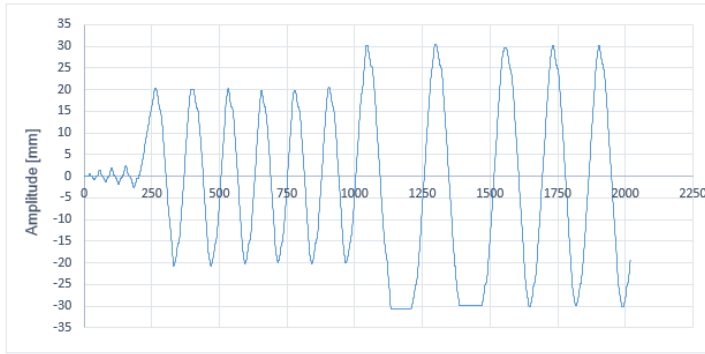
Figure 3.10 - Recorded displacement of the load cell in test number 3.

Figure 3.11 - Top-view photo at the end of the experimental test.
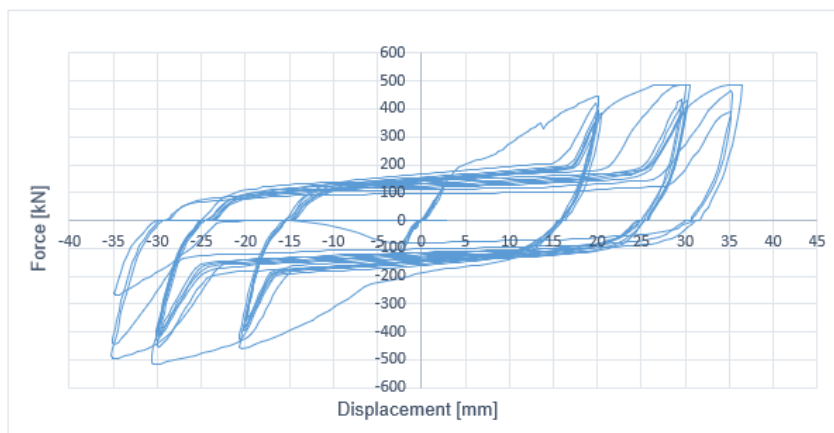
Figure 3.12 - Hysteretic curves obtained from the third test.

3.1.4 Test number 04

The box number 4, code 04-R_S235_S355_C2 had a chamfered pin produced by IST. The cyclic load following constant pattern is shown in Figure 3.13 and Figure 3.15 represents the force-displacement graph. This test also achieved failure (Figure 3.14) located in the mid-span of the pin and ovalization of the holes in the plates was observed. Take special attention to how the irregular displacement affected the hysteretic curves.
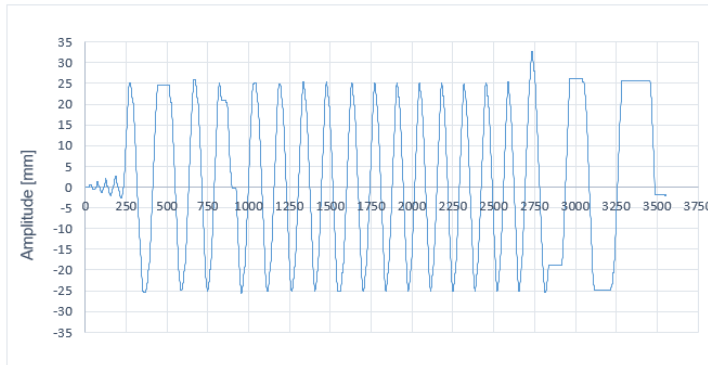
Figure 3.13 - Recorded displacement of the load cell in test number 4.

Figure 3.14 - Top-view photo at the end of the experimental test.
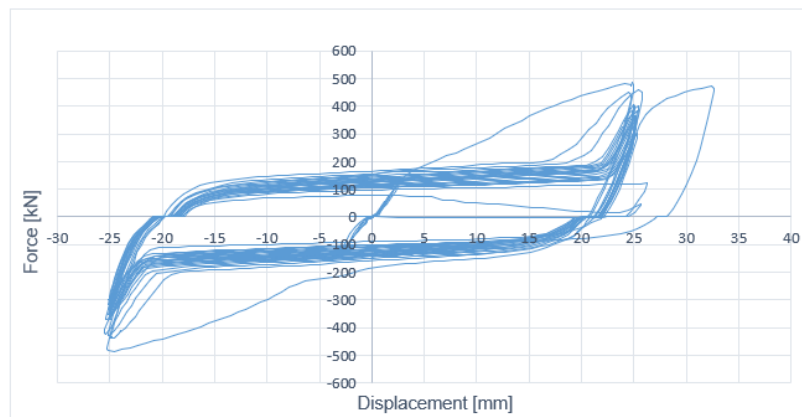
Figure 3.15 - Hysteretic curves obtained from the fourth test.

3.2 Tensile tests

As seen in Table 3.1 there are three types of material: the IST material, the SOFMAN material and the plate material. Although the grade of each steel was known, for better accuracy a tensile test campaign was performed for each type of material [5] in the same facilities as the DRD1, using the Instron machine with 250kN strength and 100mm displacement range.

Ten coupons specimens were created from the several plates that constitute the devices and as they had a similar result, it was assumed that the first test (1EP355) could represent every plate element. Other 2 tests were performed with specimens created from an untested SOFMAN pin and, again, they had similar results. Thus, the test 13PIN235 was assumed to successfully represent this material. Lastly, a specimen from the IST material (15PIN235) was tested. The pin geometries are listed in Table 3.1 and the stress-strain curves for each test are represented in Annex B – Figures B.1-B.3.

Table 3.1 - Identification and geometry of the chosen tensile tests.

Test name – material designation	Initial length (mm)	Section dimension (mm)
1EP355 – Plate material	180	29.72 X 151.35
13PIN235 – SOFMAN material	180	Ø 19.99
15PIN235 – IST material	165	Ø 20.15

3.3 INERD devices

Within the scope of the INERD project, a campaign of dissipative devices was tested [26]. These tests will be used in the model validation. For that matter, three devices were chosen: two with a chamfered pin with different internal plate measurements and one with a rectangular pin.

The test "c50_eccs" had a chamfered pin with a 50 mm distance between internal plates. The Hysteretic curve and failure mode are displayed in Figure 3.16 and Figure 3.17, respectively
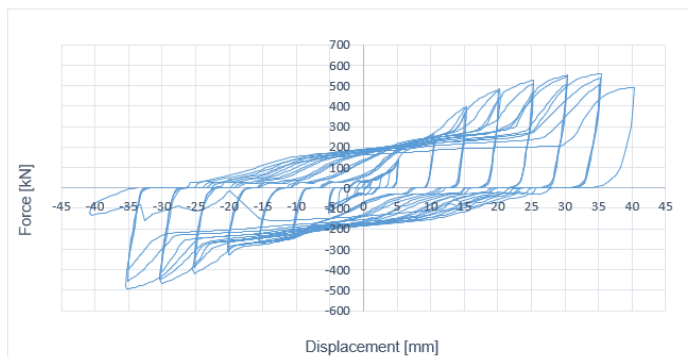
Figure 3.16 - Hysteretic curves obtained from test "c50_eccs".
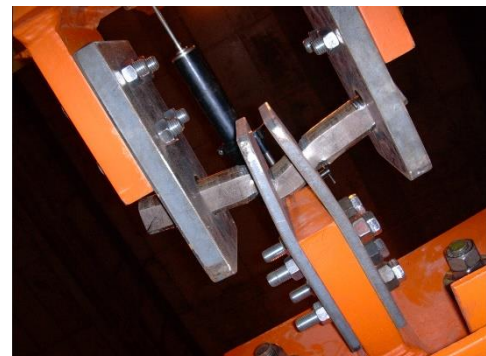
Figure 3.17 - Bottom-view photo at the end of the experimental test.

The test "c70_eccs" had a chamfered pin with a 70mm distance between internal plates The Hysteretic curve and failure mode are displayed in Figure 3.18 and Figure 3.19, respectively
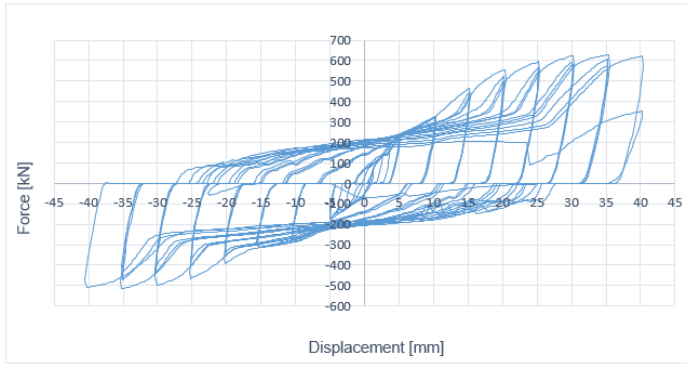
Figure 3.18 - Hysteretic curves obtained from test "c70_eccs".

Figure 3.19 - Photo at the end of the experimental test.

The test "r70_eccs" device had a rectangular pin with a 70mm distance between internal plates. The Hysteretic curve and failure mode are displayed in Figure 3.20 and Figure 3.21, respectively
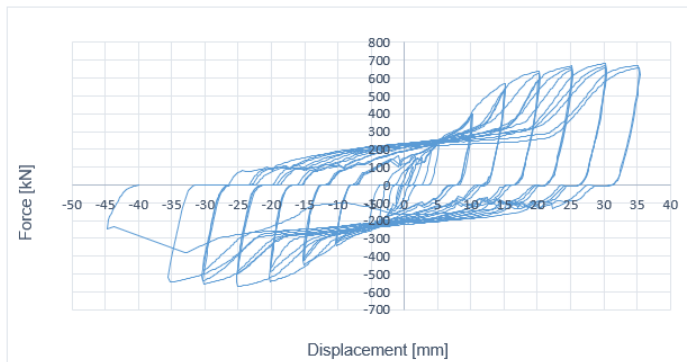
Figure 3.20 - Hysteretic curves obtained from test "r70_eccs".
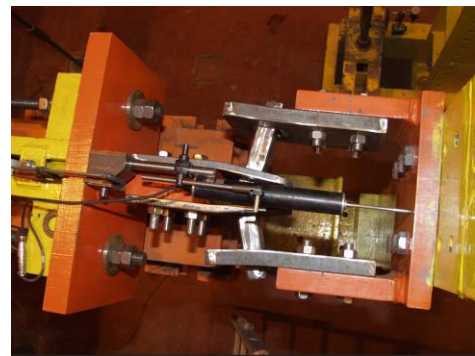
Figure 3.21 - Top-view photo at the end of the experimental test.

4 Numerical Methods and Methodology

To reach the goal of creating a model capable of reproducing the behaviour of a DRD1 device, the Software Abaqus was used. Through this tool and using the state of the art discussed in Chapter 2, a research methodology was developed. As this problem had too many variables, it was not possible to follow a sequential methodology. In other words, it was not possible to fix a value on a variable taking into account only one scenario/test. For this problem, a more cyclic path needed to be explored. The only parameters that could not be modified were the geometry and the load history of each device, those 2 variables are intrinsic to each test. For the rest of the parameters, it was necessary to evaluate and calibrate it.

The methodology used to develop the numerical model is summarised in the flow-chart (Figure 4.1). Firstly, a test geometry was chosen and implemented in the numerical software. On this, several variables were studied to achieve a similar response to the corresponding experimental test. Upon success, another experimental test was chosen and numerically tested with the same values as the one before, changing only the load history, the geometry and, in some cases, the material.
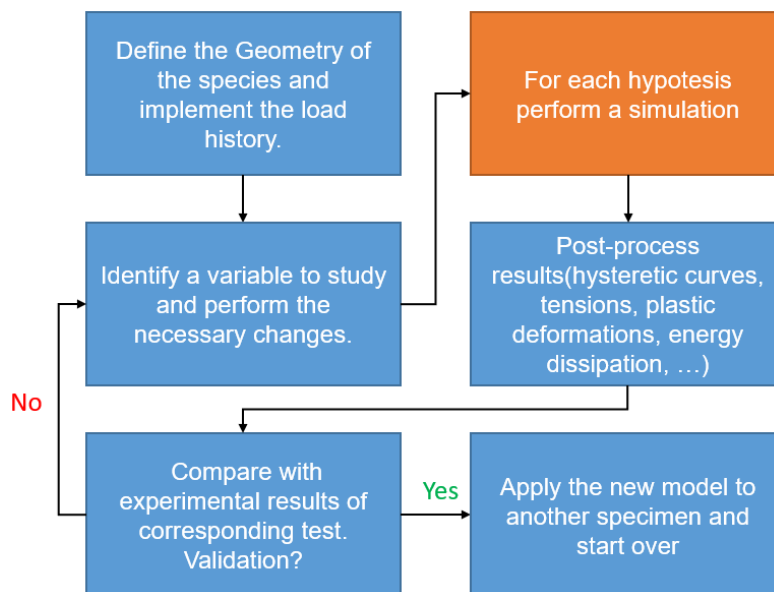
Figure 4.1 - Flow-chart of the general methodology used.

4.1 Software description

The finite elements modelling was performed using the software *Abaqus*. The program has three distinct stages: pre-processing, simulation and post-processing.

On the first stage, pre-processing (*Abaqus/CAE*), the user defines the problem. A data file, where all the necessary information is stored, is created and this can be done through a graphic interface or imported

as a text file. The first option was used throughout the project because it facilitates the development of complicated geometries.

The second stage, simulation, is a background process that will calculate the equations that are needed to solve the numerical problem. It receives the file from pre-processing and produces an output file, which has all the information about the solution. As discussed, this stage can be solved using *Abaqus/Explicit* or *Abaqus/Implicit*. The duration of a simulation depends on the processing power of the hardware used as well as all the information implemented, this operation can go from several minutes to days.

The third stage, post-processing (*Abaqus/CAE*), receives the output file and converts it into a graphic solution. In there, all the information can be visualized and there is a vast list of tools that can be used to interpret the information.

Although two distinct models were developed for this work, tensile test and DRD1 boxes, both are similar in conceptual terms. Thereby, this small description will regard both models but only the DRD1 box needs all theses modules, the tensile test simulations will not require an "interaction" module. The first step was to draw the geometry of the specimen in the "Part" module of *Abaqus/CAE*. It works like a 3D graphic design software, with the exception that every constitutive piece is shaped individually and allocated in the "Assembly" module. The next step is "Properties" in which the material properties are assigned to the parts. Then, the loads and the boundary conditions are applied in the "load" module. When necessary in "Interactions", those can be defined and applied to the geometry, including uniting two different pieces to work as one. In "step", the simulation method is defined and also the data that should be provided in the solution. The last task is done in the "mesh" section which, from a vast library of finite elements, are applied to all the parts as intended. With everything specified, on the "job" module, we can apply to the selected solver. Upon concluding this, the solution can be opened and studied in the "Visualization" section.

As this program does not work with pre-established units, any metric scale can be used but special attention is needed to achieve consistency. All physical quantities used throughout this dissertation, on *Abaqus,* are defined in the following Table 4.1

Table 4.1 - Units used in the software.

Length	Force	Time	Stress
Millimetres	Newtons	seconds	Mega Pascals
mm	N	s	MPa (N/mm^2)

4.2 Analysis procedure

For this work, it is important to obtain extensive information about the behaviour of a complex device being subjugated to a load history, so the finite element method in more efficient than others approaches such as analytical or empirical.

As stated in chapter 2, there are two types of solvers: the *Abaqus/Explicit* and the *Abaqus/Implicit*. Even though most authors use the first, upon some tests and consideration, the implicit solver was perceived as the most suited for this work. The explicit solver is commonly associated with a dynamic FE analysis, which is a powerful tool capable of delivering good results for problems with inertia effects and velocities perturbations. The implicit solver is mainly used for quasi-static problems.

The first reason why the explicit solver was not used is the fact that both our experimental test types were performed using slow displacement velocities. Therefore there was no use for calculations of inertia, impact or time-dependent effects, such as creep, swelling and viscoelasticity. Our tests could be considered as quasi-static, that is commonly simulated with the procedure called "Static, General", which uses *Abaqus/Implicit* as the solver.

The second reason for not using the explicit solver is related to material behaviour. Although another advantage of dynamic analysis is the capability of developing local instability phenomena and calculate more easily highly non-linear problems, there was no necessity of this, because, with solid 3D objects, local instabilities are not a problem, all objects were robust enough for this effect not to happen.

The final reason why the explicit solver was discarded, was to achieve a more robust model. Firstly, we are trying to create a model capable of being applied to several different specimens, so we need something and can be easily changed from one box to another. In order for *Abaqus/Explicit* to obtain good results, it needs a specific study to find the parameters that will lead to a close solution. On the other hand, *Abaqus/Implicit* is capable of creating a model that is not dependent on the specimen specifications. Secondly, although the explicit solver can always reach a solution, it does so at the price of accuracy. On the other hand, the implicit method uses equilibrium as a mean to solve the equations, leading to higher accuracy. Also, as it was possible to create a model capable of converging for these simulations with an implicit solver, there was no reason to not use this method.

Table 4.2 summarizes the values that were changed from the default in the "Incrementation" section to be able to run the DRD1 and the tensile tests simulations, achieving accurate results. Besides this, in the "General Solutions Controls", the solver was forced to iterate each increment 30 times ($I_A = 30$) instead of 5. This change is especially useful to run problems with damage criteria, without aborting. The option "NIgeom" was toggled on, so the solution could capture the geometric non-linear effects.

Table 4.2 - Solver's parameters used in the "Incrementation".

Type	Maximum number of increments	Initial increment size	Minimum increment size	Maximum increment size
Values	10^7	0.01	10^{-18}	0.1

4.3 Hardware specifications and run time condition

In this project, three different machines were used. Because two of them had similar specifications and equal run-time solving the same simulation, they will be assumed as equal devices. Thus, there are 2 different hardware, type A and type B, shown in Table 4.3.

Table 4.3 - Hardware specifications of the machines used.

Machines	RAM	VRAM	Processor	Cores	Cores used on *Abaqus/implicit*
Type A	16 Gb	8 Gb	i7 9700k	8	6
Type B	8 Gb	NA	i7 7500	4	3

Type A machine would normally be used to run the heavier DRD1 simulations and Type B for the other ones. The criteria to know when a model was too difficult to run, and therefore not useful as a tool for this study, was that a simulation would take more than 36 hours in the type A machine. This only happened for some of the heavier simulations, featuring finer meshed and complicated specifications.

4.4 Element type

The choice of what type of element to use is important when developing a model since it is the parameter that rules how all calculations are performed. From the vast library of elements available in *Abaqus/CAE*, a three-dimensional solid element was chosen for stress/displacement analyses. For our problem's specifications, the C3D20 and C3D8 elements were the most appropriate. Both are designated as a brick element, one with 8 integration points and the other with 20. As shown in Figure 4.2, the first is a linear element and the second a quadratic element, because each edge is defined by two and three integration points respectively. For bending and contact problems, the later one is quite useful, but because it leads to heavier calculations, the first one was used throughout the project. Although the solution could lose accuracy, this did not happen because the model had enough elements to avoid this. Also, the reduced integration option was used to simplify the calculations inside each element. This final element is called C3D8R.

Figure 4.2 - Representation of a linear element 8-node brick, C3D8 (left) and a quadratic element 20-node brick, C3D20 (right).

4.5 Tensile test simulations

As stated in the experimental section, several tensile tests were performed with specimens machined from DRD1 boxes. From those, stress-strain curves for each test were calculated, but as discussed in the state on the art, they correspond to the engineering values. These values do not accurately represent the true behaviour of the material, so the engineering stress-strain curve cannot be used as the constitutive relation of the material to be implemented in the calculation software.

For the DRD1 simulations, it was necessary to develop a methodology to obtain good approximations of the true stress-strain values from the engineering values. Even though there is a wide variety of studies on this topic, these could not be directly applied in our case, because we used a specific type of cyclic hardening(combined hardening) and the area where necking developed was not measured. The combined hardening has an indirect way of implementing the material behaviour on *Abaqus*. The developed methodology uses the simulation of tensile tests in *Abaqus*, replicating the experimental test, to successfully reach a close approximation to the real behaviour of the required material. It is important to understand that the logarithmic law that converts an engineering stress-strain curve to a true stress-strain curve (see chapter 2.3.2.2) is only a good approximation up until the maximum stress is reached. Consequently, the range that includes necking and damage is not accurately described.

In conclusion, it was necessary to develop a new method that could accommodate all the requirements of the present work. First, the type of material will be explained, how to input the information in the software and how to compare the stress-strain curve with the variables used by *Abaqus*. Then, the creation of a tensile test to assess the behaviour of the material parameters, and finally, the process of calibration, using these two tools.

4.5.1 Material properties

To define the properties that characterise our material, an elastic-plastic type of definition was used: an elastic set of values to replicate the Hooke law and another set for the plastic zone. For the first part, an Elastic Elasticity function in Abaqus was used, the type chosen was isotropic which is the most common for metals. In this specification, two values are required: *Young's Modulus* (E_y) and the *Poisson's ratio* (v), both available in the literature. For the second part, it was chosen the same type of cyclic plasticity used in Pavlos's PhD thesis [27], on the calibration of the material from the INERD project. It consists of the plastic plasticity function with combined hardening (data type: parameters). It requires three values: *the yield stress at zero plastic strain (f_y),* the *initial hardening parameter (C_1)* and the *Gamma 1 (γ_1)*, that defines the rate at which hardening modulus starts to decrease as the plastic strain develops. These last two are constants that define the nonlinear kinematic hardening part. It was also used a sub-option called *cyclic hardening* (with *parameters* option). It is characterized by three other variables: *Equiv stress (f_y)*, *Q-infinity (Q_∞)* and *Hardening param (b)*, equivalent to the isotropic hardening part. Although some of the variables can be taken from a simple tensile coupon test, others need a more complex approach.

Regarding the combined hardening parameters needed in *Abaqus,* the input information is not a list of values that represent the plastic curve but is rather defined by the plastic parameters in the previous paragraph. To be able to compare the material behaviour implemented in *Abaqus* with the experimental curves, the differential equations from Lemaitre and Chaboche [33] were used to understand the curve that these plastic parameters represent.

The plastic strain array is defined from the yield strain (ε_y), and a plastic increment ($\varepsilon_{increment\ i+1}$) that controls how defined the curve needs to be equation (4.1). The lower this value the smoother the curve, and for this work, increments of 0,002 were used.

$$\varepsilon_{i+1} = \varepsilon_y + \varepsilon_{increment\ i+1} \tag{4.1}$$

Now, for each value of strain (ε_{i+1}), the corresponding stress (σ_{i+1}) was calculated using equations (4.2) and (4.3), with σ_1 equal to the yield stress(f_y) and α_1 equal to 0. The variable α only has calculation purposes, it does not represent an important mechanical parameter.

$$\sigma_{i+1} = f_y + \alpha_{i+1} \tag{4.2}$$

$$\alpha_{i+1} = \alpha_i + \left(C_1 * \frac{1}{f_y} * (\sigma_i - \alpha_i) * (\varepsilon_{increment\ i+1} - \varepsilon_{increment\ i}) - \gamma_1 * \alpha_i * (\varepsilon_{increment\ i+1} - \varepsilon_{increment\ i}) \right) \tag{4.3}$$

Until here we have the equations necessary to define the material with nonlinear kinematic hardening. To define combined hardening, we still need to have into account the isotropic contribution, which is expressed in equation (4.4).

$$\sigma_{combined\ i+1} = f_y + \alpha_{i+1} + \left(Q_\infty * \left(1 - e^{-(b * \varepsilon_{increment\ i+1})} \right) \right) \tag{4.4}$$

Together equations (4.1 - 4.4)can be used to directly compare the modelled curves with the experimental tensile test curves.

4.5.2 Model development

In order to create a model to study the material parameters, it was only necessary to define the specimen geometry, which was measured during the laboratory campaign. In *Abaqus/CAE*, for each test study, the geometry needs to be implemented as a 3D solid. Then, attribute the material values to be tested, using the type of material already discussed. These are the only parameters that are changed throughout the analysis. The pins (cylindrical or parallelepipedal) were meshed an approximate global size of 2mm, with C3D8R elements. This is enough to have accurate results and a fast run-time in the hardware type B, around 20 min. As for the boundary conditions, one end of the pin was fixed and the other had only the ZZ direction free (direction of the pin elongation), where a continuous displacement was applied. Regarding the geometry and the boundary conditions, both numerical model and experimental test can be compared in Figure 4.3,

Figure 4.3 - Photo of 15PIN235 before the test (left); geometry and boundary conditions of the corresponding numerical model in *Abaqus/CAE.*

4.5.3 Calibration process

To solve the stated problem in this chapter, the following methodology was used:

1.   Identify the experimental tests with the material that is desired to characterize, acquire the geometry of the specimen and its result: the engineering curve;

2.   From the equations explained gather the set of values that define the plasticity, so it is similar to the curve from the experiment;

3.   Create the model in *Abaqus/CAE* with the correct geometry and implement the values that originated from the previous step;

4.   Run the simulation, save the reaction on the fixed end of the pin and the displacement of the other end. From these values create the stress-strain curve of the numerical test;

5.   Compare the curve from the fourth step with the curve of the experimental test. These two can be directly compared because they are engineering values. In both tests, we are measuring the reaction and displacement of opposite ends, neither consider the specimen area variation;

6.   Until the curves are similar to each other, change the plastic parameters and run the model again. Once they are similar, the definition that was implemented in the program is a good approximation to the true behaviour of the aimed material.

With this study performed, it is possible to study the DDR boxes using a close estimate of the true stress-strain relationship of the materials used in these tests.

4.6 DRD1 simulations

With the numerical characteristics defined, an overview of the construction of the prototype will be described. In particular, how the geometry was implemented as well as other necessary definitions. From a base numerical model, of the device in study, capable of converging, the influence of certain parameters was studied in order to define a final model, that can usefully predict the behaviour of similar specimens. This was achieved in three steps. First, a calibration was performed to understand the influence of different parameters. Then, some reasonable approximations were studied for several DRD1, including the damage criteria. Finally, a validation study was performed with devices from the DISSIPABLE project and the INERD project.

4.6.1 Geometry definition

The first task was to define the reference system and, for consistency, all tests were performed with the unidirectional load applied in the X-direction. The specimen was modelled with no symmetric simplifications (Figure 4.4), in order to better capture the effects of non-linearity and damage. Although a simplified version (Figure 4.5) was useful to reach a base numerical model capable of converging, after that, the full version was used for the rest of this project.
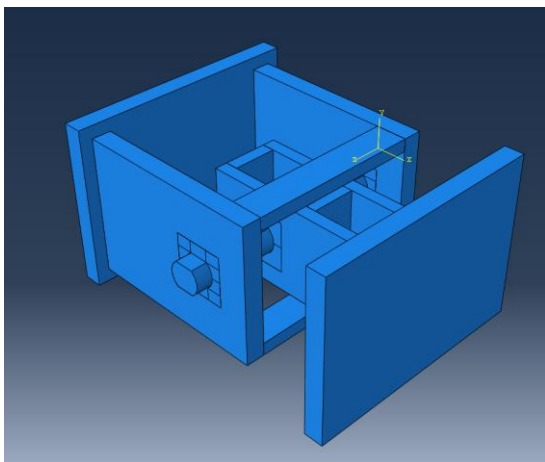
Figure 4.4 - Geometry of the model with no symmetric simplifications.
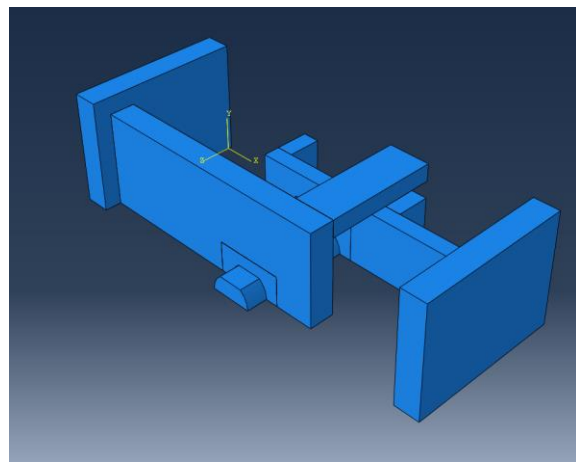
Figure 4.5 - Geometry of the model with two planes of symmetry.

As shown in Figure 4.6, this device is composed of several pieces. Each part was modelled individually in the "part" section with the same dimensions and in "Assembly" all elements were positioned in the correct place. For a better approximation in the contact region, both internal and external plates were divided in two. Thus, creating two new parts designated as External and Internal detail which have a tighter mesh to achieve its purpose. All parts are identified in Figure 4.6. In order to achieve a unified mechanism, all the parts that were supposed to be connected were done so by using the function *Tie.*

This includes the connection of the spacers to the lateral plates, the lateral plates to the base plate in both sides and the unification of each Detail to the correspondent Plate. The only geometric uncertainty was the gap between the pin and the plate details, and this measurement was defined through the calibration in section 6.1.1 to the value of 0.75 mm (Figure 4.7).
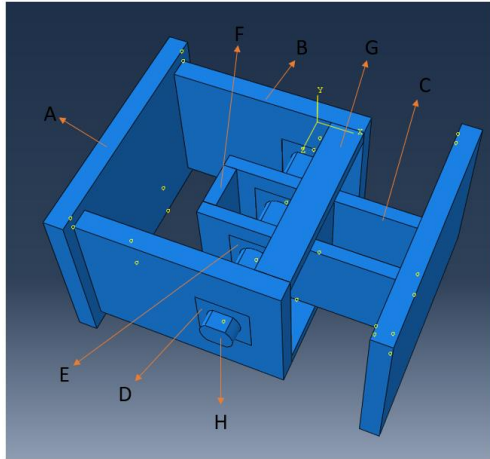
Figure 4.6 - Designation of each part. A - Base Plate; B - External Plate; C – Internal Plate; D – External Plate Detail; E – Internal Plate Detail; F-Internal Spacer; G – External Spacer; H – Pin.
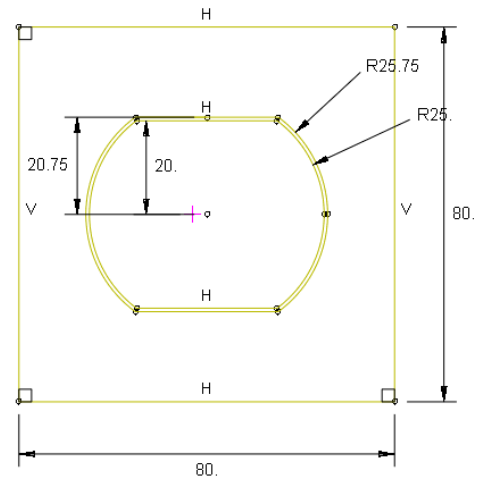
Figure 4.7 - Dimensions of the gap and external detail plate implemented in Abaqus, the internal detail plate has a circular shaped hole.

The finite element method is a numerical technique, so all the solutions calculated are approximations, therefore, it is important to have high mesh densities to achieve more accurate solutions. However, it is important to keep in mind that the problem cannot take too much time to be solved, otherwise, it becomes less practical to perform parametric studies. Since the type of element is already defined, it is only necessary to apply the most appropriate mesh dimensions. For the elements that do not reach the yield stress, a mesh around 15 mm was sufficient to serve their constructive purposes, this includes the External Plates, the Internal Plates and the Spacers. The parts that withstand extensive deformations, namely the Plate Details and the Pin, were refined with values around 4 to 7mm. In the other hand, the base plates had very small strain values, thus it could be described with a mesh of 35 mm. In Figure 4.8, an example of a standard meshing solution is presented, the different zones can be observed and most importantly the tighter mesh in all the zone that will suffer most of the plastic deformation.
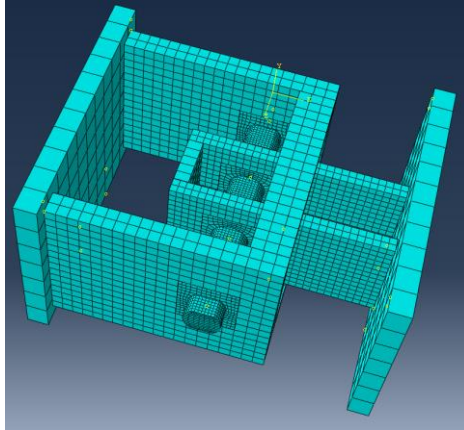
Figure 4.8 - Mesh dimensions of a generic example that achieve accurate results.

As shown in Figure 4.9 the boundary conditions were applied in the same method as the tensile test. The Base Plate that is attached to the External Plates was fixed and the other end had only the Y and Z directions fixed. The load history of each corresponding tests was applied in this plate on the X direction. It might appear that the boundary conditions are applied to the edges but that is not the case, it is only the way *Abaqus* represents them. In fact, they are applied to the whole surface.

The hysteretic curves of each simulation were calculated so that they could be compared with the experimental results. For this, the reaction force of the fixed base plate was gathered throughout the simulation. With the displacement of the movable base plate, it was possible to calculate the hysteretic curves.
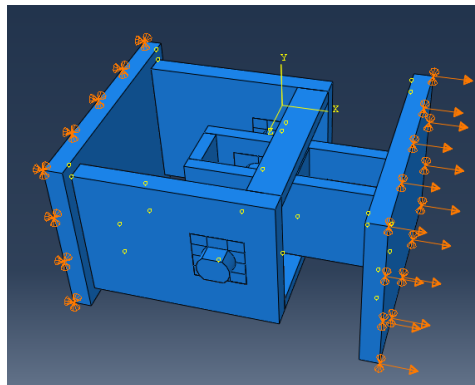
Figure 4.9 - Boundary conditions used for DRD1 marked through orange spots around the surface that they are applied, the unitary displacement is also visible.

4.6.2 Load cases

To correctly replicate the experimental tests, it was necessary to use the exact load history applied and not the one that was intended. This difference exists due to the challenging handling of the load cell. Even though the easiest way would be to directly apply the displacement measured during the

experimental test, this was not possible due to numerical reasons. This measurement in such long tests creates extensive lists of values, on average around 3500 values making it difficult for the solver to converge.

Figure 4.10 shows an example of one of the applied load cases, from test 2 (code: 02-R_S235_S355_E). Although the aim was to perform a cyclic load from the ECCS standards (Figure 4.11), there were some differences due to the difficulty of controlling the displacement inf the load cell in real-time.
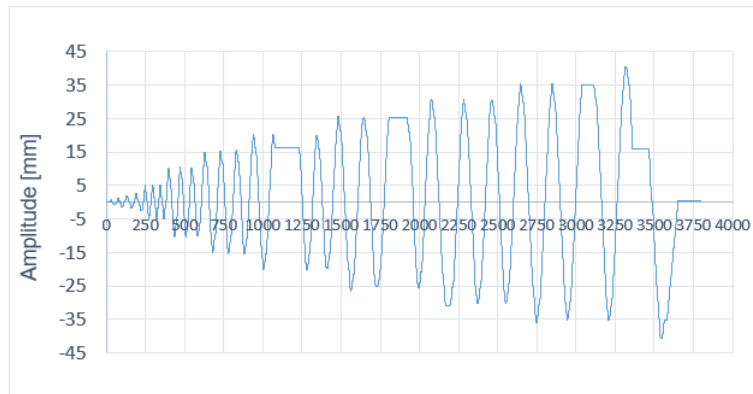
Figure 4.10 - Recorded displacement of the load cell in test number 2 (02-R_S235_S355_E).
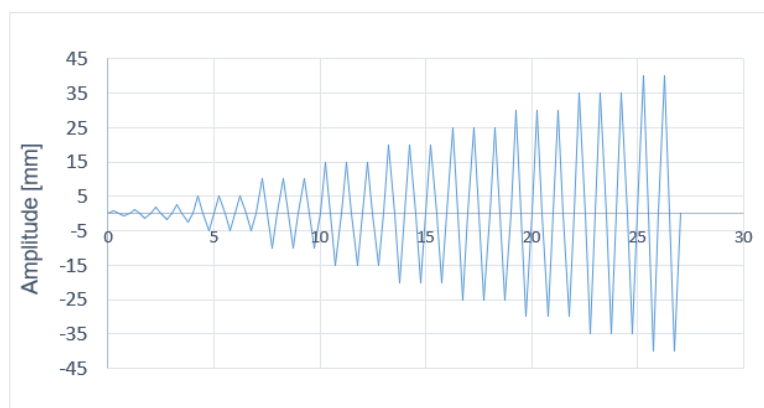
Figure 4.11 - Representation of the cyclic load with ECCS standards.

By comparing both figures there are two main differences. The first one is in the horizontal axis, it is possible to observe that there were several stops during the test. These do not interfere with the simulation itself, because it is not considering time-dependent effects. The second is the slight difference in the maximum displacement reached in each cycle. So, to be true to the tests performed, for every load case, a shorter array of values was created. With a linear development and with the maximum forces achieved in each respective cycle. These were calculated so that each complete cycle would correspond to one step in the software.

The displacement applied to the mobile base plate was implemented as 1 mm and the array was inserted as the amplitude of this force. So, for a different load case, the only parameters to change is this amplitude. Each load history has one or two additional cycles comparing to the real number of

cycles applied in the experimental test, for better understanding the model's behaviour. All amplitude arrays obtained for the several numerical tests performed are available in Annex C – Figures C.1-C.4. Each cycle has four notorious positions: X.0 is the start of the cycle; X.25 is where the maximum displacement is applied in one direction; X.5 when it returns to the initial position; X.75 the maximum displacement to the other direction.

4.6.3 Contact parameters

The type of contact used in these simulations was the *surface-to-surface contact (standard)*, which defines individually the interactions between each pair of elements. This type of formulation, in problems with large displacements such as the one being studied, is numerically more stable than other available formulations. But this advantage has a practical disadvantage: all zones that might have contact need to be identified, and, with several surfaces in each element, there was a long list of pairs that needed to be identified separately. Therefore, for all surfaces from the Internal and External Plate Detail, a contact was created for each of the three surfaces of the pin, where contact might happen. To define which surface was designated as slave or master, only the mesh density was taken into account [28], and the surface with the coarser mesh should be the master of the pair formulation.

The sliding formulation used was a finite sliding that, although heavier, was necessary because the small sliding could not achieve accurate results, due to the large relative displacement between the plates and the pin. Using this formulation the pin would not be able to properly deform, and the tangential motion would be somewhat restricted. A key factor in the success of this model was the usage of tangential behaviour, with the formulation called Penalty. This enables the implementation of isotropic friction in the contacts, which follows the Coulomb law. The value of the friction coefficient had to be explored because the standard value for steel-to-steel contact (0.4), would not get accurate results. This study is presented in section 6.1.

Regarding pressure-overclosure, several methods can be used to define the normal behaviour between the pin surfaces with the plate details surfaces. The most common is to use a linear pressure-overclosure relationship, that allows controlling the penetration through a contact stiffness, the higher this value is, the less penetration happens with the same pressure. This was used in the first simulations, but it did not lead to acceptable results because even with high contact stiffness values, the contact formulation was mitigating deformations and lowering the overall stiffness of the device. As a result, the hard contact enforcement method was applied. This method only allows the minimum penetration possible to avoid divergence errors, so it was more suitable to describe the contact relationship and avoiding unwanted effects.

4.7 Damage criteria

An important part of this dissertation is to assess the possibility to predict failure on the tested devices. To predict in which cycle a DRD1 would break, regardless of geometry and material, this particular study

was conducted in two different specimens: in the tensile test and the devices, after all other variables were already calibrated. This means that upon the simulations reach a satisfactory approximation to their respective experimental tests, the damage parameters were studied so that each simulation would have an end. Otherwise, both numerical models would run indefinitely.

Only two types of damage were thought possible to apply in this project and achieve good results, mainly because most tools offered by *Abaqus* are for the Explicit solver, and the Implicit solver is being used. The first one is called *Maxpe Damage* and the second one *Ductile Damage*. Even though they are very different, both work with the same two steps. Firstly, a damage initiation is defined, so that when that criterion is filled the correspondent element will start degrading. This degradation is the second step, called damage evolution, and it defines the behaviour of the element throughout the degradation phase. It can be defined using the dissipated energy or the displacement that the element can withstand until failure. In the DRD1 these Damage criteria were only applied to the pin.

The first type of damage (*Maxpe*), uses the maximum principal strain as the damage initiation criteria. This sort of damage is based on traction separation law, so when an element breaks it is divided in two and initiates a "crack" which will continue to open until total failure. For implementation, besides defining the characteristics of the criteria and applying it to the desired object (in this case the pin), it is also necessary to define the crack. This technique uses the extended finite element method, designated as XFEM, to solve the calculations regarding the evolution of the crack. Although most authors define the position of the crack through a two-dimensional object that represents its opening location, this definition was not relevant for the present work, because we do not know exactly where this would happen in the DRD1. Thus, this was defined by the damage initiation process, so it would open the cracks in elements with the highest principal strain values.

The second type of damage, the *Ductile Damage*, corresponds to the occurrence of void coalescence in the material, ultimately leading to failure. The initiation parameter is called Fracture Strain (PEEQ) and it is a variable that represents the scalar measure of all components of the equivalent plastic strain, in other words, the total sum of the plastic deformations that an element withstands. This value was studied regardless of stress triaxiality and strain rate, due to the lack of the necessary tests. To sum up, this method initiates damage on elements that cannot withstand a certain magnitude of equivalent plastic strains. Then, the elements are controlled by the damage evolution criteria.

Regardless of the type of damage used, the method to assess if the failure definition is adequate is the following: first, the method was studied on controlled and fast numerical tests, the tensile tests. Using these, the identification of the outcomes of each parameter was accomplished and it was also assessed the best way to implement the damage criteria in study. In this study, the simulations used a mesh of 1mm to enhance the accuracy of the results. Then, these definitions were transferred to the DRD1 to study its behaviour on a global level. It was important to maintain the focus on developing a criterion that could predict failure for every device. So, for specimens with the same pin material, they should break near the cycle that their correspondent experimental test did. This was one of the main factors in the evaluating of the best damage approximation.

5 Material Calibration

Based on the experimental results from the tensile tests for each of the three materials of interest for this project, a calibration was performed using the method described in the previous chapter. To simplify the development of this study, this will be divided into two: first, the plasticity of the material will be analysed and then, the failure method will be explored.

Prior to exploring each material, some parameters were defined as common for all tests. First, the Poisson constant was fixed at 0.3, a common value in the literature, when studying steels. Secondly, Young's modulus was also fixed, based on prior knowledge to 210GPa. Finally, it was acknowledged that, having four different variables (C_1, γ_1, Q_∞, b) to define the plastic evolution of the material, was too unreliable. Therefore, after simulating material definitions on several tensile tests and DRD1's, the isotropic part of the combined hardening (Q_∞, b) was neglected without a significant loss of accuracy. This means that the sub-option *cyclic hardening* of the *combined hardening* can be ignored. Therefore, the plasticity can be defined only by two variables: C_1 and γ_1. As a result, the hardening definition used was non-linear kinematic hardening.

Regarding the study of failure, both the *Maxpe* and the ductile damage were explored, to easily assess which would be the best type of failure to implement in the DRD1.

5.1 Plastic definition

This chapter study is divided in three parts, one for each type of material examined. On the 1EP355 test, all the progression from the tensile test will be presented and explained. For the other two tests, 13PIN235 and 15PIN235, only the best results are shown.

5.1.1 Calibration of the plate material (test 1EP355)

As a first approach, a tensile test was simulated on *Abaqus* with the plasticity based on the engineering curve from the experimental test. Finding the best fitting plasticity in the experimental test was not simple, because the plastic curve implemented can only have a logarithmic evolution. Therefore, all implementations will be based on an approximation. The values used for this first simulation were $C_1 = 3000$, $\gamma_1 = 28$ with a yield stress (f_y) of 400MPa. In Figure 5.1, a comparison is made between the response from the experimental tests with the graphic representation of the values stated before. In order to capture a close stress-strain relationship, three guidelines were taken into account. First, the yield stress was assumed to equal the maximum stress of experimental tensile test (ETT) after the linear range. Then, the Young's modulus value obtained from the ETT is lower than 210 GPa but as already discussed, that was the values used. Lastly, both γ_1 and C_1 where chosen so that its evolution would be asymptotic towards the maximum stress point obtained from the ETT.
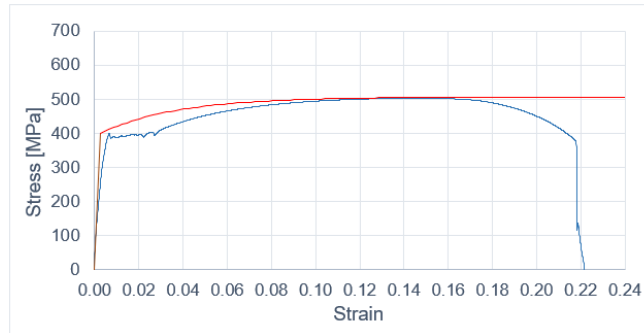
Figure 5.1 - The first material model applied to test 1EP355 (red) and the engineering curve (blue) of this ETT.

As part of the method described in the previous chapter, the simulation was solved using the stress-strain relationship shown in Figure 5.1. From the reaction forces (Z direction) of the fixed surface of the numerical specimen and the displacement of the other end, the result force-displacement curve is defined. Then, using the dimensions of this pin, the stress-strain curve can be calculated. On Figure 5.2, the engineering curve from the simulation is compared with the one from ETT. The discrepancy of values is clear in the numerical test as soon as the necking effect starts, the pin loses most of its resistance and the stress decreases. This behaviour is associated with this localized effect because the material was defined as a horizontal line beyond the start of necking (Figure 5.1). Consequently, the elements present in the necking zone (

Figure 5.3) suffer displacement with no added stress when they reach this horizontal behaviour.
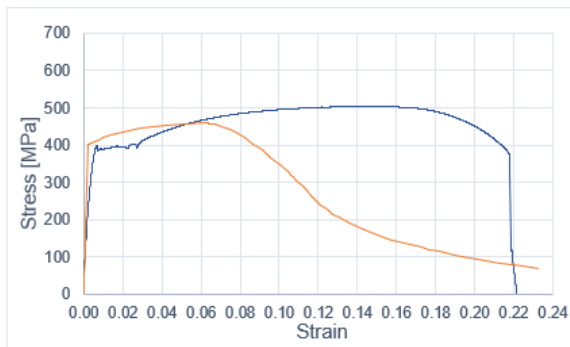
Figure 5.2 - Numerical response of the first material model (orange) compared with the engineering curve (blue).
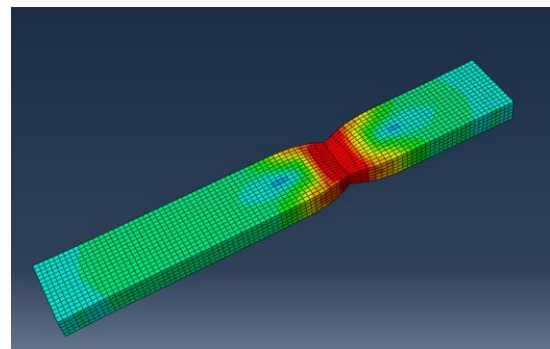
Figure 5.3 - Numerical tensile test with the first material model applied to 1EP355.

As discussed, the engineering curve does not define the true stress-strain relationship of a certain material, Instead of defining it through the engineering curve of the ETT, the logarithmic law was applied to it, following equations (2.2) and (2.3). With those equations, a new curve (True Curve test 1EP355, Figure 5.4) was defined and, as a result, another set of parameters was calculated. Using the same three guidelines, the values obtained were $C_1 = 4350$, $\gamma_1 = 23$ and yield stress (f_y) of 400MPa.

Represented in Figure 5.4 is the graphic representation of the constitutive relation used in this second simulation.

Figure 5.4 - The second material model applied to test 1EP355 (red), the engineering curve (blue) and the true curve (green) of this ETT.

From Figure 5.5 some improvement is observed with this different definition. The stress reaches higher values and it can maintain those values until a strain of 0.09, while in the previous simulation, this was only maintained until 0,07. Nevertheless, it is still far from an acceptable solution.
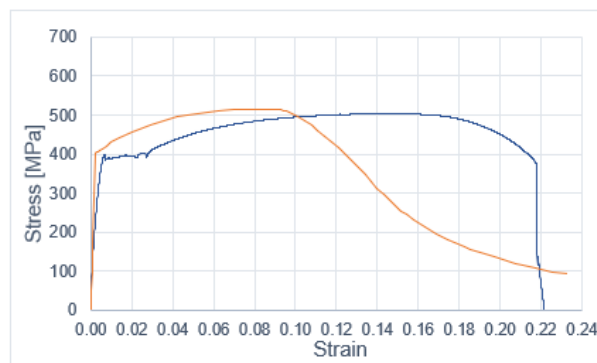
Figure 5.5 - Numerical response of the second material model (orange) compared with engineering curve (blue).

For the third definition, another approach was taken. First, since the typical evolution of a true stress-strain curve has an increase of stress, after the necking phenomenon (Figure 2.13), the plastic variables in study were defined so that higher stresses were reached. Secondly, the logarithmic law applied in the last definition is only accurate until the beginning of the necking effect. Considering the stress-strain curve, this corresponds to the range after the maximum stress. Consequently, the plastic parameters were defined so that the curve that they represent would follow the logarithmic curve until its maximum stress. However, with the limitation of the plastic definition discussed, only close approximations were possible to define. After several simulations testing different pairs of values, the following values were obtained: $C_1 = 2100$, $\gamma_1 = 7.2$, represented in Figure 5.6. This material definition leads to the subsequent response represented in Figure 5.7. In the end, this type of definition was the one that could better represent the material used as it was able to capture the necking effect and has similar stress-strain values, just before the sudden failure of the ETT.
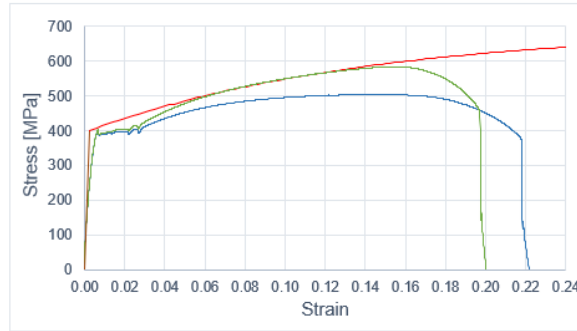
Figure 5.6 - The third material model applied to test 1EP355 (red), the engineering curve
(blue) and the true curve (green) of this ETT.
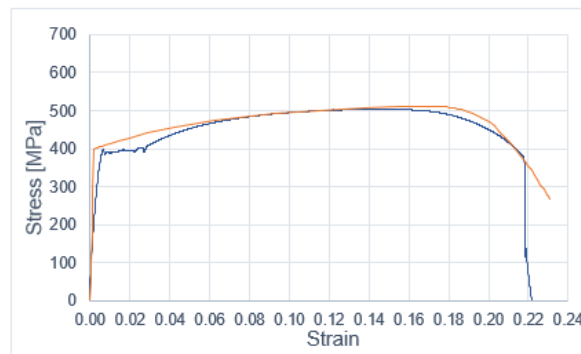
Figure 5.7 - Numerical response of the third material model (orange) compared with
engineering curve (blue).

5.1.2 Results for the SOFMAN material (test 13PIN235)

With the material defined for the plate material, the other tests were studied with the same procedure. After several simulations, the material was calibrated to the following plastic values $C_1 = 1600$, $\gamma_1 = 11$ (Figure 5.8). In Figure 5.9 the behaviour of the numerical test using this definition is presented.
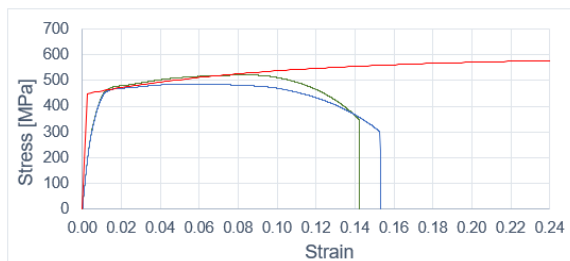
Figure 5.8 - The third material model applied to test 13PIN235 (red), the engineering curve (blue) and the true curve (green) of this ETT.
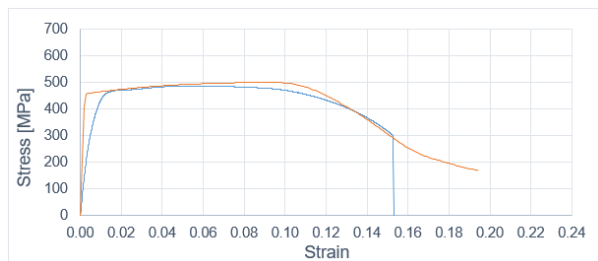
Figure 5.9 - Numerical response of 13PIN235 with material defined (orange) compared with the respective engineering curve (blue).

5.1.3 Results for the IST material (test 15PIN235)

The same procedure was applied to this material leading to the following plastic values; $C_1 = 1500$, $\gamma_1 = 10$. The implemented definition and its result on the tensile numerical test are displayed in Figure 5.10 and Figure 5.11, respectively.
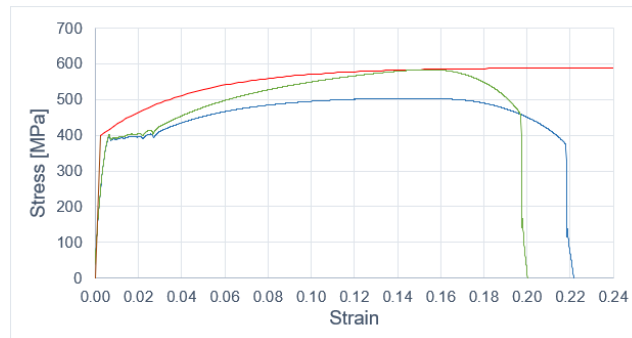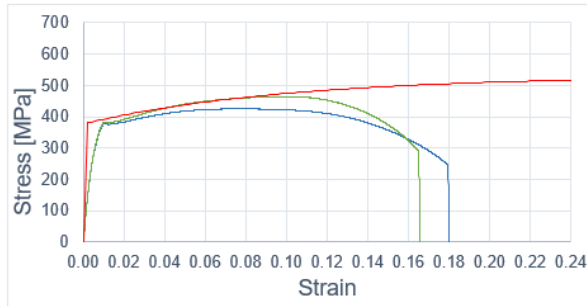
Figure 5.10 - The third material model applied to test 15PIN235 (orange), the engineering curve (blue) and the true curve (green) of this ETT.
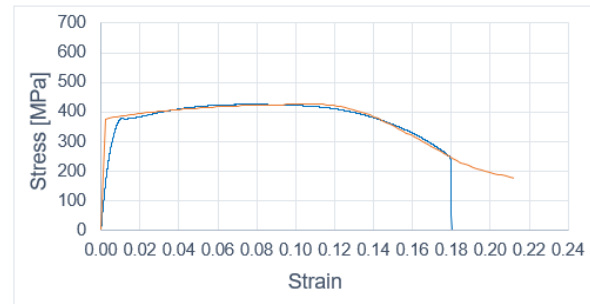
Figure 5.11 - Numerical response of 15PIN235 with material defined (orange) compared with the respective engineering curve (blue).

Table 5.1 - Plastic definition of the materials lists all the material parameters used for each type of material, following the third and most accurate definition. These were the values implemented when defining the material behaviour in the numerical models of a DRD1.

Table 5.1 - Plastic definition of the materials.

Physical properties	Yield Stress [f_y]	Kinematic hard parameter [C_1]	Gamma 1 [γ_1]
Plate Material	400	2100	7.2
IST Pin	380	1500	10
SOFMAN Pin	460	1600	11

5.2 Damage criteria

Upon successfully studying the plastic behaviour of a tensile test, it was necessary to determine a failure definition. As a tool, the test 15PIN235 was used to achieve this goal, moreover, this material that will indeed suffer failure on the devices.

5.2.1 *Ductile damage* criteria

Regarding the Ductile damage modelling, two options were analysed: either using an early damage initiation (DI) and control the necking effect through a tabular displacement evolution; or using the DI initiation just to simulate the sudden and brittle final curve segment, for which the damage evolution (DE) was settled to a value small enough so that it would be a sudden effect.

This first type follows closely the proposal in Figure 2.14. As discussed in chapter 2.3.2.3, matrix D is defined to represent the degradation progress of a numerical element. This matrix is applied when the material enters the necking range so it was calculated so that it follows the necking evolution until failure. Figure 5.12 is the representation of the matrix used to simulate necking on the IST pin. This matrix follows the behaviour after necking of the engineering curve of IST material, increasing the loss of rigidity, from 0 (no damage) to 1 (total failure of the element). The results are presented in Figure 5.13. Note that the curve from the simulation with failure did not go down to zero stress. This is due to the difficulty that the solver has when calculating damage progression with element removal, a consequences of choosing the implicit solver.
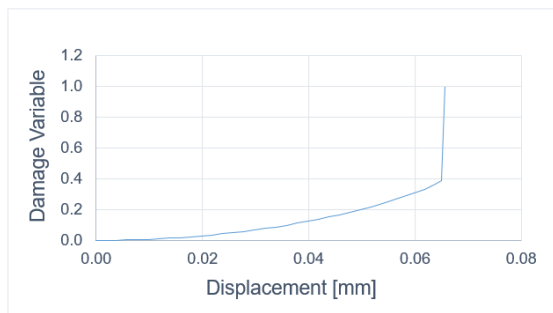
Figure 5.12 - The curve representing the loss of stiffness per displacement of a numerical element.
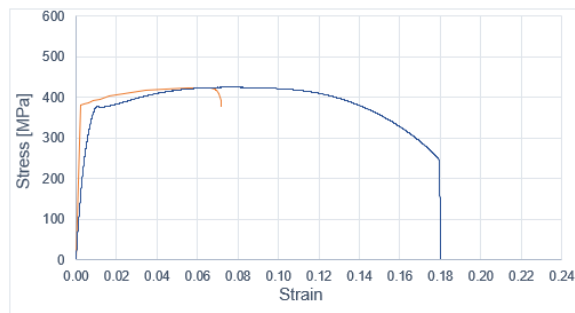
Figure 5.13 - Stress-strain curve using the first application of ductile damage (orange) and the experimental engineering curve of 15PIN235 (blue).

Even though only one result is presented, this type of damage can be acknowledged as not suitable for our objective for the following reason. The development of failure does not follow what was expected, although it was designed for that purpose: it has a much shorter range than the necking from the ETT. Regardless of this, it was still possible to calibrate both the DI and DE so that the outcome would be similar to the ETT. However, for this to happen, the plastic definition would have to change as well, forcing it to stray away from the results of the experimental test. In the end, for this method to work, the numerous parameters of both plasticity and failure would need to be calibrated individually, for each type of material. This defeats the purpose of having a method that could be general and easy to apply to different ETT or even DRD1. Besides, this solver has difficulties calculating iterations when damage is involved, which in this case, starts at the beginning of the necking. It was concluded that using this damage definition to simulate the necking effect would not be a solution for this project.

Considering the problems presented before, it was necessary to develop a definition that would not rely on damage evolution. The solution was to use a failure definition that would end the simulation at the correct moment, without DE. As a result, this method cannot be perceived as a damage criterion because it will only predict when failure would occur.

Without DE, the only parameter necessary to define damage is the Fracture Strain(PEEQ). Using a PEEQ=0.98 the curve that was obtained from the numerical tensile test is represented in Figure 5.14.

As it is possible to observe, the numerical curve has a loss of stress near $\varepsilon = 0.18$, which is the same as the correspondent ETT. The reason why the stresses in the numerical curve does not fall until 0 is again due to the difficulty in calculating the damage evolution (this consists in removing elements when they lose all their stiffness, Figure 5.15). The first advantage of this method is that we know that from the last point of the numerical curve it would only go straight to null stress. The second is the ability to predict failure without simulating the damage. This is possible because the variable PEEQ can be observed throughout a simulation, so that, knowing when the pin breaks, we can obtain the exact value of PEEQ at that moment. Although this is a simplification, this method is straight forward and therefore can be used to find a universal calibration value to predict the cycle of failure in each DRD1.
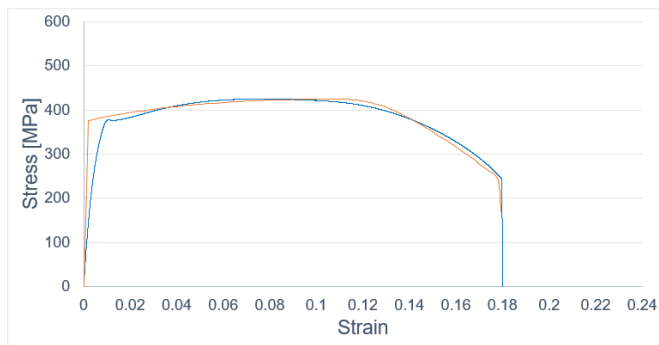
Figure 5.14 - Stress-strain curve using the second application of ductile damage (orange), the experimental engineering curve of 15PIN235 (blue).
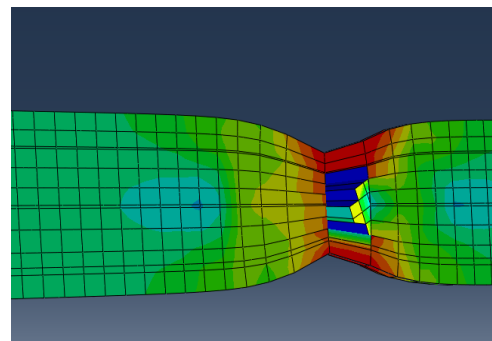
Figure 5.15 - Detail of the necking effect and correspondent element removal due to damage.

5.2.2 *Maxpe* criteria

This method has two phases: the DI defined by the maximum principal strain, represented with the appearance of a crack, and the DE that defines how much does the material resists to the progression of the crack. Several attempts were performed to define the necessary parameters: in the DI the maximum principal strain, in the DE it was necessary to define a type of degradation and the fracture energy (energy released before the crack propagates to another numerical element). As shown in Figure 5.16, this method looks promising because it can perform the degradation of the material without being aborted by the solver. Two main results were achieved: one that uses a linear degradation and one that uses an exponential one (Figure 5.17). They both have the same initiation parameter with a Max. Principal strain equal to 0.17 when in fact it should be a lower value, around 0.1 (when the necking effect starts). This was not possible because of the nature of the test, on this tensile test several cracks would appear throughout the specimen. It was not perceived as a problem because in the DRD1 the Pin is subjected to bending, localizing the place that a crack can appear. Comparing the two damage formulations in this test, the exponential definition has a better behaviour.
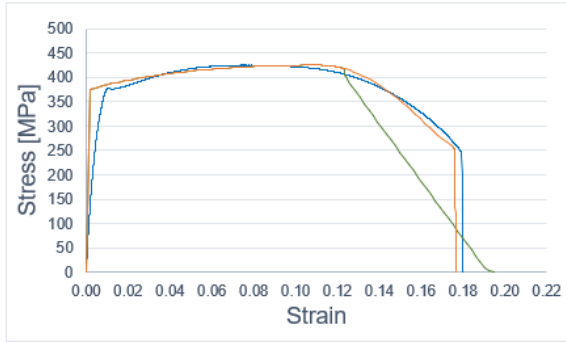
Figure 5.16 - Stress-strain curve with exponential degradation (orange), with linear degradation (green) and the experimental engineering curve of 15PIN235 (blue).
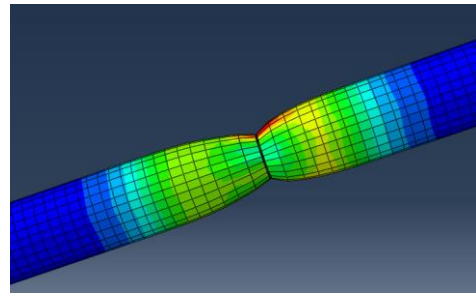
Figure 5.17 - Detail of Necking and opening of the crack, in the exponential definition.

Although it is difficult to calibrate this definition due to the extensive combination of possible values, this method is the most promising when studying DRD1. Besides being capable of introducing degradation on the material, the implicit solver can calculate the damage evolution without the solver terminating in errors.

6 Device Simulation Results

This chapter will have five sections. Firstly, an initial calibration was performed to understand the effects that some parameters have on the device. Secondly, the calibrated model developed in this dissertation will be applied to several DISSIPABLE devices and compared in detail with the correspondent experimental test. Thirdly, two damage formulations were added to the material definition and it was studied the effectiveness of these damage criteria. Then, The developed model will be validated with other experimental tests, from this project and project INERD. In the end, a parametric study was conducted having in mind the untested devices.

6.1 Calibration

The visualization of the influence of several parameters has two objectives. The main one is to define specific values for the variables that were still not defined, namely the friction coefficient and the gap between the plate details and the pin. The other objective is to understand the tools that can be used to improve a model, to facilitate future studies that might be performed on this topic. This will be performed by comparing the hysteretic curves between simulations that have different values for certain variables.

6.1.1 Gap value and friction coefficient

Using the second device (code: 02-R_S235_S355_E), a set of tests were performed with only one variable being studied at a time, first the size of the gap between plate details and the pin and secondly the friction coefficient on their contact definition. Represented in Figure 6.1 the force-displacement curves are displayed.
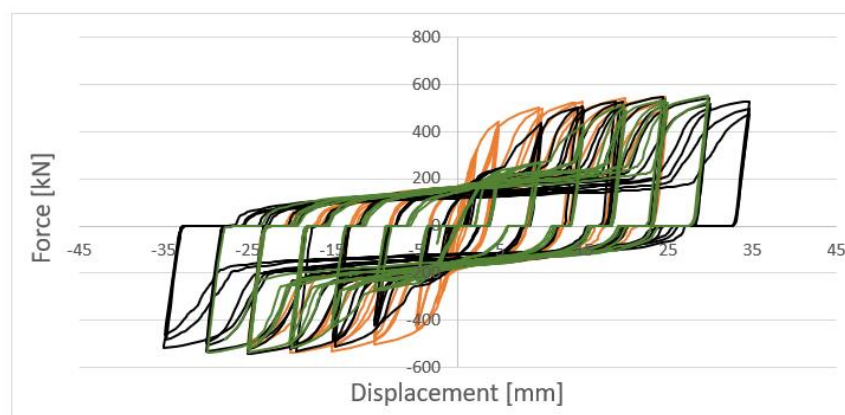
Figure 6.1 - Hysteretic curves of simulations with different gaps: 0.1mm (orange); 0.5mm (black); 1mm(green).

As shown, the DRD1 models are very sensitive to this variable being the most obvious effect, the evolution of the maximum forces achieved in each cycle. As the gap gets smaller, the contact between the elements in question happens earlier, making the device enter in the plastic range. This variable does not interfere with the ultimate force, they all converge to the same value. This evolution cannot be

used to assess the measurement in question because it is also a phenomenon dependent on the friction coefficient. There is a behaviour that is characteristic only of the gap value, the first moment in which the pin enters in the plastic range. This event reflects a sudden gain of stiffness at a specific moment during loading, before this, the pin has an elastic behaviour. For an easier observation, Figure 6.2 represents an enlargement of the previous graph as well as the hysteretic curves from the respective experimental test. The value calibrated for this variable was 0.75mm.
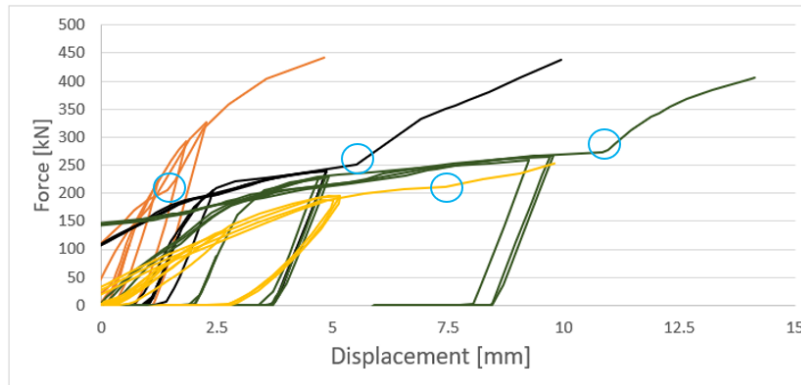
Figure 6.2 - Identification of the sudden gain of stiffness on experimental test (yellow) and models with different gaps: 0.1mm (orange); 0.5mm (black); 1mm(green).

When testing different friction coefficients (Figure 6.3), it is clear that it only affects the evolution of maximum forces. And, not like the previous variable, the moment of the first plastic deformations does not change. Upon determining the gap values, the friction coefficient could be calibrated because it is the last parameter that has this type of influence. After assessing different DRD simulation this value was established as 0.05.
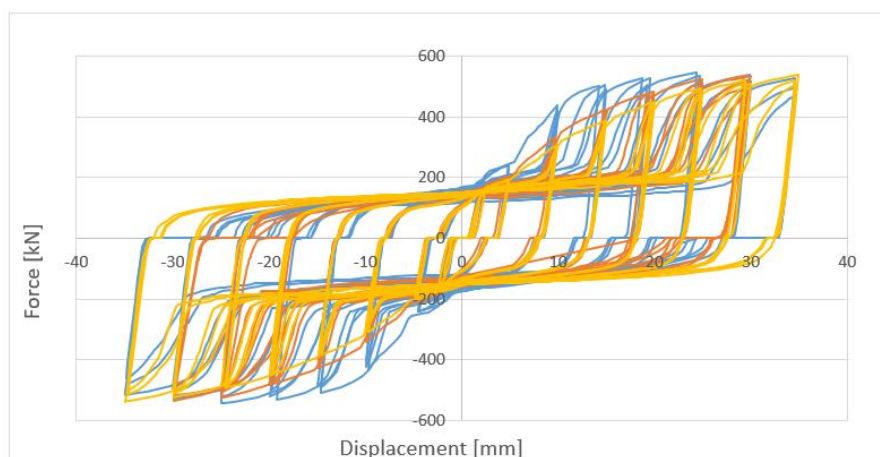
Figure 6.3 - Hysteretic curves of simulations with different friction coeficients: 0.4 (blue); 0.1 (orange); 0.01 (yellow).

6.1.2 Yield stress value

To understand the influence that the yield stress value of the Pin material had on these devices, test number 2 (code: 02-R_S235_S355_E) was used for this study. However, this is not a parameter that needs to be calibrated, it should be used the same value as the yield stress from the respective tensile test. But, in case the steel grade is unknown, this application might be needed. These simulations were performed only until the first cycle of 25mm because is around this displacement the maximum force stabilizes for this device.

As shown in Figure 6.4, there is a significant impact on overall behaviour. The first consequence is the ultimate force achieved and the second is the low-pressure contact value (dashed lines on Figure 6.4). With higher pin steel-grades, these two values are higher as well.

This study was also applied to the plate elements and the influence was minimal mainly due to the low deformations on these elements throughout the test. This was more relevant on devices with no spacers between plates such as the ones from the INERD project, where lateral deformation was observed in the external plates.
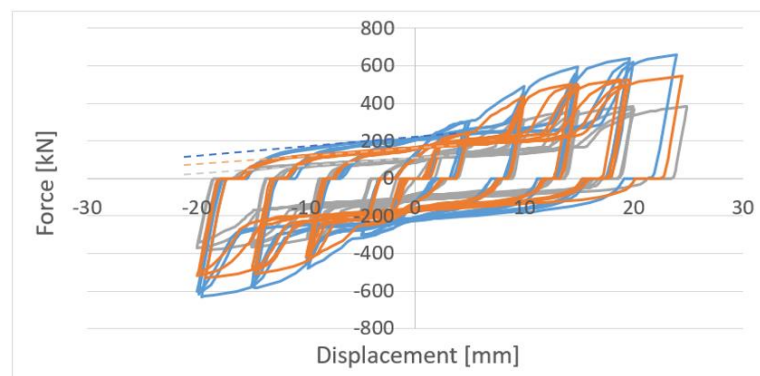
Figure 6.4 - Hysteretic curves of simulations with different yield stress: 500Mpa (blue); 380 Mpa (orange); 235 Mpa (grey) and respective force level of low-pressure contact (dashed).

6.2 Model developed with Dissipable devices

In this study, several numerical models were explored and one of those was selected as the one that achieved better approximations to the real behaviour. That model was defined throughout the previous chapters.

The model chosen has one variant: the mesh density of both the pin and the details parts, leading to two versions of this model, version A and version B. This was developed from the necessity of understanding the effect that changing the mesh of the pin had. In Table 6.1 the specifications of each version are summarized. Keep in mind that in version B the surfaces of the pin were designate as *master* and in version A it was designated as *slave,* entirely due to their mesh size relation.

Table 6.1 - specifications of each model, including the total number of nodes.

Approximate global mesh size	Plate detail parts	Pin part	Number of elements/ Number of nodes
Version A	6 mm	4 mm	12940 / 18718
Version B	5 mm	6 mm	9628 / 15082

6.2.1 Device number 2

This box was the specimen used in most of the development of the model. It is composed by the IST pin material (test 15PIN235) and the rest of the box by the plate material(test 1EP355). It was subjected to the cyclic load of Annex C – Figures C.2, that follows the ECCS load standards. It is worth to notice that, for now, only the hysteric curves are being evaluated. Therefore, the damage criterion was not applied in this chapter.

As shown in Figure 6.5 the solution created (version A) has similar curves as the experimental ones. From these hysteretic curves, the maximum forces in each cycle are very close which is a good indicator that the gap value and the friction value were well assessed. Also, the material calibration seems accurate due to the close ultimate force value reached towards the end of the test.

One of the behaviours that were not possible to capture was the loss of stiffness on the unloading path. Until half the unloading range of each cycle, the numerical model is accurate (their inclination is the same) but closer to the horizontal axis the experimental curve changes the inclination while the numerical model maintains it. The other difference was the location in the Pin that accumulated most of the deformations (Figure 6.6). In this image, the colour scale refers to the plastic strain of each element to facilitate the interpretation of the deformations. While in the experimental test the deformations accumulated in the centre of the pin, in the numerical, it was in the contact locations with internal plates.

Figure 6.5 - Left: comparison of hysteretic curves between experimental test (blue) and numerical model version A (red). Right: Pin and Lateral Plate detail of version A mesh.
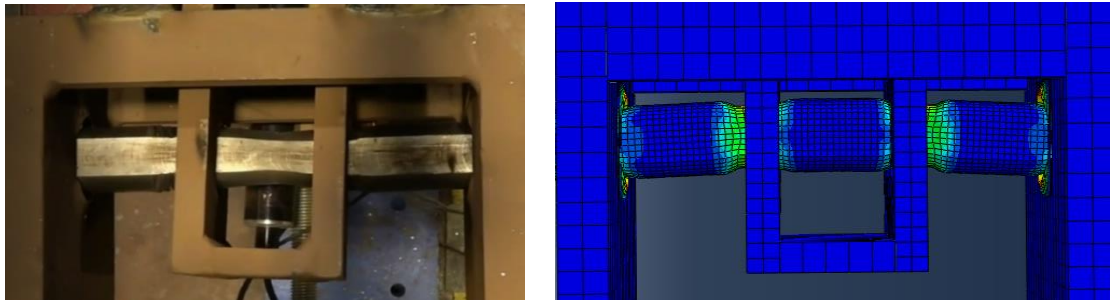
Figure 6.6 - Pin deformation close to failure in the experimental test (left) and the numerical test (right) at step 26.5.

The low contact pressure zone also has similar force values, this is the horizontal range found in every cycle before the device reaches higher stiffness, that has a value of around 180 kN. It is associated with the contact of the 6 points represented in Figure 6.8 (left), that leads to the plastic deformation of both pin and plate. The set of figures (Figure 6.7 and Figure 6.8) represents the top half view of the model throughout half a cycle, from a displacement of 25,3mm (step 18.25) to -25.5mm (step 18.75). This cycle was chosen as an example to demonstrate this effect and their colour scale is in figure Figure 6.9. Notice that the beginning of this behaviour in each cycle is progressively later than the previous cycle (Figure 6.5), due to the increasing deformation that the box withstands, particularly on the plate holes. With larger deformations, larger displacements are required for these points to enter in contact. When the box reaches the step 18,75 the 6 points can be distinguished for their high von mises stresses values, because these are the plate locations that absorbs most of the deformations. This effect leads to the ovalization of the holes in the plates (Figure 6.10).
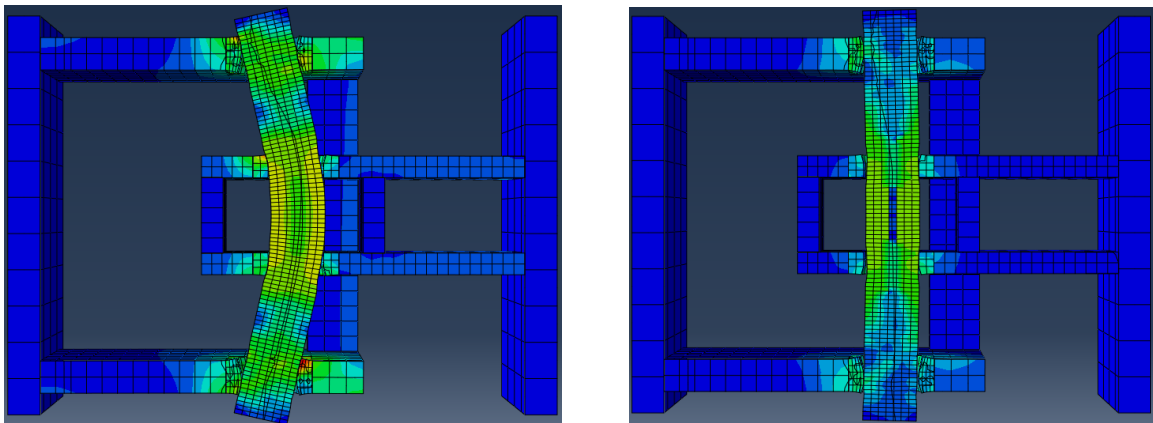
Figure 6.7 - Top view of the model in step 18.25, the beginning of this half-cycle(left) and Top view of the model in step 18.50, when the model has displacement equal to zero in this cycle (right).
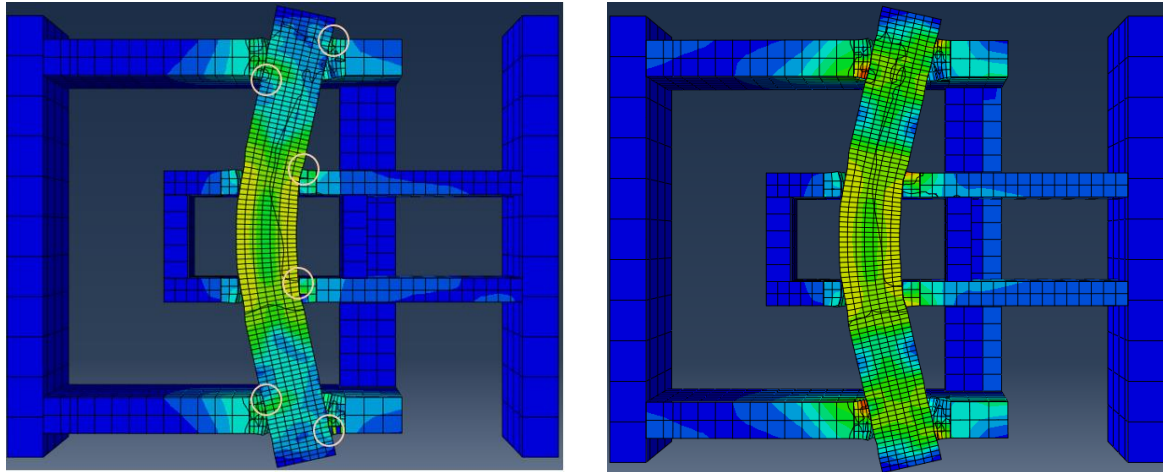
Figure 6.8 - Top view of the model in step 18.73, when the six points enter in contact and stiffness rises (left) and Top view of the model in step 18.75, the end of this half-cycle (right).
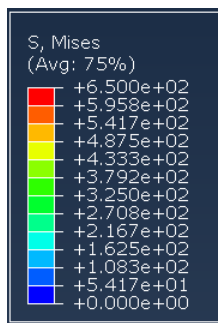
Figure 6.9 - The colour scale of Von Mises stress of Figures A, B, C, D.
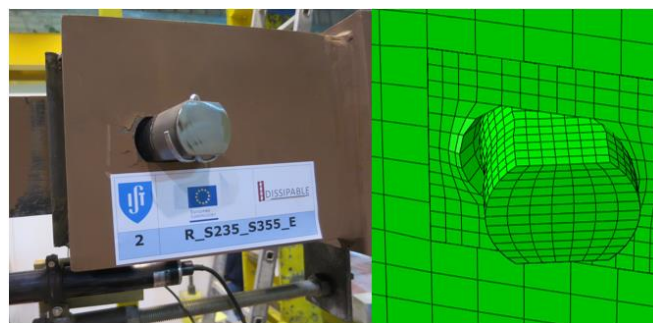
Figure 6.10 - Ovalization in similar situations of Experimental test (left) and numerical test (right).

Version A of this model can simulate quite well the behaviour of the correspondent test but due to its meshing properties, this simulation took close to 34 hours to run. To develop a model that could be solved in less time, Version B was created. With a slit change of mesh sizes in the Pin and Plate Detail parts (Figure 6.11 - right), the solver could perform the calculations in around 6:30 hours. A major improvement but the accuracy should be conserved

Figure 6.11 (left) evidenciates the small differences between numerical models (Version A and B). For an improved evaluation of each model performance, the energy dissipation was calculated, summing the area of each cycle using the trapezoidal method. The initial cycles and the final cycle were not taking into account because at the beginning there is no energy dissipation(elastic behaviour) and at the end, the numerical solutions don´t have a damage criterion. Figure 6.12 represents the energy dissipated in each cycle regarding the three hysteretic curves. Both version A and B follow the same progression throughout the cycles as the experimental test. The dissipated energy of the experimental test (E_E) is compared with the energy from the simulations (E_N) in Table 6.2, using the percentual difference equation (6.1).

$$\%\text{difference} = \frac{|E_E - E_N|}{\left|\frac{(E_E + E_N)}{2}\right|} \times 100 \qquad (6.1)$$
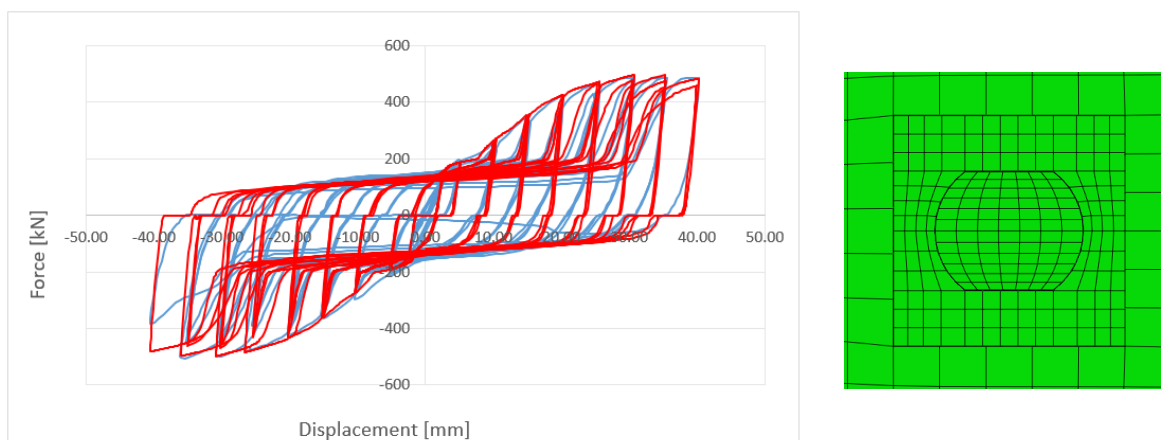

Figure 6.11 - Left: Comparison of hysteretic curves between experimental test (blue) and numerical model version A (red) and B (black). Right: Pin and Lateral Plate detail of version B mesh.
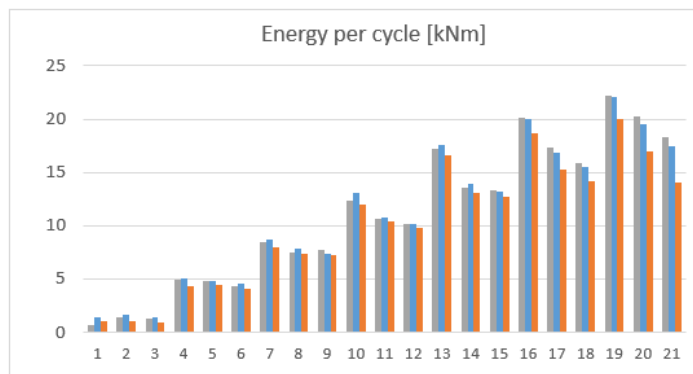

Figure 6.12 - Energy dissipated of the experimental test (orange), version A (Blue) and version B (grey) in specimen 2.

Table 6.2 - Comparison of energy dissipation between numerical models and experimental test – device number 2.

Specimen 02-R_S235_S355_E	Total energy dissipated (kNm)	Percentual difference (%)
Experimental Test	218.5	
Type A Model	240.5	9.5
Type B Model	241.1	9.8

The numerical model (version A) has achieved an overestimation of 9.5% regarding the real behaviour. Notice how in the last cycles the error is higher, the main reason is the presence of steel degradation on the experimental test. With higher damage effects, the higher is the error in that cycle because this model does not have damage implemented.

Version B, although less accurate, it is still very close to version A meaning that it can be a useful tool to obtain results, similarly to its precedented, but much faster. To prove this hypothesis, the comparison between versions will be performed on the next two specimens: device number 3 and number 4.

The percentual difference without considering the unloading range of each cycle was calculated to understand the error that the unloading range creates (Table 6.3). The different behaviour on the unloading is responsible for around half the error between the real and the numerical tests.

Table 6.3 - Comparison of energy dissipation between numerical models and experimental test, without considering the unloading range of the hysteretic curves – device number 2.

Specimen 02-R_S235_S355_E	Energy dissipated (kNm)	Percentual difference* (%)
Experimental Test	242.0	
Type A Model	252.8	4.3
Type B Model	253.4	4.6

6.2.2 Device number 3

To simulate the device number 3 (code: 03-R_S235_S355_C1) only the applied load history changes (Annex C – Figures C.3), in comparison with the device 2. In Figure 6.13,Figure 6.14Figure 6.15 and Table 6.4 the relevant results are displayed, from simulation using the model version B. The evaluation of this model is similar to the previous device. This indicates that this model is able to achieve acceptable results regardless of the displacements it is subjected.
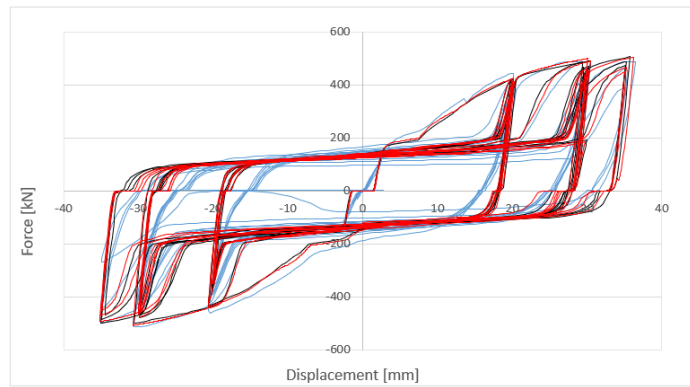
Figure 6.13 - Comparison of hysteretic curves between experimental test (blue) and numerical model version A (red) and B (black) of specimen 3.
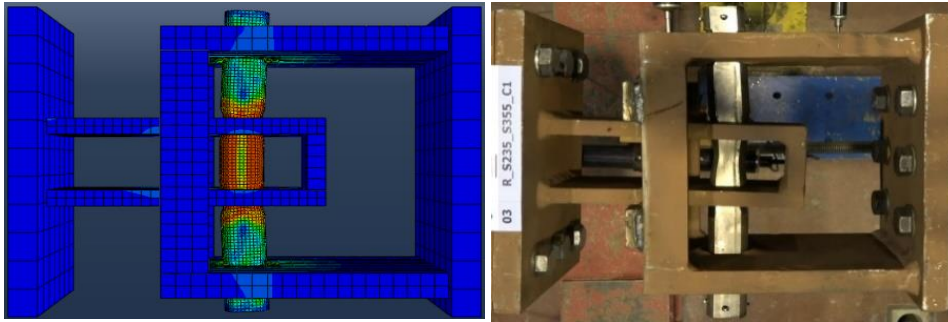
Figure 6.14 - State of the box: right before failure (right), at the end of the simulation (left) with Von Mises stress.

Table 6.4 - Comparison of energy dissipation between numerical models and experimental test, with () and without (*) considering the unloading range of the hysteretic curves – device number 3.

Specimen 03-R_S235_S355_C1	Total Energy dissipated (kNm)	Percentual difference (%)	Percentual difference* (%)
Experimental Test	189.2		
Type A Model	208.6	9.7	3.9
Type B Model	210.5	10.6	4.9
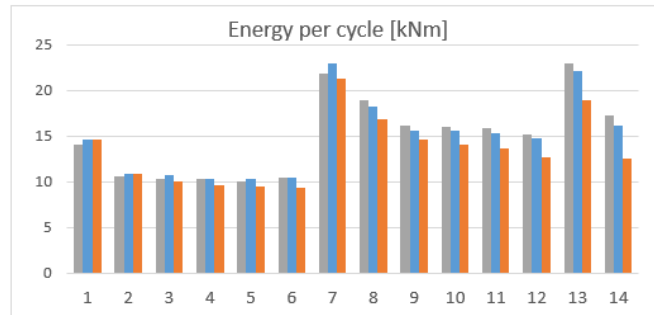
Figure 6.15 - Energy dissipated of the experimental test (orange), version A (Blue) and version B (grey) in specimen 3.

6.2.3 Device number 4

This device had the same properties as the last two but was subjected to another load history (Annex C – Figures C.4). Although this box had a new set of spacers to avoid lateral movement, this addition was not explored in this work. As no instability is implemented in the simulation, there is no lateral displacement (Figure 6.17), removing the use of these new spacers.

As shown in Figure 6.16, the general development of the curves is similar, although the low contact pressure range has more evident differences when compared with the other devices. In this specimen, due to the loads being more constant, there is a bigger consequence of the degradation of the pin that the model does not capture. This degradation is evidential in the descendant values of that horizontal range in the experimental hysteretic curve. This affects the dissipated energy throughout the cycles, as shown in Figure 6.18. The values of the experimental test get lower every cycle while in the numerical model it is almost constant. Ultimately, this reflects in the total energy dissipated reaching an error of 15.6% (Table 6.5), higher than the last two boxes. In other words, in this experimental test, the damage degradation starts earlier and influences more cycles than the other tests. Optimally, when introducing a functioning damage criterion this error would be much smaller.
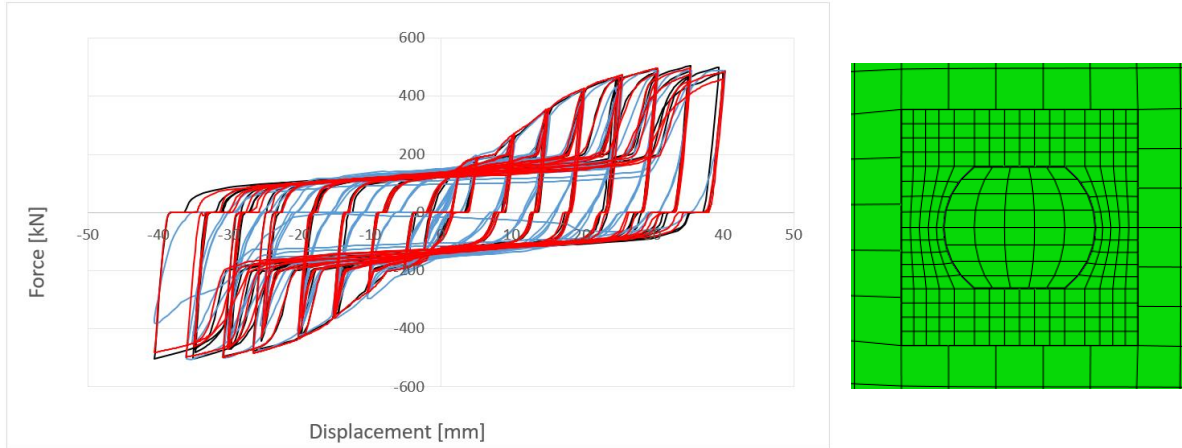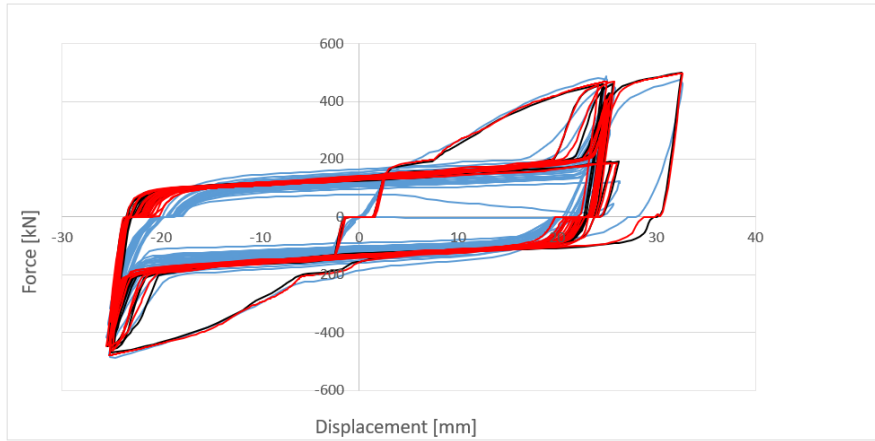
Figure 6.16 - Comparison of hysteretic curves between experimental test (blue) and numerical model version A (red) and B (black) of specimen 4.
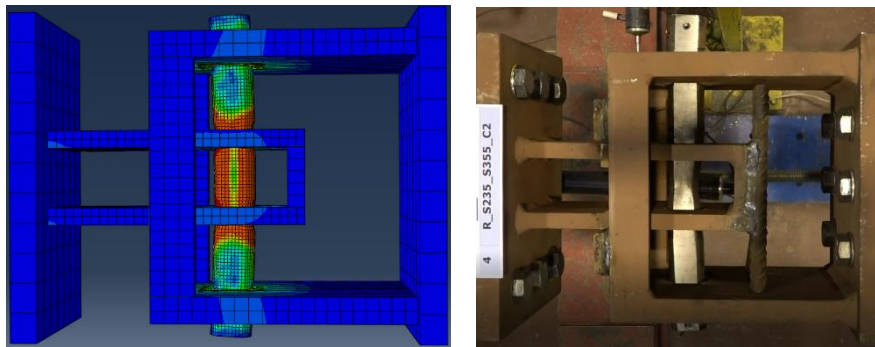
Figure 6.17 - State of the box: right before failure (right), at the end of the simulation (left) with Von Mises stress.

Table 6.5 - Comparison of energy dissipation between numerical models and experimental test, with () and without (*) considering the unloading range of the hysteretic curves – device number 4.

Specimen 04-R_S235_S355_C2	Total Energy dissipated (kNm)	Percentual difference (%)	Percentual difference* (%)
Experimental Test	206.1		
Type A Model	241.2	15.6	10.1
Type B Model	243.0	16.4	11.3
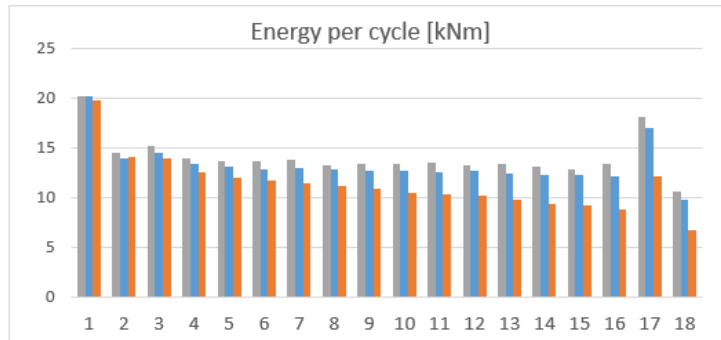
Figure 6.18 - Energy dissipated of the experimental test (orange), version A (Blue) and version B (grey) in specimen 4.

In conclusion, version B of this model has less than 2% of added error comparing to version A. Therefore, the remaining of the studies will be performed using version B, for its solving speed. It is also interesting to notice that the error associated with the inability of predicting the correct unloading path is constant. This error is close to 5% in the three specimens' studies regardless of the numerical version used.

To prove the effectiveness of the plastic definition method (section- 5.1) applied in this project, each box was simulated using the second plastic model on the pin. In other words, model type B was solved with a different plastic formulation adapted to the pin, the second definition instead of the third. Considering the hysteretic curves from specimen number two (Figure 6.19), the impact of using different plastic definitions seems low. Only this figure is presented because the other two specimens had similar curve developments. However, when considering the percentual difference of dissipated energy from each type of plasticity with the experimental test, it is clear that, regardless of the specimen, the second definition has inferior results (Table 6.6). In conclusion, the study performed in section 5.1 enhanced the accuracy in the DRD1 solutions.
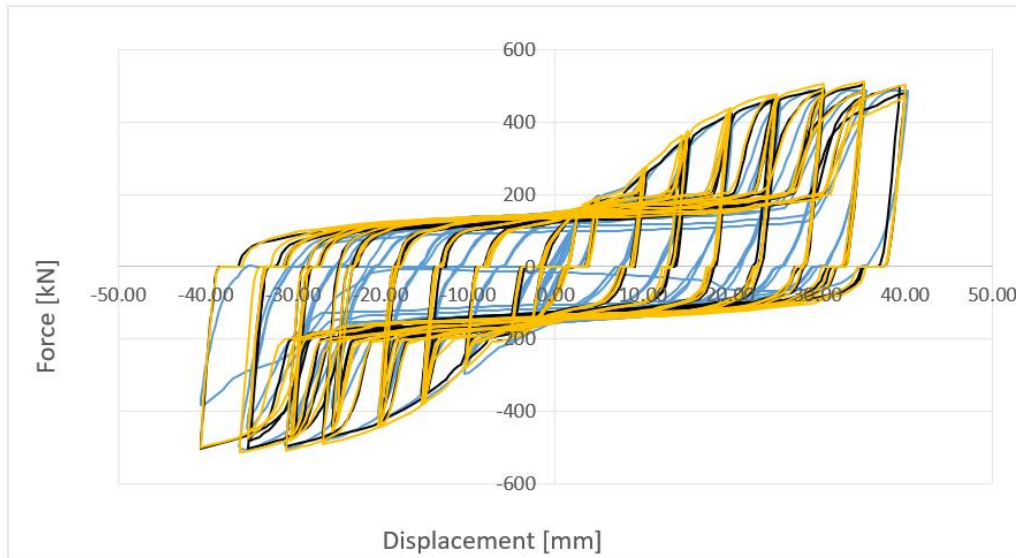
Figure 6.19 - Comparison of hysteretic curves between experimental test (blue) and numerical model version B with the second plastic definition (yellow) and third plastic definition(black) of specimen 2.

Table 6.6 - Energy dissipated and percentual difference of each numerical simulation with its corresponding experimental test, using both the second and the third material definition.

	Box 2 [kNm] | [%]		Box 3 [kNm] | [%]		Box 4 [kNm] | [%]	
Model with the third plastic definition (Energy dissipated | Percentual difference)	241.1	9.8	210.5	10.6	243.0	16.4
Model with the second plastic definition (Energy dissipated | Percentual difference)	256.4	15.9	225.5	17.5	262.2	23.9
Experimental test (Energy dissipated)	218.5		189.2		206.1	

6.3 Damage criteria

Using the information gathered in the study of the damage criteria applied to the numerical tensile tests (section 5.2), the implementation of such criterion, in the DRD1 model, was explored. First, the implementation of the *traction separation law* type of damage was applied and then the *ductile damage* function was used.

6.3.1 Using *Maxpe* as damage criteria

To study this implementation, the model version B of box number 2 (code 02-R_S235_S355_E) was used. The *Maxpe* function was added to the pin material properties and several definitions were studied, changing, in the DI, the maximum principal strain (MPS) value and in the DE the fracture energy and the type of softening (exponential or linear). Although in the tensile tests the exponential softening achieved better results, in the DRD1 simulations, it was the linear softening. The definition that achieved the best results is defined by:

- A MPS = 0.1, which is the strain that, the stress-strain curve of IST material reaches the highest stress value. This value defines the start of material degradation by initiating a crack.
- A linear softening with 1350 as fracture strain, that corresponds to the area of the experimental force-displacement from the strain value of 0.1 to fracture

Figure 6.20 represents the influence that the damage criteria described have on the device. It is possible to identify the material degradation in the last cycles, the maximum force starts to lower and the low contact pressure zone also decreases towards the end. Figure 6.21 shows the total fracture of the pin, in this numerical solution, and Figure 6.22 shows the opening of the fracture when it divides the Pin in two. Besides the successful damage degradation implemented, the end of the test was also simulated accurately. The experimental test failed on step 25.25 and the simulation on step 25.56.
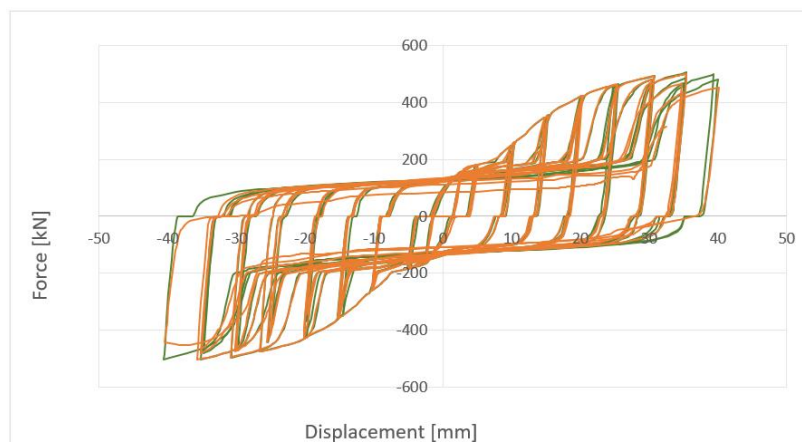
Figure 6.20 - Comparison between the numerical results of device number 2 with (orange) and without the damage implemented (green).
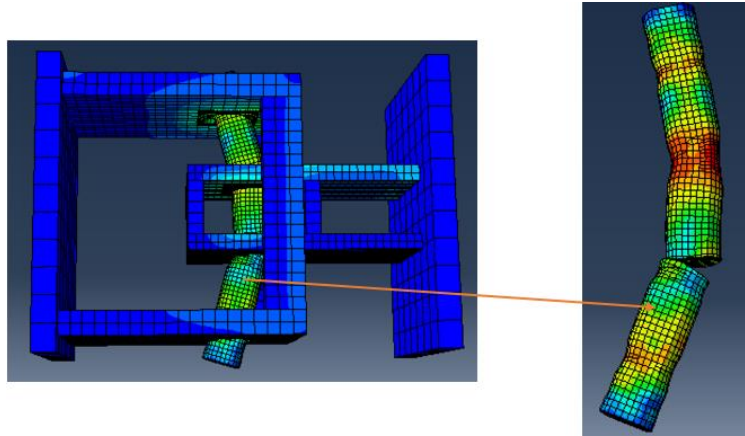
Figure 6.21 - State of the device (left) at the end of the simulation upon total fracture of the pin (right).
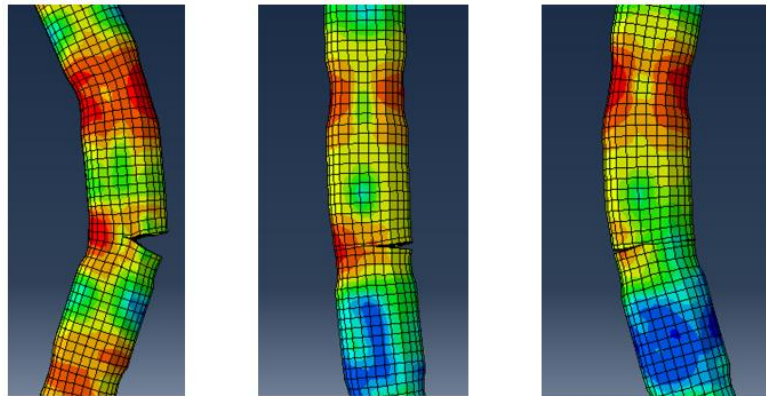
Figure 6.22 - Progression of the crack opening: existing crack at step 25.25 (left); progression of the crack through the pin, at step 25.56 (centre); fracture of the pin in two in step 25.70 (right).

Good results were achieved with this damage criteria but it has a complex definition, which makes the calibration of this criterion difficult to execute. Besides, this definition turned the model much heavier, taking around 20 hours to solve, using version B. As a consequence, another type of failure criteria was explored: the use of the *ductile damage* criteria to predict failure.

6.3.2 Using *ductile damage* to predict failure

As discussed in section 5.2.1 this method does not include a damage criterion in the model because it does not implement degradation in the device, this only predicts the cycle of failure. The maximum value of the equivalent plastic strain (PEEQ) was identified in the numerical solutions in the cycle of

experimental failure. In other words, each experimental test has a failure cycle and, in the numerical models, it was identified the maximum value of PEEQ in that cycle.

In Table 6.7, the cycle of failure for the three experimental tests is identified. In these devices, from the start of a crack until its total propagation always happens in less than a cycle, so it was registered the cycle where the crack got through the pin.

Table 6.7 - Failure cycle of each experimental test.

Devices	02-R_S235_S355_E	03-R_S235_S355_C1	04-R_S235_S355_C2
Failure cycle	25.25	18.75	22.25

The highest value of PEEQ was recorded throughout each numerical test. In Figure 6.23 those values are represented, as well as, the correspondent experimental fracture of each device, in a lighter colour. Shown in Table 6.8, the values of PEEQ in the failure cycle are displayed, which corresponds to the intersection of each curve in Figure 6.23.
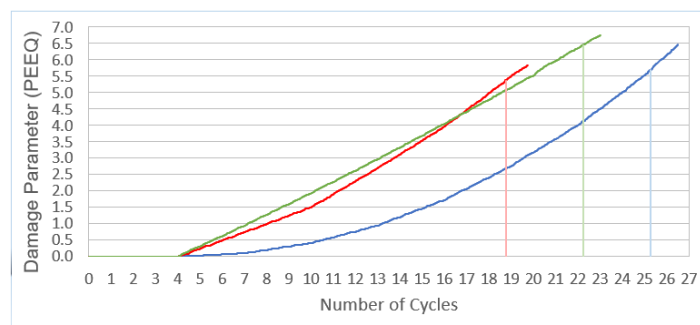
Figure 6.23 - Evolution of the maximum plastic strain accumulation in each simulation, with a vertical line representing the end of the correspondent experimental test; Test2 (blue), test3 (red), test4 (green).

Table 6.8 - Maximum PEEQ value on the simulation at the failure cycle (experimental).

Numerical solutions	Simulation of device 2	Simulation of device 3	Simulation of device 4
Maximum PEEQ at failure (experimental moment)	5.7	5.35	6.45

It is interesting to point out that the evolution of the PEEQ is directly related to the load history applied in each box. For instance, the curve from device 2 has an exponential growth because the load applied is crescent (Annex C – Figures C.2), while the device 4 is almost a straight line due to its constant load history (Annex C – Figures C.4). Another remark is the fact that until cycle 4 they all have an elastic

response due to the low displacements. Finally, considering only these three test subjects, the parameter in the study was calibrated to 5.833, by calculating the average PEEQ value.

Next, to assess the error that this method has associated a horizontal line was implemented on the figure with the calibrated value (Figure 6.24). Doing so, we could observe when the simulation would end using such a definition to end the simulation (Table 6.9). Then, by comparing with the actual cycle of failure, the discrepancy of the cycle was calculated
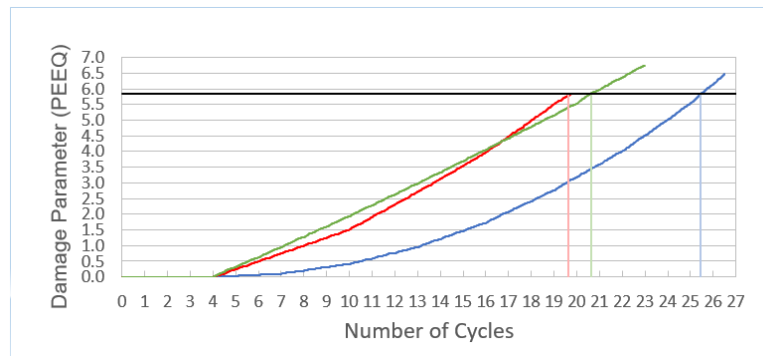
Figure 6.24 - Evolution of the maximum plastic strain accumulation in each simulation, with calibrated PEEQ value and correspondent ending cycle of the simulations: test 2 (blue), test 3 (red) and test 4 (green).

Table 6.9 - Cycle of failure on the simulation using the calibrated value of PEEQ, with the error from the correspondent experimental test.

Numerical solutions	Simulation of device 2	Simulation of device 3	Simulation of device 4
Predicted failure cycle	25.43	19.62	20.65
Difference from numerical and experimental [Cycles]	0.18	0.87	-1.6

Although this methodology does not implement the effects that a damage criterion would, it can give an acceptable estimative on the failure cycle. The maximum error occurred on the fourth device, mainly because it is the device that withstood more material degradation. As a result, not having such effect implemented in the simulation led to a bigger discrepancy.

To understand the limits that this simplification had, it was assessed in the numerical validation. The first limitation already acknowledged is that it only reaches approximate results on mechanisms that have a fast damage degradation. In other words, devices that, from the appearance of a crack to total failure, only achieve less than one or two cycles.

6.4 Validation of the numerical model

To validate this model, devices from the INERD project and device number 1 from DISSIPABLE were used. They were simulated using model type B with the correct geometry and materials from each correspondent test. Regarding the gap value in the INERD devices, it was not possible to find a specific value, so it was used the same from the DISSIPABLE devices. Consequently, some considerable errors were brought by this discrepancy. To assess the accuracy of the simulations, the hysteretic curves were compared and the method to predicts failure assessed. The materials from the INERD devices were calibrated the same way as in Chapter 5, using the ETT available in the report from the project [26]. The parameters calculated and implemented are displayed in Table 6.10.

Table 6.10 - Plastic definition calibrated from the ETT from INERD.

Physical properties	Yield Stress $[f_y]$	Kinematic hard parameter $[C_1]$	Gamma 1 $[\gamma_1]$
Pin Material	400	2000	7
Plate Material	364	1750	7

6.4.1 Device number 1

This device had the SOFMAN material (13PIN235) characterizing the constitutive relation of the Pin. From Figure 6.25, it is possible to see that there is some agreement with the curves, except on the last cycles and the unloading range. One of the reasons for this discrepancy might be related to the highly irregular behaviour and great lateral displacements in the experimental test. While in the numerical model it was designed to be symmetrical and without lateral displacement.

Figure 6.25 - Comparison of hysteretic curves between experimental test (blue) and numerical model version B (black) of specimen 1.

6.4.2 INERD device "c50_eccs"

Using the available information on this experimental test, model type B was implemented. In general, the results were satisfactory, the overall curves were quite similar, except for the maximum forces in the negative displacements (Figure 6.26). As identified in section 6.1.1, one of the causes for this difference is the gap, the experimented device probably had an asymmetric plate hole. As a result, the sudden gain of stiffness happens in very distinct displacement values. From Figure 6.28, it is possible to see that the numerical solution was capable of capturing the plastification of the lateral plates, hence the different ultimate forces achieve in each direction, visible on both the hysteretic curves.

When predicting failure, from the calibrated value of PEEQ=5.833, this simulation failed at 23.6 cycles. Since the experimental test failed at 24.5 cycles, this method had an error of less than one cycle, this is represented in Figure 6.27. Although no damage model is implemented, this simplification could be applied, with good accuracy, on a device with a different geometry.

Figure 6.26 - Comparison of hysteretic curves between experimental test (blue) and numerical model version B(black) of specimen "c50_eccs".

Figure 6.27 - "c50_eccs"- Accuracy of failure prediction with the evolution of maximum PEEQ value (blue), the limit of cycles of the experimental test (light blue), the calibrated value of PEEQ (Black) and correspondent number of cycle achieved by the solution (red).
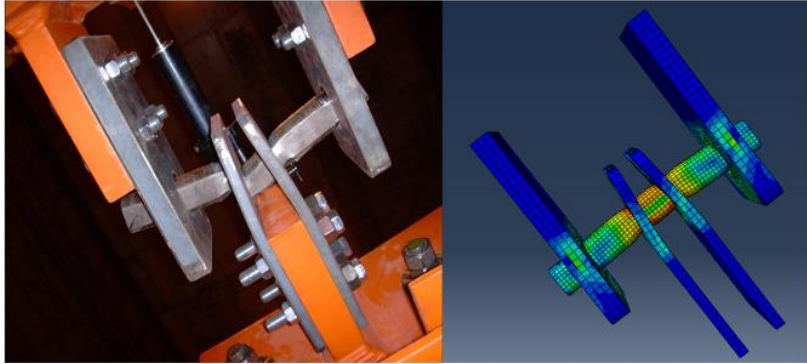
Figure 6.28 - "c50_eccs"- State of the box: at the end of the test(left) and the end of the simulation(right) with Von Mises stress.

6.4.3 INERD device "c70_eccs"

Even with a larger distance amongst internal plates, the comparison between curves is very identical to the one from device"c50_eccs", from the hysteretic curves (Figure 6.29) to the distribution of deformations (Figure 6.31). As shown in Figure 6.30, the failure analysis was successful, the experimental test failed at 25 cycles and, in the simulation, it failed at 24.4. This leads to an error of less than a cycle.

It can be concluded that the calibrated value of PEEQ achieves good predictions regardless of the type of material, the INERD and DISSIPABLE devices are constituted by materials with different constitutive relations. As this criterion is based on strain values, it is independent on the behaviour of each material. For example, a device that had a pin with lower yield stress would logically fail earlier than one with higher yield stress. In the simulation, it would be able to predict it because the first device would reach higher strains faster and consequentially break earlier.
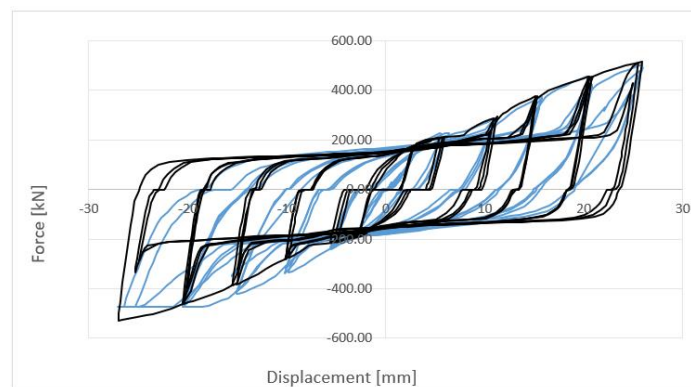

Figure 6.29 - Comparison of hysteretic curves between experimental test (blue) and numerical model version B(black) of specimen "c70_eccs".
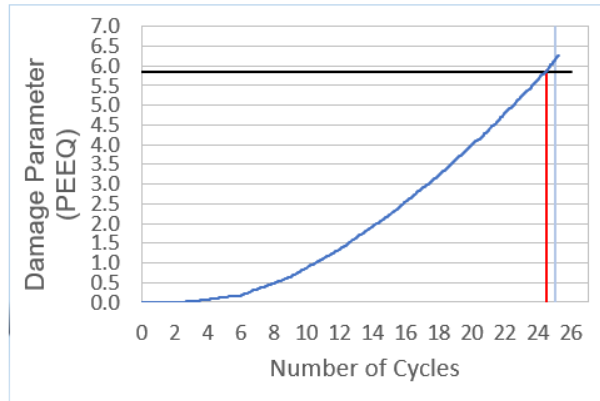
Figure 6.30 - "c70_eccs"- Accuracy of failure prediction with the evolution of maximum PEEQ value (blue), the limit of cycles of the experimental test(light blue), the calibrated value of PEEQ (Black) and correspondent number of cycle achieved by the solution (red).
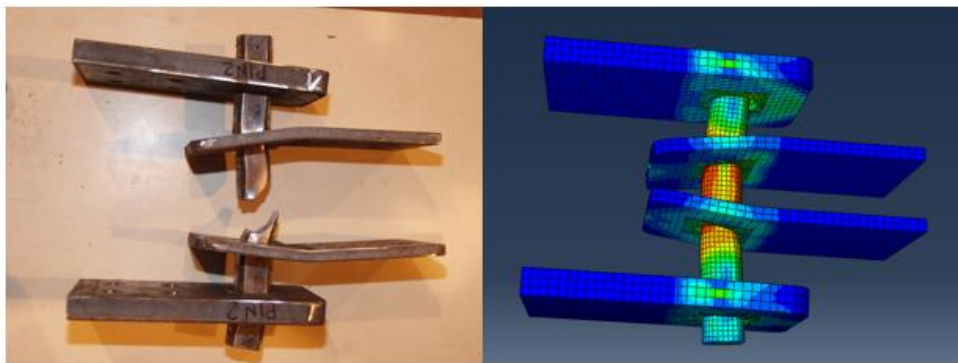
Figure 6.31 - "c70_eccs"- State of the box: at the end of the test(left) and the end of the simulation(right) with Von Mises stress.

6.4.4 INERD device "r70_eccs"

Lastly, a specimen with a rectangular pin was modelled in the software. Comparing the hysteretic curves (Figure 6.32) the accuracy of the model was surprisingly good, all major comparative parameters were very similar. Besides, as shown in Figure 6.34, the displacement of the plates was also captured. In this case, the external plates were also affected mainly due to the low yield stress of these and the higher rigidity from this rectangular pin.

When applying the simplified method to predict failure, it did not work. In the experimental test, the device broke at 20.5 cycles while in the numerical model, extrapolating from PEEQ evolution would fail at around 24 cycles (Figure 6.33). The reason might be from the different pin shape and the type of plate holes. This method relies on deformations so when these have a different mode a new PEEQ value needs to be calibrated. Furthermore, in this device, the rotation of the pin is locked by the internal plate holes that also have a rectangular shape. In the devices with a chamfered pin, these holes have a circular chape allowing rotation freely.
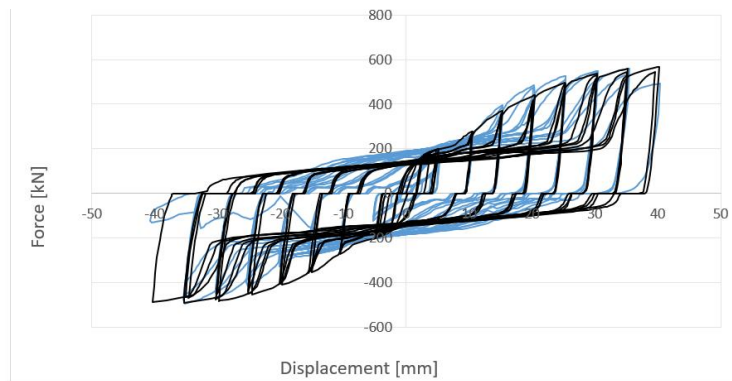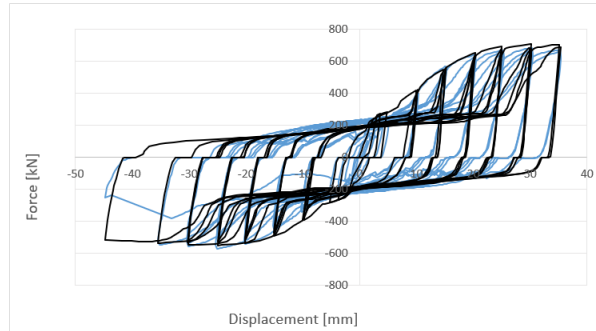
Figure 6.32 - Comparison of hysteretic curves between experimental test (blue) and numerical model version B (black) of specimen "r70_eccs".
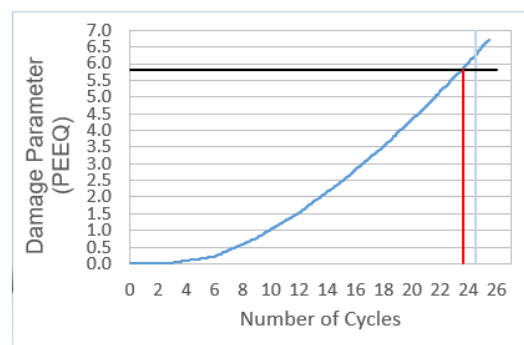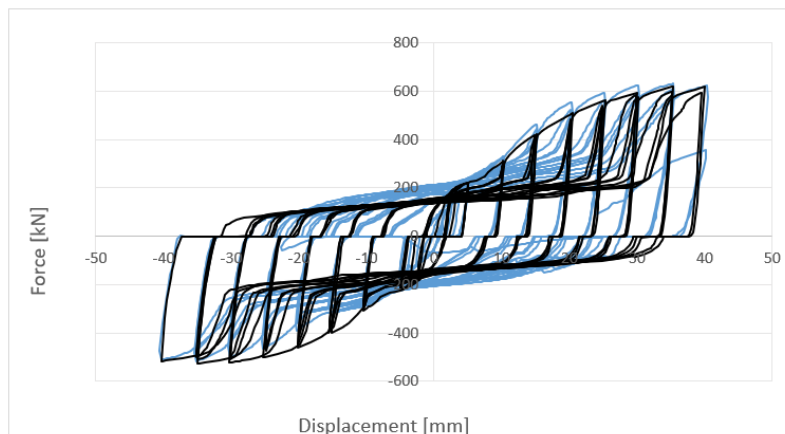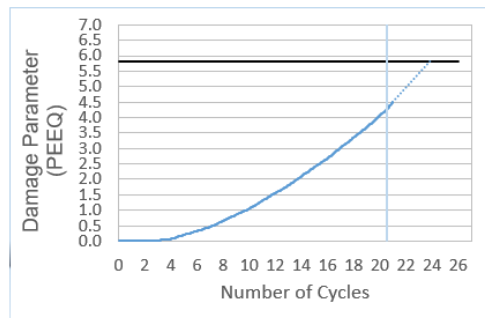

Figure 6.33 - "r70_eccs" Accuracy of failure prediction with the evolution of maximum PEEQ value (blue), the limit of cycles of the experimental test (light blue), the calibrated value of PEEQ (Black).
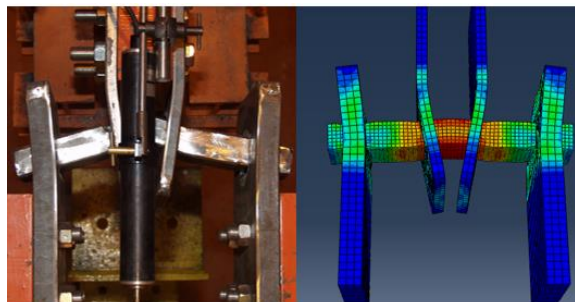
Figure 6.34 - "r70_eccs" - State of the box: at the end of the test (left) and the end of the simulation (right) with Von Mises stress.

6.5 Parametric study

A parametric study was realized within the scope of the experimental tests to be performed(Annex A – Figure A.1). For this matter, the tests chosen were: test 5 (code: 05-R_S235_HSS_D1_E) and test 19 (code: 19-R_S235_HSS_D2_E), where the difference between them are the internal plate spacing (test 5=70mm and test 19=90mm). The only geometric difference of these tests remains on a smaller section size of the pin, from a diameter of 50mm to 45mm. These tests were performed using the same load history as test number 2. Test 5 and 19 were modelled with that same definition as the IST material for

the Pin and as for the High Strength Steel(HSS), the S690 was used [50], calibrated to the following values: f_y=690 MPa, $C_1 = 3130$, $\gamma_1 = 17$. These simulations were solved with the simplified method to predict failure, to compare the dissipated energy up until failure, of three different scenarios.

1. The first comparison aims to understand the consequences of changing the Pin's section and length, so the test number 2 was compared with test 5, using the same plate material as test 2 (Figure 6.35)
2. The second scenario assesses the influence of using HSS in the Lateral Lates. In Figure 6.36, the curves from test 5 are compared, using as the material of the Lateral Plates: HSS and the 1EP355 material~
3. The third scenario studies the influence of the internal plate spacing. Figure 6.37 compares test 5 with test 19, both using HSS for the lateral plates.

Table 6.11 summarizes the number of cycles and the energy dissipated until fracture, of the four simulations.
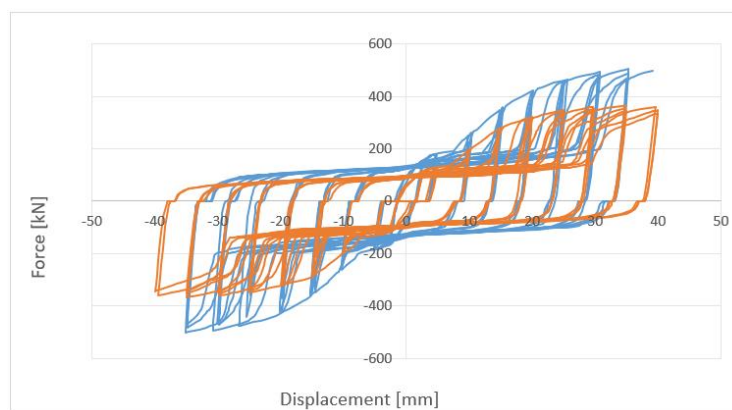
Figure 6.35 - Hysteretic curves of the first scenario, Test number 2(blue) and test number 5 with the plate material 1EP355 (orange).
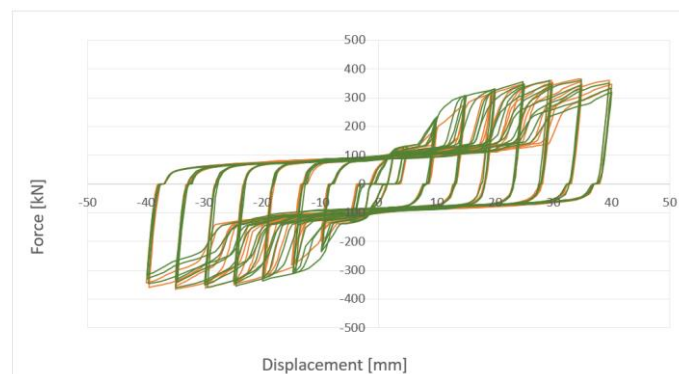
Figure 6.36 - Hysteretic curves of the second scenario, Test number 5 with plate material: 1EP355 (orange) and HSS (Green).
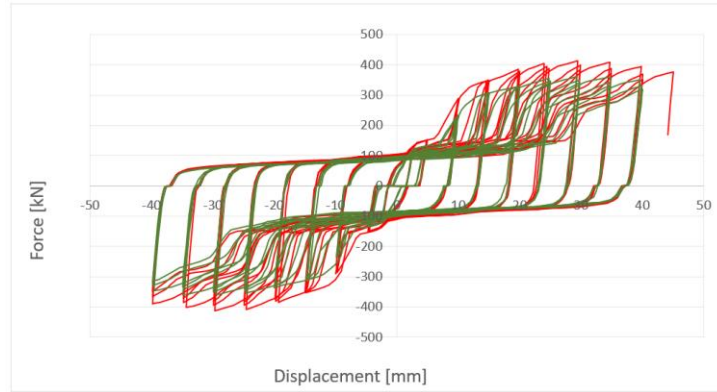
Figure 6.37 - Hysteretic curves of the third scenario, Test number 5 (green) and test number 19 (orange), both with HSS.

Table 6.11 - Number of cycles achieved and total energy dissipation of each simulation.

Devices	Test 2	Test 5 (using 1EP355 as plate material)	Test 5 (using HSS as plate material)	Test 19
Number of cycles achieved until failure	25.43	27.69	27.79	28.29
Total energy dissipated (kNm)	241	219	231	264

The first scenario shows that the reduction of the section of the pin lowers the forces achieved in each cycle. Although test 5 runs more cycles until failure than test 2, the second can dissipate more energy.

The second scenario shows that using HSS as the plate material does improve its behaviour. Both run a similar number of cycles but the device using HSS can dissipate more energy.

The third scenario shows that having a higher distance between plates might be beneficial. Test 19 can withstand more cycles and dissipate more energy.

In the end, assuming that the error of predicting failure maintains low, using HSS on the plates and increasing the distance between them is beneficial. These changes help to dissipated energy without increasing much the maximum forces, which happens with the device with a larger Pin section. Maintaining a lower maximum force is important to decrease the probability of damage in the rest of the structure.

7 Final Conclusions and Suggestions for Future Work

7.1 Conclusions

The objective of this work was to create a numerical model able to capture the behaviour of the devices tested within the scope of the DISSIPABLE project. For this dissertation, a methodology was developed, which assisted in choosing the solver type, the implementation of the geometry and respective mesh sizes, the creation of a logical method to assess the true parameters from a generic experimental tensile test, the contact parameters and the definition of a damage criterion. In this task, the experimental data available was used to calibrate the numerical model.

The used of a finite element method with an implicit solver proved to be able of handling such a complex problem. Although it was difficult to converge these simulations at the beginning, when achieved, we could be confident in the results because we knew the equilibrium was always respected throughout every numerical solution, which also made it possible to perform a parametric study on several parameters. In the end, this affected the variety of damage criteria that could be applied but accuracy should come first, especially in such long tests, that have a big overlay of effects.

The material calibration methodology proved to be quite efficient to define the true variables required on a *combined hardening* formulation when only the engineering curve is available. With the first step of numerically simulating the experimental tensile tests, the parameters calculated could be directly implemented in other simulations such as the DRD1 and the INERD.

Using experimental tests in the calibration of the model with a wide variety of load cases, different boundary conditions and internal plate distances, it was concluded that the model could obtain accurate hysteretic curves regardless of those conditions. Two variants of the model were created, and both had similar results, but one was preferred due to its lower time to solve, from around 34 hours to 6.5 hours.

In the DRD1, the accumulation of strains happened in the middle, leading to damage. However, the model spread it between two localized zones, where the pin comes to contact with the internal plates. Consequently, it worked well with INERD devices, in the validation tests, since their deformation mode was also primarily in those two zones.

For the implementation of a damage criterion, it was identified a possible way to implement such behaviour. The *Maxpe* formulation proved to be capable of achieving such a task but, unfortunately, this method was difficult to calibrate. Not being able to reach a unique set of values that could attain satisfactory results for different devices with different conditions, another method was developed. This method, that relies on the concentration of plastic strains could achieve an acceptable prediction on the number of cycles that each device could withstand, even though it does not implement degradation on the material. This technique was successful for every device with a chamfered pin but when tested on

a specimen with a rectangular pin it failed, this method is therefore probably dependent on the geometry of pin tested.

From the brief parametric study performed, it can be concluded that the usage of HSS will be beneficial for these devices as it increases the dissipated energy, without increasing the maximum forces withstood by the DRD1. In addition, increasing the distance between internal plates improved its behaviour with a slight increase of the maximum force value.

7.2 Future Work

To understand the robustness and the limitation of this model, this should be compared with different experiment tests, such as, the ones that will be performed in January 2020, LERM.

Considering the new set of spacers added to the DRD1 upon the first experimental campaign, it would be beneficial to study a model that would use them. For this, an eccentricity on the application of the load case should be studied and implemented, otherwise, those spacers would have no effect.

The type of solver used, proved to be successful but it would be interesting to explore the explicit solver further. That solver would be able to calculate solutions using *ductile damage* (including degradation) in the material formulation and, therefore, possible to calibrate this type of damage criterion into the DRD1.

Upon understanding that the damage criteria, *Maxpe*, can obtain good results (implementing damage degradation), a study could be conducted. The calibration of this method should be performed using the tensile tests, to achieve good results on the DRD1. If successful, through any tensile test it would be possible to predict the damage response on any type of DRD1.

To understand the device behaviour in real conditions, it would be interesting to subject it to real seismic spectrums. So that in the end, the behaviour of this device could be simplified to a spring type curve. With this simplification of the device behaviour, it could be easily used and calculated during the conception of the building. Otherwise, it would be a much heavier calculation to take into account the hysteretic properties of these.

References

[1]   Cambridge international dictionary of English. 1995. Cambridge: Cambridge University Press.

[2]   EN1998-1: 2004. Eurocode 8: Design of structures for earthquake resistance. -Part 1: General rules, seismic actions and rules for buildings, CEN, Bruxelles, Belgium.

[3]   FEMA 273: NEHRP, 1997.guidelines for the seismic rehabilitation of buildings, Federal Emergency Management Agency.

[4]   Bento, R. e Lopes, M. 1990. Modelação Fisicamente Não Linear de Estruturas de Betão Armado. Disciplina de Modelaçãoo e Análise Estrutural, Instituto Superior Técnico.

[5]   Calado, L., Proença, J. M., Cabrita, D., Nascimento, S. 2020. The DISSIPABLE project, Work Package 4 – Deliverable 4.1 Report on experimental tests on DRD systems. Research Programme of the Research Fund for Coal and Steel.

[6]   Nascimento, S. M. D. 2020. Detailed Experimental Programme Fully Dissipative and Easily Repairable devices for resilient buildings with composite steel-concrete structures – Pin device. Advanced Studies Diploma in Civil Engineering, Instituto Superior Técnico.

[7]   Chen, Z., Zhu, E., Lam, F., Pan, J. 2014. Structural performance of Dou-Gong brackets of Yingxian Wood Pagoda under vertical load – An experimental study. *Engineering Structures*, Vol.80, pp 274-288.

[8]   Pelke, E., Kurrer, K. E. 2015. On The Evolution Of Steel-Concrete Composite Construction. 5th International Congress on Construction History, Chicago. *5ICCH Proceedings*, Vol. 3, pp 107-116.

[9]   Calado, L., Santos, J. 2013. Estruturas Mistas de Betão e Aço. *IST press*, 2ªedition.

[10]   Tsavdaridis, K. D. 2015. Seismic Analysis of Steel-Concrete Composite Buildings: Numerical Modeling. *Encyclopedia of Earthquake Engineering*, pp 1-36.

[11]   Dinu, F., Dubina, D., Marginean, I. 2014. Improving the structural robustness of multi-story steel-frame buildings. *Structure and Infrastructure Engineering,* Vol 8, pp 1028-1041.

[12]   Plumier, A., Doneux, C., L. Sanchez, R. Agatino, C. Plumier, A. Elnashai, M. Tsujii, R. Pinho, J. Bouwkamp, H. Parung, B. Broderick, A. Elghazouli, E. Cosenza, & G. Manfredi. 2001. Siesmic behaviour and design of composite steel concrete structures. ICONS Report 4. *LNEC Edition*. Lisbon.

[13]   Buckle, I. G. 2000. Passive control of structures for seismic loads. *Bulletin of the New Zealand Society for Earthquake Engineering*. Vol 33, pp 209-221.

[14]   Soong, T. T.,1990. Active Structural Control: Theory and Practice, Longman, London, and Wiley, New York.

[15]   Skinner, R. I., Robinson, W. H., McVerry, G.H. 1993. An Introduction to Seismic Isolation, John Wiley & Sons Ltd, West Sussex, England.

[16]   Septimiu, L., Chira, F., Victor, O. R. 2005 Passive, Active and Semi-Active Control Systems in Civil Engineering. Bulletin of the Polytechnic Institute of Jassy, Vol 2, pp 23-31.

[17]   Hill, K.E., 1995. The Utility of Ring Springs in Seismic Isolation Systems. Ph.D Thesis, Department of Mechanical Engineering, University of Canterbury

[18]   Okada, K., Nakamura, Y. 2019. Review on seismic isolation and response control methods of buildings in Japan. *Geoenviron Disasters 6*, Article number 7.

[19]   Warn, G. P., Ryan, K. L. 2012. A Review of Seismic Isolation for Buildings: Historical Development and Research Needs. *Mdpi Buildings*, Vol 2, pp 300-325.

[20]   Aghlara, R., Tahir, M. M., Adnan, A. 2015. Comparative study of eight metallic yielding dampers. *Jurnal Teknologi,* Vol 77, pp 119–125

[21]   Vayas, I., Thanopulos, P., Tsarpalis, P., Dimakogianni, D., Henriques, J., Degee, H., Hoffmeister, B., Pinkawa, M., Castiglioni, C. A., Alavi, A., Brambilla, G., Calado, L., Proença, J. M., Sio, J., Chesoan, A., Stratan, A., Dubina, D., Neagu, C., Dinu, F., dubina, D., Georgiev, T., Raycheva, L., Zhelev, D., Rangelov, N., Morelli, F., Natali, A., Salvatore, W., Butz, C., Renzi, V., Butz, C., Medeot, R. 2017. The INNOSEIS Project, Innovative Anti-Seismic Devices and Systems, Research Programme of the Research Fund for Coal and Steel, Grant agreement RFSR-CT-2008-709434, ECCS – European Convention for Constructional Steelwork.

[22]   Namora, B. C. P. C. 2019. Pórticos planos sujeitos a sismos: dissipação de energia por atrito. Master Thesis, Departement of Civil Engineering, Lisbon university, IST.

[23]   Soong, T. T., Spenser, B. F., 2002. Supplemental Energy Dissipation: state-of-the-art and state-of-the-practice, Engineering Structures, Vol. 24, pp 243-259.

[24]   Connor, J. J. 2002. Introduction to Structural Motion Control. Prentice Hall; 1st edition, chapter 4.

[25]   Bishay, G. N. W., Carr, A. J. 2014. Ring spring dampers: Passive control system for seismic protection of structures. *Bulletin of the New Zealand Society for Earthquake Engineering*, Vol 47, pp 173-180.

[26]   Plumier, A., Doneux, C., Castiglioni, C., Brescianini, J., Crespi, A., Dell'anna, S., Lazzarotto, L., Calado, L., Ferreira, J., Feligioni, S., Bursi, O., Ferrario, F., Sommavilla, M., Vayas, I., Thanopulos, P., Demarco, T. 2004. Two innovations for earthquake resistant design: The INERD Project, Final Report. Research Programme of the Research Fund for Coal and Steel, Grant Agreement No7210-PR-316.

[27]   Thanopoulos, P. 2006. Earthquake behavior of metal carriers with energy absorption systems. Ph.D Thesis, Department of structures. National Technical University of Athens

[28]   DASSAULT 2014. Abaqus Analysis User's Guide. *Version 6.14*. France: Dassault Systèmes Simulia Corporation.

[29]   Chaboche, J. L., Rousselier, G. 1983. On the Plastic and Viscoplastic Constitutive Equations—Part I: Rules Developed With Internal Variable Concept, *Journal of Pressure Vessel Technology*, Vol. 105(2), pp 153-158.

[30]   Chaboche, J. L. 2008. A review of some plasticity and viscoplasticity constitutive theories. *International Journal of Plasticity*, Vol. 24, pp 1642-1693.

[31]   Li, K. P., Carden, W. P., Wagoner, R. H. 2002. Simulation of springback, *International Journal of Mechanical Sciences,* Vol. 44, pp 103-122.

[32]   Zhuang, X., Ma, Y., Zhao, Z. "Fracture prediction under nonproportional loadings by considering combined hardening and fatigue-rule-based damage accumulation," *International Journal of Mechanical Sciences,* Vol. 150, pp 51-65.

[33]   Lemaitre, J., Chaboche, J. L. 1990. Mechanics of Solid Materials, Cambridge University Press.

[34]   Faridmehr, I., Osman, M. H., Adnan, A. B., Najed, A. F., Hodjati, R., Azimi, M. A. 2014. Correlation between Engineering Stress-Strain and True Stress-Strain Curve. *American Journal of Civil Engineering and Architecture,* Vol. 2, pp 53-59.

[35]   Tu, S., Ren, X., He, J., Zhang, Z. 2019. Stress-strain curves of metallic materials and post-necking strain hardening characterization: A review. *Fatigue and Fracture of Engineering Materials and Structures(FFEMS),* Vol. 43, pp 3-19.

[36]   Bridgman, P. W. 1952. Studies in Large Plastic Flow and Fracture, McGraw-Hill, New York

[37]   Wang, Y. D., Xu, S. H., Ren, S. B., Wang, H. 2016. An Experimental-Numerical Combined Method to Determine the True Constitutive Relation of Tensile Specimens after Necking. *Advances in Materials Science and Engineering,* Vol. 2016, pp 1-12.

[38]   Barsoum, I., Ali, K. F. 2015. A procedure to determine the tangential true stress-strain behaviour of pipes. *International Journal of Pressure Vessels and Piping,* Vol. 128, pp 59-68

[39]   Paul, S. K., Roy, S., Sivaprasad, S., Tarafder, S. 2018. A Simplified Procedure to Determine Post-necking True Stress–Strain Curve from Uniaxial Tensile Test of Round Metallic Specimen Using DIC. *Journal of Materials Engineering and Performance,* Vol. 27, pp 4893-4899.

[40]   Bandstra, J. P., Koss, D. A., Geltmacher, A., Matic, P. & Everett, R. K. 2004. Modeling void coalescence during ductile fracture of a steel. *Materials Science and Engineering*, Vol. 366, pp 269-281.

[41]   Børvik, T., Hopperstad, O. S. & Berstad, T. 2003. On the influence of stress triaxiality and strain rate on the behaviour of a structural steel. Part II. Numerical study. *European Journal of Mechanics - A/Solids,* Vol. 22, pp 15-32.

[42]   Ying, Y., Liu, X., Han, Q. Liu, Z. 2018. Simulation of ductile fracture of structural steels with void growth model and a continuum damage criterion based on it. *Theoretical and Applied Fracture Mechanics*, Vol. 98, pp 134-148.

[43]   Anderson, T. L. 2005. Fracture Mechanics: Fundamentals and Applications, 3a . CRC Press

[44]   Belytschko, T., Black, T. 1999. Elastic crack growth in finite elements with minimal remeshing. *International Journal for Numerical Methods in Engineering*, Vol. 45, pp 601- 620.

[45]   Santos, T. G., 2017 Estudo numérico da propagação de fendas de fadiga num aço de alta resistência. Master Thesis, Mechanical Engineering Department, Lisbon university, IST.

[46]   Ahmad, M., Sosa, J. L. C., Arun, S., Rongong, J. 2018. An enhanced void-crack-based Rousselier damage model for ductile fracture with the XFEM. *International Journal of Damage Mechanics,* Vol. 28, pp 943-969.

[47]   Barber, J. R. & Ciavarella, M. 2000. Contact mechanics. *International Journal of Solids and Structures,* Vol. 37, pp 29-43.

[48]   Adams, G. G. & Nosonovsky, M. 2000. Contact modeling - forces. *Tribology International*, Vol. 33, pp 431- 442.

[49]   ECCS.1986. Recommended testing procedures for assessing the behaviour of structural steel elements under cyclic loads, ECCS Publication nº45.

[50]   Calado, L., Proença, J. M., Cabrita, D., Nascimento, S. 2020. The DISSIPABLE project, Work Package 2 – Deliverable 2.2 Report on parametric studies of DRD systems. Research Programme of the Research Fund for Coal and Steel

Annex A

Full list of experiemental test specimens

No of test configuration	Configuration code (*)	Pin shape	Pin Φ	Pin steel	External plate thickness	External plate dimensions	Internal Plate spacing	Internal plate thickness	External plate dimensions	Plates steel	Load protocol
1	R_S235_S355_D1_E	R	50	S235	30	220x300	D1	20	140x300	S355	E
2	R_S235_S355_D1_C1	R	50	S235	30	220x300	D1	20	140x300	S355	C1
3	R_S235_S355_D1_C2	R	50	S235	30	220x300	D1	20	140x300	S355	C2
4	R_S235_S355_D1_C3	R	50	S235	30	220x300	D1	20	140x300	S355	C3
5	R_S235_HSS_D1_E	R	45	S235	30	220x300	D1	20	140x300	HSS	E
6	R_S235_HSS_D1_C1	R	45	S235	30	220x300	D1	20	140x300	HSS	C1
7	R_S235_HSS_D1_C2	R	45	S235	30	220x300	D1	20	140x300	HSS	C2
8	R_S235_HSS_D1_C3	R	45	S235	30	220x300	D1	20	140x300	HSS	C3
9	R_StS_S355_D1_E	R	45	StS	30	220x300	D1	20	140x300	S355	E
10	R_StS_S355_D1_C1	R	45	StS	30	220x300	D1	20	140x300	S355	C1
11	R_StS_S355_D1_C2	R	45	StS	30	220x300	D1	20	140x300	S355	C2
12	R_StS_HSS_D1_E	R	45	StS	30	220x300	D1	20	140x300	HSS	E
13	R_StS_HSS_D1_C1	R	45	StS	30	220x300	D1	20	140x300	HSS	C1
14	R_StS_HSS_D1_C2	R	45	StS	30	220x300	D1	20	140x300	HSS	C2
15	C_S235_S355_D1_E		50	S235	30	220x300	D1	20	140x300	S355	E
16	C_S235_S355_D1_C1		50	S235	30	220x300	D1	20	140x300	S355	C1
17	C_S235_S355_D1_C2		50	S235	30	220x300	D1	20	140x300	S355	C2
18	C_S235_S355_D1_C3		50	S235	30	220x300	D1	20	140x300	S355	C3
19	R_S235_HSS_D2_E	R	45	S235	30	220x300	D2	20	140x300	HSS	E
20	R_S235_HSS_D2_C1	R	45	S235	30	220x300	D2	20	140x300	HSS	C1
21	R_S235_HSS_D2_C2	R	45	S235	30	220x300	D2	20	140x300	HSS	C2
22	R_S235_HSS_D2_C3	R	45	S235	30	220x300	D2	20	140x300	HSS	C3
23	R_StS_S355_D2_E	R	45	StS	30	220x300	D2	20	140x300	S355	E
24	R_StS_S355_D2_C1	R	45	StS	30	220x300	D2	20	140x300	S355	C1
25	R_StS_S355_D2_C2	R	45	StS	30	220x300	D2	20	140x300	S355	C2
26	R_StS_HSS_D2_E	R	45	StS	30	220x300	D2	20	140x300	HSS	E
27	R_StS_HSS_D2_C1	R	45	StS	30	220x300	D2	20	140x300	HSS	C1
28	R_StS_HSS_D2_C2	R	45	StS	30	220x300	D2	20	140x300	HSS	C2
		R									

Dimensions in mm and steel grades in MPa
(*) Configuration code according to: #PinShape_#PinSteelGrade_#PlatesSteelGrade_#InternalPlateSpacing_#LoadProcotol

Color codes			
Protocol	Pin section	Steel grade	Internal plate spacing
E = ECCS	R = ⬭ Chamfered	S235	D1 = 80/70/80
C1 = Constant 1	C = ◯ Circular	StS	D2 = 70/90/70
C2 = Constant 2		S355	
C3 = Constant 3		HSS	

Figure A.1 - Specifications of each specimen to be tested in the laboratory upon conclusion of the first campaign

Test Configurations		Pin			Spacers		Plates		
No	Code	Section	Φ (mm)	Material	GP1	GP2	Ext. (mm)	Int. (mm)	Mat.
1	R_S235_S355_E	R	50	SOFMAN			30x 220x 300	20x 140x 300	S355
2	R_S235_S355_E	R	50	IST	X				S355
3	R_S235_S355_C1	R	50	IST	X				S355
4	R_S235_S355_C2	R	50	IST	X	X			S355
15	C_S235_S355_E	C	50 W1	SOFMAN	X				S355
16	C_S235_S355_E	C	50 W2	IST	X	X			S355
17	C_S235_S355_E	C	50 W1	IST	X	X			S355
18	C_S235_S355_E	C	50 W3	IST	X	X			S355

Figure A.21 - Specifications of the tests performed in the first campaign at the end of 2019
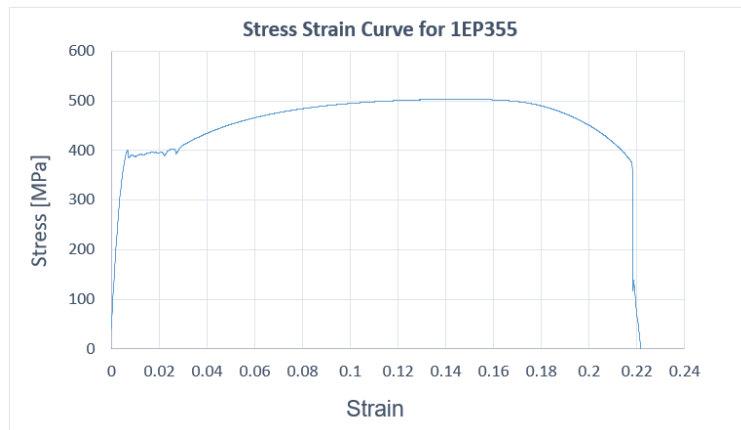
Annex B

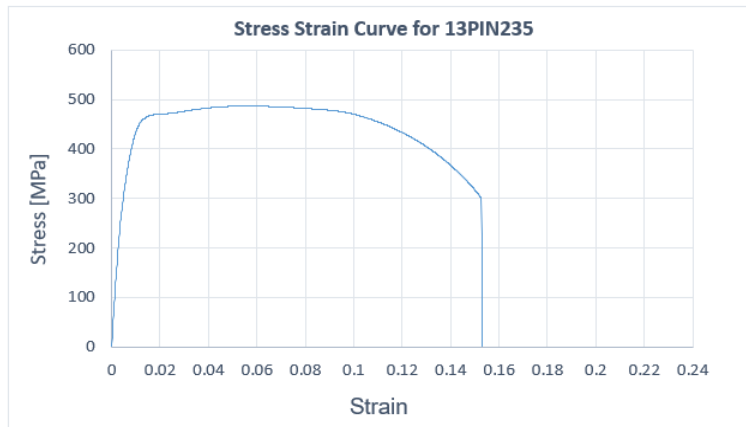Figure B.1 - Engineering Stress-Strain Curve for test 1EP355

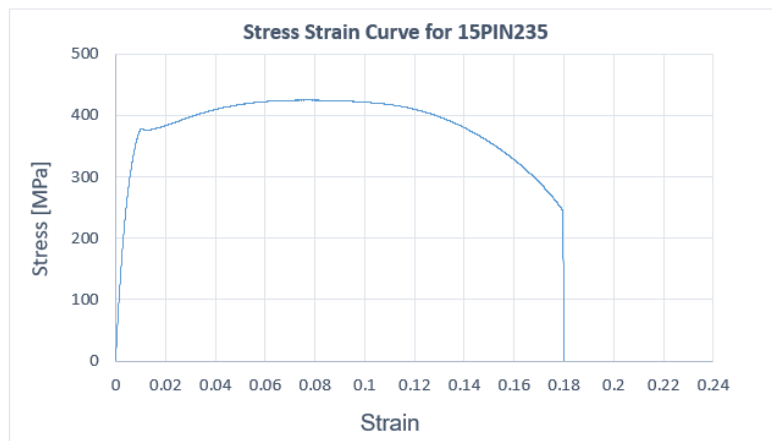Figure B.2 - Engineering Stress-Strain Curve for test 13PIN235

Figure B.3 - Engineering Stress-Strain Curve for test 15PIN235
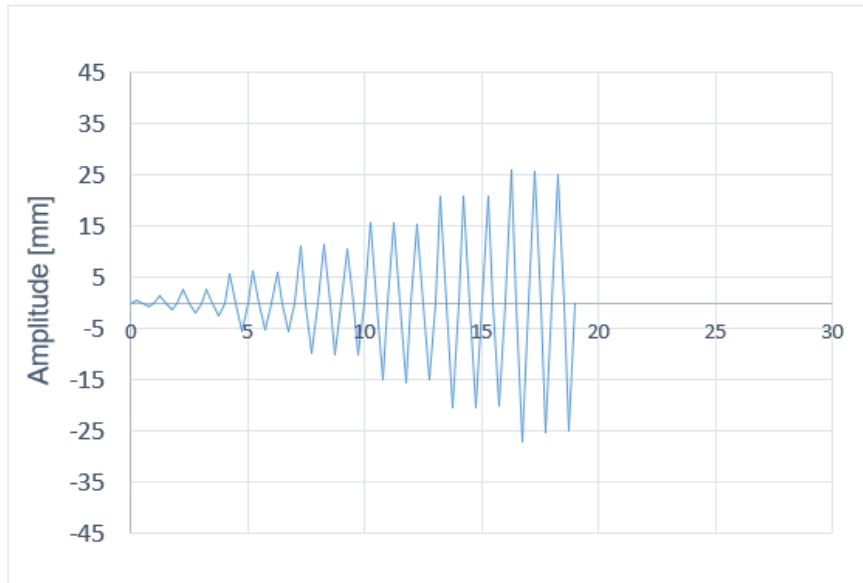
Annex C

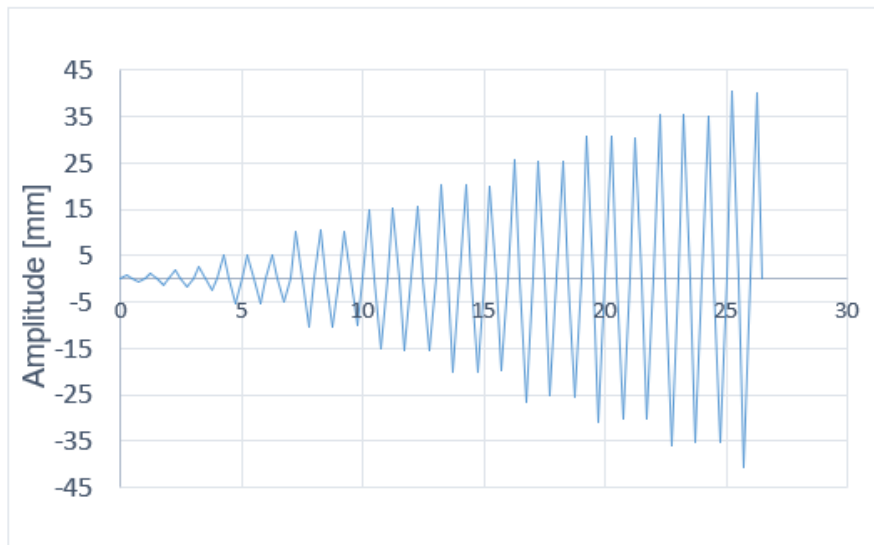Figure C.1 - Load case used on device number 1 numerical simulation

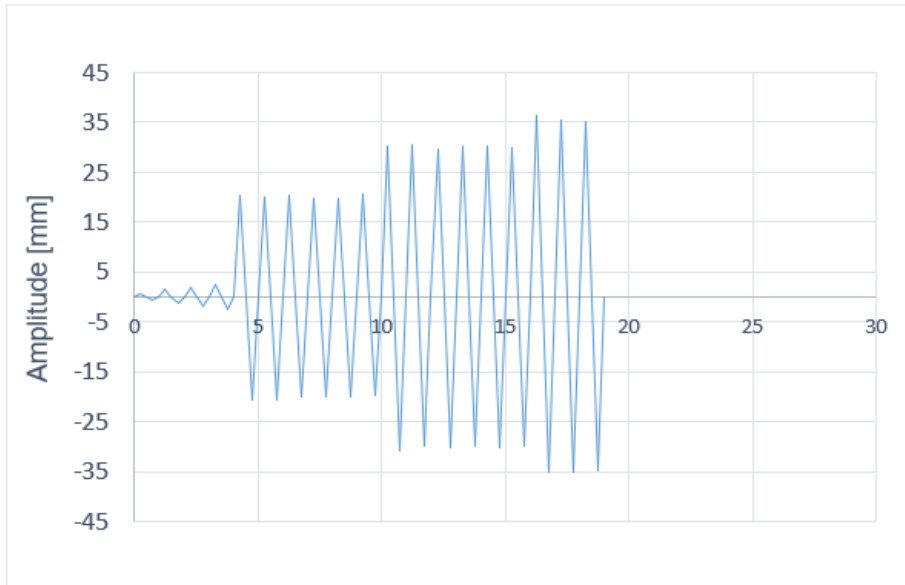Figure C.2 - Load case used on device number 2 numerical simulation

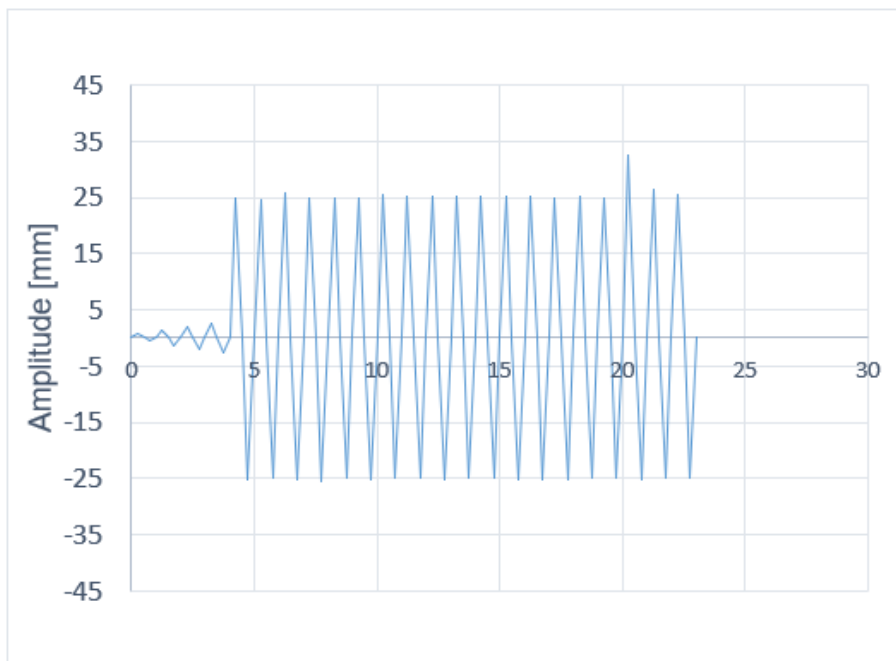Figure C.3 - Load case used on device number 3 numerical simulation

Figure C.4 - Load case used on device number 4 numerical simulation